UTS UNIVERSITY OF TECHNOLOGY SYDNEY

Engineering Polymeric Hydrogels for Solar Water Purification

by Shudi Mao

Thesis submitted in fulfilment of the requirements for the degree of

Doctor of Philosophy

under the supervision of Associate Professor Qiang Fu and Professor Long D. Nghiem

University of Technology Sydney
Faculty of Engineering and Information Technology

June 2025

Certificate of Original Authorship

I, Shudi Mao declare that this thesis, is submitted in fulfilment of the requirements for the award of Doctor of Philosophy, in the School of Civil and Environmental Engineering/Faculty of Engineering and Information Technology at the University of Technology Sydney.

This thesis is wholly my own research work unless otherwise referenced or acknowledged. In addition, I certify that all information sources and literature used are indicated in the thesis.

This document has not been submitted for qualifications at any other academic institution.

This research is supported by the Australian Government Research Training Program.

Signature: Production Note: Signature removed prior to publication.

Date: 26/06/2025

Acknowledgements

At the outset, my deepest gratitude goes to my principal supervisor, Associate Professor Qiang Fu, for his unwavering guidance, encouragement, and mentorship throughout my PhD journey. Starting my PhD during the challenging COVID-19 pandemic, Qiang provided invaluable support, including assistance with my Australian border exemption application and adjustments to my research plan during off-shore study. His dedication ensured a smooth start to my PhD. His passion for academia has been a tremendous source of encouragement for me, especially during times when I encountered challenges in my research. He always provided innovative and practical ideas, which greatly alleviated my anxiety and helped me move forward. Additionally, I am also deeply grateful to my co-supervisor, Professor Long D. Nghiem, for his academic insights and steadfast support. It has been a true privilege to complete my PhD under their supervision.

I would also like to express my heartfelt thanks to Prof. Dawei Su and Dr. Xiaoxue Helen Xu for their valuable collaboration and support. My gratitude also goes to the UTS laboratory technical support officers, including Dr. Mohammed AH. Johir and Dr. Zhimei Xu, for their comprehensive training in laboratory safety and the characterization techniques essential for my experiments.

I am profoundly grateful to my colleagues and friends in University of Technology Sydney (UTS) who have supported me during this incredible journey. To Ms. Xin Stella Zhang, Mr. An Feng, Mr. Casey Onggowarsito, and Ms. Yihan Shi, thank you for being

my pillars of support, for the countless discussions that sparked new ideas, and for the moments of laughter that kept me grounded. To Mr. Ming Zhou, Mr. Qian Chen, Mr. Jiaqi Zhang, Dr. Huan Liu, Dr. Chen Wang, Dr. Haoding Xu, Dr. Feng Shan, Dr. Derek (Qiang) Hao, Dr. Fulin Qu, Mr. Yang Jiang, Mr. Jibin Li, Ms. Gaihong Wang, Dr. Lan Wu, Dr. Xuan Zhang, Dr. Bing Zhang, Dr. Wei Huang, Dr. Zehao Zhang, Dr. Zhengheng Xu, Mr. Xingdong Shi, Dr. Jianyuan Zhen, Ms. Huishan Meng, Mr. Siran Feng, Ms. Ting Zhou, Mr. Zhenyao Wang, Ms. Hanwei Yu, Ms. Ying Long, Ms. Yuanying Yang, Mr. Shida Zhao, Mr. Haibin Xiong, and Ms. Jiashu Wang, your encouragement and friendship have been a source of great comfort and motivation. In addition, I would like to thank Ms. Oliwia Degórska, Ms. Aleksandra Makiej, and Ms. Weronika Badzińska, my lovely friends from Poland, for the wonderful days of working and having fun together. I am immensely lucky to have shared this chapter of life with you all.

To my parents, Mr. Jianguo Mao and Ms. Qing Wang, words cannot express the depth of my appreciation for your unconditional love and unwavering belief in me. You have been my greatest source of strength and the foundation upon which I have built this journey.

Lastly, I want to thank myself for persevering through the challenges, embracing the setbacks, and celebrating the successes. This journey has not been easy, but I am proud of the growth, resilience, and determination that have brought me to this milestone.

List of Publications

1. **Mao, S.**, Johir, M., Onggowarsito, C., Feng, A., Nghiem, L., & Fu, Q. (2022). Recent Developments of Hydrogel Based Solar Water Purification Technology. *Materials Advances*, 3(3), 1322-1340.
2. **Mao, S.**, Onggowarsito, C., Feng, A., Zhang, S., Fu, Q., & Nghiem, L. D. (2023). A cryogel solar vapor generator with rapid water replenishment and high intermediate water content for seawater desalination. *Journal of Materials Chemistry A*, 11(2), 858-867.
3. **Mao, S.**, Feng, A., Zhang, S., Onggowarsito, C., Chen, Q., Su, D., & Fu, Q. (2023). Investigation of structure-property-application relationships of the hydrogel-based solar vapor generator. *Journal of Materials Chemistry A*, 11(42), 23062-23070.
4. **Mao, S.**, Zhang, S., Shi, Y., Feng, A., Onggowarsito, C., Xu, X., Aditya, L., Sun, Y., Nghiem, L. D., & Fu, Q. (2025). Precision-Engineered, Polymer-Lean, Digital Light Processing 3D-printed Hydrogels for Enhancing Solar Steam Generation and Sustainable Water Treatment [10.1039/D5MH00018A]. *Materials Horizons*.
5. Onggowarsito, C., **Mao, S.**, Zhang, X. S., Feng, A., Xu, H., Fu, Q. J. E., & Science, E. (2024). Updated perspective on solar steam generation application. *Energy & Environmental Science*, 17(6), 2088-2099.
6. Feng, A., **Mao, S.**, Onggowarsito, C., Naidu, G., Li, W., & Fu, Q. (2023). Tillandsia-Inspired Composite Materials for Atmospheric Water Harvesting. *ACS Sustainable Chemistry & Engineering*, 11(15), 5819-5825.

7. Zhang, X. S., **Mao, S.**, Wang, J., Onggowarsito, C., Feng, A., Han, R., Liu, H., Zhang, G., Xu, Z., Yang, L., Fu, Q., & Huang, Z. (2024). Boron nanosheets boosting solar thermal water evaporation. *Nanoscale*, 16(9), 4628-4636.
8. Shi, Y., Feng, A., **Mao, S.**, Onggowarsito, C., Zhang, X. S., Guo, W., & Fu, Q. (2024). Hydrogels in solar-driven water and energy production: Recent advances and future perspectives. *Chemical Engineering Journal*, 492, 152303.
9. Onggowarsito, C., Feng, A., **Mao, S.**, Nguyen, L. N., Xu, J., & Fu, Q. (2022). Water Harvesting Strategies through Solar Steam Generator Systems. *ChemSusChem*, 15(23), e202201543.
10. Onggowarsito, C., Feng, A., **Mao, S.**, Zhang, S., Ibrahim, I., Tijing, L., Fu, Q., & Ngo, H. H. (2022). Development of an innovative MnO2 nanorod for efficient solar vapor generator. *Environmental Functional Materials*, 1(2), 196-203.
11. Feng, A., Onggowarsito, C., **Mao, S.**, Qiao, G. G., & Fu, Q. (2023). Divide and Conquer: A Novel Dual-Layered Hydrogel for Atmospheric Moisture Harvesting. *ChemSusChem*, 16(14), e202300137.
12. Onggowarsito, C., Shao, Z., **Mao, S.**, Zhang, S., Feng, A., Li, X., Wong, E. H., & Fu, Q. (2024). Versatile cationic dual-layer hydrogel filtration system for sustainable solar steam generator. *Materials Today Sustainability, 26*, 100753.
13. Aditya, L., Vu, H. P., Johir, M. A. H., **Mao, S.**, Ansari, A., Fu, Q., & Nghiem, L. D. (2024). Synthesizing cationic polymers and tuning their properties for microalgae harvesting. *Science of the Total Environment*, 917, 170423.

14. Feng, A., Shi, Y., Onggowarsito, C., Zhang, X. S., **Mao, S.**, Johir, M. A., Fu, Q., & Nghiem, L. D. (2024). Structure-Property Relationships of Hydrogel-based Atmospheric Water Harvesting Systems. *ChemSusChem*, 17(11), e202301905.

15. Feng, A., Akther, N., Duan, X., Peng, S., Onggowarsito, C., **Mao, S.**, Fu, Q., & Kolev, S. D. (2022). Recent Development of Atmospheric Water Harvesting Materials: A Review. *ACS Materials Au*, 2(5), 576-595.

Conference Presentations

Oral presentations:

1. **Mao, S.**, Feng, A., Zhang, S., Onggowarsito, C, Su, D., Nghiem, L. D. & Fu, Q. Nano and micro structure design of polymeric hydrogels for solar vapor generator-based seawater desalination, *International Conference on Advanced Materials for Energy, Environment and Health 2024 (ICAMEEH 2024)*, September 24-27, Adelaide, Australia, 2024.
2. **Mao, S.**, Zhang, S., Feng, A., Shi, Y., Onggowarsito, C, Su, D., Nghiem, L. D. & Fu, Q. Structure Design of Polymeric Hydrogels for Solar Vapor Generator based Seawater Desalination, *2024 NSWPoly Early Career Researcher Symposium,* November 8, Sydney, Australia, 2024.
3. **Mao, S.**, Zhang, S., Feng, A., Shi, Y., Onggowarsito, C, Su, D., Nghiem, L. D. & Fu, Q. Polymeric hydrogel membranes for solar vapor generator based seawater desalination, *Membrane Society of Australasia Annual Meeting And Conference 2024 (MSA-AMC 2024)*, December 9-11, Sydney, Australia, 2024.

Poster presentation:

1. **Mao, S.**, Feng, A., Zhang, S., Onggowarsito, C, Chen, Q., Su, D. & Fu, Q. Investigation of structure-property-application relationships of the hydrogel-based solar vapor generator, *2023 NSWPoly Early Career Researcher Symposium*, October 20, Sydney, Australia, 2023.

Table of Contents

Certificate of Original Authorship i

Acknowledgements ii

List of Publications iv

Conference Presentations vii

Table of Contents viii

List of Abbreviations xiv

List of Tables xvii

List of Figures xviii

Abstract xxviii

CHAPTER 1 1

Introduction 1

1.1 Background 2

1.2 Research Objectives 5

1.3 Thesis Outline 6

CHAPTER 2 9

Literature Review 9

2.1 Introduction 10

2.2 Solar-thermal Conversion Enhancement 14

2.2.1 Photothermal Materials 15

2.2.2 Surface Topography Modification 23

2.2.3 Reducing Heat Loss 27
2.3 Enhancing water transport/activation capacity 30
2.3.1 Adjusting the Wettability 31
2.3.2 Tuning Internal Water Channels 32
2.4 Water Activation 35
2.5 Conclusions and Remaining Challenges 38
CHAPTER 3 41
Chemicals and Characterizations 41
3.1 Introduction 42
3.2 Chemicals 42
3.3 Characterizations 42
3.3.1 Zeta Potential 42
3.3.2 Scanning Electron Microscope (SEM) 43
3.3.3 Fourier Transform Infrared Spectroscopy (FT-IR) 43
3.3.4 UV-visible-NIR (UV-vis-NIR) 43
3.3.5 Raman Spectra 43
3.3.6 Differential Scanning Calorimetry-Thermogravimetric Analysis (DSC-TGA) 43
3.3.7 DSC 44
3.3.8 Viscosity Test 44
3.3.9 Tensile Test 44

3.3.10 Contact Angle 44
3.3.11 Inductively Coupled Plasma Mass Spectrometry (ICP-MS) 45
3.3.12 UV-Vis Spectroscopy 45
3.3.13 Total Dissolved Solids (TDS) 45
CHAPTER 4 46
Nanoscale: Interaction Between Water Molecules and Hydrophilic Groups 46
4.1 Introduction 47
4.2 Experimental Section 50
4.2.1 Chemicals 50
4.2.2 Synthesis of Hydrogels in Acid Condition 51
4.2.3 Synthetic Procedure for Other Hydrogels 51
4.2.4 Characterizations 52
4.2.5 Simulation Study 53
4.2.6 Interfacial Solar Steam Generation Tests 53
4.3 Results and Discussion 54
4.3.1 Hydrogels' Chemical Structure and Morphology 54
4.3.2 Hydrogels' Light Absorption and Water Uptaking Capability 58
4.3.3 Water Interaction Within the Hydrogels 59
4.3.4 ISSG Tests 64
4.3.5 Desalination Performance in Real Seawater 67
4.4 Conclusion 69

CHAPTER 5 71
Microscale: Efficient Water Transport in Optimized Pore Structures 71
5.1 Introduction 72
5.2 Experimental Section 75
5.2.1 Chemicals 75
5.2.2 Synthesis of PVA-based Hydrogels 75
5.2.3 Synthesis of PHEA-based Cryogels 76
5.2.4 Synthesis of PPEG-based Cryogels 76
5.2.5 Characterizations 77
5.2.6 Interfacial Solar Steam Generation Tests 77
5.3 Results and Discussion 78
5.3.1 Pore Construction in Hydrogels and Cryogels 78
5.3.2 Hydrogels' Water Transport Capability 82
5.3.3 Hydrogels' Chemical Structure and Light Adsorption Capability 83
5.3.4 Intermediate Water Content 85
5.3.5 ISSG Tests 86
5.3.6 Desalination Performance in Real Seawater 92
5.4 Conclusion 93
CHAPTER 6 95
Scale Up Hydrogel Fabrication via 3D Printing 95
6.1 Introduction 96

6.2 Experimental Section 99
6.2.1 Chemicals 99
6.2.2 Development of 3D Printing Inks 99
6.2.3 3D Printing of Hydrogels 100
6.2.4 Characterizations 101
6.2.5 Interfacial Solar Steam Generation Tests 102
6.3 Results and Discussion 102
6.3.1 The Development of 3D Printing Ink 102
6.3.2 3D Printed Hydrogels' Chemical Structure and Morphology 108
6.3.3 3D Printed Hydrogels' Mechanical Strength, Hydrophilicity and Light adsorption 110
6.3.4 Water Interaction within the 3D Printed Hydrogels 111
6.3.5 ISSG Tests 113
6.4 Conclusion 117
CHAPTER 7 118
Micro/Macrostructure Design for Hydrogel Water and Heat Balance via 3D Printing and Real Outdoor ISSG 118
7.1 Introduction 119
7.2 Experimental Section 121
7.2.1 Chemicals 121
7.2.2 Preparation of 3D Printing Ink 121

7.2.3 3D Printing of Hydrogels 121
7.2.4 Characterizations 122
7.2.5 Outdoor Experiments 124
7.3 Results and Discussion 125
7.3.1 3D Printed Hydrogels' Chemical Structure and Morphology 125
7.3.2 Intermediate Water within the 3D Printed Hydrogels 128
7.3.3 Water and Heat Balance during ISSG Tests 129
7.3.4 Desalination and Wastewater Purification Performance 132
7.3.5 Real Outdoor Desalination 134
7.4 Conclusion 136
CHAPTER 8 137
Conclusion and Recommendation 137
8.1 Conclusions 138
8.2 Recommendations for Future Works 141
References 146

List of Abbreviations

AA	Acrylic acid
AETAC	[2-(acryloyloxy)ethyl]trimethylammonium chloride
AMPSA	2-acrylamido-2-methyl-1-propanesulfonic acid
APS	Ammonium persulfate
BW	Bond water
DI	Deionized
DIW	Direct Ink Writing
DLP	Digital Light Processing
DMA	N,N-dimethylacrylamide
DSC	Differential Scanning Calorimetry
EEW	Equivalent vaporization enthalpy of water
EPE	Expanded polyethylene
FT-IR	Fourier transform infrared spectroscopy
FW	Free water
GA	Glutaraldehyde
GO	Graphene oxide
HCl	Hydrochloric acid
HEA	2-hydroxyethyl acrylate
ICP-MS	Inductively Coupled Plasma Mass Spectrometry
IR	Infrared

ISSG	Interfacial Solar Steam Generation
IW	Intermediate water
LAP	Lithium phenyl-2,4,6-trimethylbenzoylphosphinate
LN	Liquid nitrogen
LSPR	Localized Surface Plasmon Resonance
MB	Methyl blue
MBA	*N,N'*-methylenebis(acrylamide)
NaCl	Sodium chloride
PAM	Polyacrylamide
PEGDA	Poly(ethylene glycol) diacrylate
PPy	Polypyrrole
PTM	Photothermal material
PVA	Poly(vinyl alcohol)
SEM	Scanning electron microscope
T_g	Glass transition temperature
TDS	Total Dissolved Solids
TE	Thermoelectric
TEMED	*N,N,N',N'*-tetramethyl-ethylenediamine
TGA	Thermogravimetric Analysis
UV	Ultraviolent
VC	L-Ascorbic acid

WHO	World Health Organization

List of Tables

Table 4.1 The mass of the monomer and crosslinker used for the synthesis of the corresponding hydrogel. 52

Table 4.2 The energy E_0 and E_1 output by the *Avogadro*, and the simulated hydrogen bonding energy E_{hyd} of IW. 61

Table 5.1 The average pore size and wall thickness of all the samples calculated from the cross-section SEMs via 'Imagej'. 81

Table 5.2 The calculated equivalent water evaporation enthalpy in the gel samples at the surface equilibrium temperature. 88

Table 5.3 List of the ISSG performance of the hydrogels in previous work with similar testing setup. 90

Table 6.1 The development of 3D printing ink for DLP. The concentration of GO is the same in all formulations (0.5 mg mL^{-1}). 104

Table 6.2 Evaporation rates and polymer mass loading of the DLP 3D printed hydrogels from previous work. 115

Table 6.3 Evaporation rates and polymer mass loading of the DIW 3D printed hydrogels from previous work. 116

List of Figures

Figure 1.1 Comprehensive diagram of thesis structure. 8

Figure 2.1 Schematic illustrations of a single slope (a) solar still and (b) hydrogel based material platform for solar water purification. 12

Figure 2.2 SEM images of different surface topography: (a−c) G-SH, (d−f) F-SH and (g−i) D-SH. (j) The underwater oil (1,2-dichloroethane) contact angle of each modified surface. (k) The optical profilometer test results revealed the surface area and root-mean-square (RMS) roughness of each sample. (l) The water mass changes, (m) water evaporation rates and energy conversion efficiencies of different samples under 1 sun. Reproduced with permission (Guo, Zhao, et al., 2019). Copyright 2019, American Chemical Society. 24

Figure 2.3 Spatial distribution of PTMs in HHE 3. Photographs of (a) fully swollen HHE 3; (b) cross-section of freeze-dried HHE 3; (c) SEM image of the top portion of HHE 3; the corresponding EDS mappings of (d) C and (e) iron elements. (f) Schematic illustration of solar water purification using HHEs. (g) Under 1 sun irradiation, the temperatures at both the hydrogel evaporator surface and in the bulk water. (h) COMSOL simulation results of the temperature distribution of a control sample (pure PVA hydrogel with uniformly distributed absorbers) and HHE 3. Reproduced with permission (Y. Guo, H. Lu, et al., 2020). Copyright 2020, John Wiley and Sons. 27

Figure 2.4 (a-c) Schematic illustration of patchy-surface hydrogels (PSHs). (d-k) Optical

images and contact angles of PSHs with (d and h) 0%, (e and i) 30%, (f and j) 60%, and (g and k) 90% OTS covered surfaces. The scale bars are all 20 mm. (l) PSHs' evaporation rates and corresponding energy conversion efficiencies under 1 sun. Reproduced with permission (Y. Guo, X. Zhao, et al., 2020). Copyright 2020, Royal Society of Chemistry. 31

Figure 2.5 (a) Schematic illustration of the water transport in tree from root to the top with the SEM images of the top and bottom of wood. (b) Schematic illustration of the direction freezing method. (c) Water mass loss for pure water, MM, n-TIH3, and TIH3 under 1 sun. Reproduced with permission (Yu & Wu, 2020). Copyright 2020, John Wiley and Sons. (d) Evaporation rates and energy conversion efficiencies of MoCC-CHs. Reproduced with permission (F. Yu et al., 2020). Copyright 2020, American Chemical Society. (e-f) SEM images of radially aligned channels and micropores. (g) Schematic illustration of the radial freezing method. (h) Water transport distance over time. (i) Water evaporation rate and energy conversion efficiency of PAAm-based aerogels with different channel directions. Reproduced with permission (Xu et al., 2019). Copyright 2019, American Chemical Society. 33

Figure 2.6 (a) Schematic illustration of ISSG based on h-LAH. (b) Water state in h-LAH. (c) In h-LAHs, the IW/FW ratio. (d) Bulk water and the water in h-LAHs' equivalent water vaporization enthalpy. Reproduced with permission (Zhou, Zhao, et al., 2019b). Copyright 2019, American Association for the Advancement of Science. (e) The melting activity of IW in various frozen IPNGs as depicted by DSC curves. (f) Solar water

purification with conrrolled hydration based on IPNG. (g) IPNGs' solar evaporation rate and energy conversion efficiency under 1 sun. Reproduced with permission (X. Zhou et al., 2020). Copyright 2020, John Wiley and Sons.....35

Figure 4.1 (a) Schematic illustration of the preparation of the hydrogel ISSGs. (b) Chemical structures of the monomers, cross-linker and initiator.....54

Figure 4.2 (a) FT-IR spectra of PAMPSA-GO, PAA-GO, PHEA-GO, PPEG-GO, PDMA-GO, PAM-GO and PAETAC-GO. Cross-section SEM figures of the fabricated hydrogels: (b) PAM-GO, (c) PAMPSA-GO, PAA-GO, PHEA-GO, PPEG-GO, PDMA-GO, and PAETAC-GO. Among them, PPEG-GO, PDMA-GO and PAM-GO have micropores distribution on their macroporous walls.....56

Figure 4.3 (a) UV-vis-NIR spectra of all the hydrogels and the solar spectrum (AM 1.5 G) with normalised spectral solar irradiance density (the light-yellow region) spanning the wavelength range of 280-2,500 nm. The water absorbed in the gel per gram of the dried gel plotted versus the absorption time within (b) 24 hours and (c) 30 s. 58

Figure 4.4 The molecule model and the automatic computed energy of (a) the -NH_2 group in PAM connected with two water molecules via hydrogen bonding and (b) the moment of dragging the second water molecule to break the hydrogen bonding between the water molecules. (c) Electrostatic Potential Maps of the polymer repeating unit. 61

Figure 4.5 The fitting curves for (a) PAMPSA-GO, (b) PAA-GO, (c) PHEA-GO, (d) PPEG-GO, (e) PDMA-GO, (f) PAM-GO, and (g) PAETAC-GO in their Raman spectrum, and the pink and light blue peaks correspond to free and intermediate water, respectively.

The inset figures are the schematic illustration of the water molecule configuration. (h) The IW:(IW+FW) ratios of all the hydrogels calculated from their Raman spectrum in the O-H stretching energy area. (i) The equivalent water vaporization enthalpy of the water in the hydrogels, the green enthalpy drop represents for the enthalpy reduced by the interaction between the water molecules and corresponding hydrophilic group. 63

Figure 4.6 (a) Schematic illustration of the ISSG setup. (b) The infrared images of the PAM-GO at the 0 minute, 15 minutes, 30 minutes, 45 minutes and 60 minutes during the ISSG testing. (c) The surface temperatures and bulk water temperatures of the hydrogels calculated from the infrared images during one-hour ISSG testing under one sun. (d) Water mass loss of the hydrogels and pure water under one sun. Notably, all of the data were calibrated with dark evaporation data. (e) Structure-property-application relationships of the polymeric hydrogels. 64

Figure 4.7 PAM-GO hydrogel based SVG desalination performance. (a) The evaporation rates of PAM-GO after being exposed to seawater for different days in 15 days. Insets: Solar vapor generation performance after one and two weeks of exposure to seawater. (b) The sealed jar for the condensed water collection. (c) The four primary ion concentrations of the seawater and the condensed water. (d) The total dissolved solids of the seawater and the condensed water..... 67

Figure 4.8 Evaporation rates of the hydrogels in real seawater. 69

Figure 5.1 (a) Schematic of the preparation process of the gels and the schematic of chemical structures of all the components during the gelation of (b) PVA gels, (c) PHEA

gels, and (d) PPEG gels.....78

Figure 5.2 Schematic diagram of the formation process of the (a) hydrogel and (b) cryogels. During the freezing process, (I) the ice crystals firstly generated and then (II) grew bigger with or without limitation of the polymer chains. (III) After thawing, the final gels with pores were obtained. Cross-section SEM images of (c) PVA-GO-5, (d) PVA-GO-10, (e) PHEA-GO-5, (f) PHEA-GO-10, (g) PPEG-GO-5, and (h) PPEG-GO-10 gels from a top-view. 80

Figure 5.3 The porous structure shown via cross-section SEM image of PPEG-GO-10-LN. 82

Figure 5.4 The water content of (a) the gel frozen at -18 ºC and (b) the gel rapid frozen by liquid nitrogen per gram of the corresponding dry gel plotted against water absorption time (the right figure represents for the first 200 minutes of water absorption). (c) The saturated water content in the well-saturated gel per gram of the corresponding xerogel. 83

Figure 5.5 (a) FT-IR spectra of the PVA-GO-10, PHEA-GO-10, and PPEG-GO-10 gels showing their hydrophilic groups. (b) UV-vis-NIR spectra of the gels and the solar spectrum of air mass 1.5 global (AM 1.5 G) with normalised spectral solar irradiance density (the light yellow area) over the wavelength of 300-2,500 nm.....84

Figure 5.6 Fitting curves in the O-H stretching energy region for (a) PVA-GO-5, (b) PHEA-GO-5, (c) PPEG-GO-5, (d) PVA-GO-10, (e) PHEA-GO-10 and (f) PPEG-GO-10 in Raman spectrum. The pink peaks and light blue peaks represent free water and

intermediate water, respectively. 85

Figure 5.7 (a) The setup for the ISSG test. (b) The temperatures of the gel surface and bulk water during the one hour of ISSG test under 1 sun. (c) Water mass changes of PVA hydrogels, PHEA cryogels, PPEG cryogels and the pure water without any gels during the solar steam generation test under 1 sun irritation. All the data have been calibrated with dark evaporation data and were estimated by the slopes of the mass−time curve via linear fitting. (d) Water mass changes of PPEG-GO-10, PPEG-GO-10-LN, and the pure water during the solar steam generation test under one sun irritation. (e) The calculated equivalent water vaporization enthalpy in the gel samples at various temperatures by DSC-TGA. (f) Comparison of the evaporation rate and energy efficiency to the hydrogel ISSGs in previous works with similar testing setup (The testing gel is fixed in the middle of a floating foam and the gel itself can directly contact the bulk water. Notely, the gel surface should not be much high above the foam surface). Detailed data are listed in Table 5.3. 86

Figure 5.8 The evaporation rates and corresponding solar-to-vapor energy efficiencies of gels with (a) 5 wt% polymers and (b) 10 wt% polymers. We take the equivalent water evaporation enthalpy at the gel surface temperature for the calculation of energy efficiency. Each error bar shows the difference from at least two gel samples. 89

Figure 5.9 Desalination performance of the cryogels. Evaporation rates of (a) PHEA-GO-10 and (b) PPEG-GO-10 immersed in real seawater for half a month. Insets: ISSG performance after seven and fourteen days of exposure to seawater. (c) The setup for

desalination and condensed water collection. Four major ions concentrations measured in real seawater both before and after solar desalination via (d) PHEA-GO-10 and (e) PPEG-GO-10. (f) Total dissolved solids of the seawater and the desalinated water of PPEG-GO-10 and PHEA-GO-10. 92

Figure 6.1 (a) Schematic illustration of the bottom-up DLP 3D printing method, (b) the chemical structures of the constituents in the printing ink, and (c) the evolution of the polymer network throughout the UV-induced radical polymerization and post-treatment. 104

Figure 6.2 Morphology and chemical structure of the 3D printed hydrogels. For the 3D printed 5PVA15PHEA-C: (i) designed 3D model, (ii) physical image, (iii) longitudinal cross section optical image, (iv) longitudinal cross-sectional SEM image, (v) the zoom-in cross-sectional SEM image, (vi) top view SEM image, and (vii) the zoom-in top view SEM image. (b) Physical image of a 3D pattern (with a total height of 4 mm and 2 mm depth of “UTS” patterns). The cross-section SEM images of the pore structure in the concave 3D printed hydrogel of (c) 5PVA20PHEA-C and (d) 10PVA15PHEA-C, respectively. (e) FT-IR spectra of the 5PVA15PHEA-C, 5PVA20PHEA-C, and 10PVA15PHEA-C hydrogels. The control sample is a pristine 5 wt% PVA hydrogel directly crosslinked with GA. 108

Figure 6.3 (a) The 3D model of ASTM (E8) subsize standard hydrogel specimen for tensile test, and (b) the 3D printed hydrogels from the model. (c) Stress-strain curve of the printed 5PVA15PHEA hydrogel in the tensile test. The contact angle test of 3D printed

5PVA15PHEA hydrogel at (d) 0 s and (e) 0.08 s. (f) UV-vis-NIR adsorption spectrum of the 3D printed 5PVA15PHEA hydrogel and the air mass 1.5 global (AM 1.5 G) solar spectrum with normalized spectral solar irradiance density (the light-yellow region) in the wavelength range from 300 to 2,500 nm. 110

Figure 6.4 (a) The water content vs absorption time of 3D printed hydrogels. The unit is measured gram of water per gram of dry gel. Fitting curves for the (b) 5PVA15PHEA-C, (c) 5PVA20PHEA-C, and (d) 10PVA15PHEA-C hydrogels in the Raman spectra within the O-H stretching energy region. Free water is indicated by the green peaks, whereas intermediate water by blue peaks. Raw DSC curves and the equivalent water vaporization enthalpies calculated from the integrated area of (e) 5PVA15PHEA-C, (f) 5PVA20PHEA-C, and (g) 10PVA15PHEA-C hydrogels, respectively. 112

Figure 6.5 The ISSG performance of the printed hydrogels. (a) A home-made set up for the SSG test. (b) Water mass changes under one sun irritation condition for 5PVA15PHEA-C, 5PVA20PHEA-C, and 10PVA15PHEA-C hydrogels, respectively (in DI water). (c) The temperature variations of the 5PVA15PHEA-C, 5PVA20PHEA-C, and 10PVA15PHEA-C hydrogel surfaces and bulk water during the SSG test under one sun irritation. (d) Comparison of the evaporation rates and precursor concentrations to state-of-the-art DLP (Liu & Zheng, 2024; Sun et al., 2023; Xiao et al., 2024; Yang et al., 2024; Zhan et al., 2023; Zheng et al., 2023) and DIW (Huang et al., 2024; Li et al., 2023; Liu et al., 2023; Yuan et al., 2021; S. Zhang et al., 2024) 3D-printed ISSGs (typical three-dimensional ISSGs were not included). Detailed data are listed in Tables 6.2 and 6.3. 114

Figure 7.1 Schematic illustration of the custom-designed outdoor SSG device..... 125

Figure 7.2 (a) Schematic illustration of the bottom-up DLP 3D printing method. For the 3D printed 5PVA15PHEA-N (b), 5PVA15PHEA-H (c), and 5PVA15PHEA-C (d) hydrogels: (i) designed 3D models, (ii) physical images, (iii) longitudinal cross section optical images, (iv) cross-sectional SEM images, and (v) the zoom-in SEM images showing the pores on the raised node structure of 5PVA15PHEA-N, the hole wall of 5PVA15PHEA-H, and the concave structure of 5PVA15PHEA-C, respectively. 126

Figure 7.3 FT-IR spectra of the 3D printed 5PVA15PHEA-N, H, C hydrogels. A control sample of pristine 5 wt% PVA hydrogel is included. 127

Figure 7.4 Fitting curves for the (a) 5PVA15PHEA-N, (b) 5PVA15PHEA-H, and (c) 5PVA15PHEA-C hydrogels in the Raman spectrum within the O-H stretching energy region. Free water is represented by the green peaks, whereas intermediate water is represented by the blue peaks. Raw DSC curves and the equivalent water vaporization enthalpies calculated from the integrated area of (d) 5PVA15PHEA-N, (e) 5PVA15PHEA-H, and (f) 5PVA15PHEA-C hydrogels, respectively. 128

Figure 7.5 The SSG performance of the printed hydrogels. (a) A home-made set up for the SSG test. The schematic illustrating of the (b) water transport and (c) thermal transfer in 5PVA15PHEA-N, 5PVA15PHEA-H, and 5PVA15PHEA-C. (d) Water mass changes under 1 sun irritation condition for 5PVA15PHEA-N, H, C hydrogels, and pure water. (e) The temperature variations of the 5PVA15PHEA-N, H, and C hydrogel surfaces and bulk water during the SSG test under one sun irritation. The infrared images showing the

temperature equilibrium of these three differently shaped hydrogels after one hour of irritation are displayed on the right. (f) The graph showing the link between the water absorption time and the water content per gramme of the corresponding dry gel. 130

Figure 7.6 (a) The evaporation rates of 5PVA15PHEA-C, N, H in DI water, seawater and simulated brine (20 wt% NaCl solution). (b) Evaporation rates of 5PVA15PHEA-C in seawater over two weeks. Insets: SSG performance after six and fourteen days of seawater exposure. (c) Four significant ion concentrations in seawater before and after the desalination of 5PVA15PHEA-C, N, and H hydrogel based solar steam generators. (d) The physical images of self-desalting behavior of 5PVA15PHEA-C, N, and H hydrogels. (e) The UV-vis spectra of simulated wastewater containing dye (MB) before and after the purification of 5PVA15PHEA-C hydrogel based solar steam generator. Insert: the optical photos of the MB solution before and after SSG. 132

Figure 7.7 (a) Physical image of the 3D printed larger 5PVA15PHEA-C hydrogels (with a diameter of 4 cm) for outdoor SSG. (b) The digital photo of our outdoor SSG device. (c) The environment temperature, humidity, and solar light intensity during the day of outdoor SSG test on 7th October 2024 in Sydney, Australia. 135

Abstract

Water scarcity, as an increasingly pressing global issue, has posed a serious threat to human health and world peace. Without requiring any extra energy input, Interfacial Solar Steam Generation (ISSG) offers a promising complement to current energy-intensive freshwater production technologies.

Both thermal and water managements play crucial roles in governing the performance of ISSG systems. However, thermal management alone such as enhancing light capture and solar-thermal conversion cannot surpass the theoretical evaporation rate limit of 1.59 kg m^{-2} h^{-1} under one-sun irradiation (1 kW m^{-2}). By utilizing polymeric hydrogels, equivalent evaporation enthalpy of water (EEW) can be lowered through hydrogen bonding, activating surrounding water molecules and facilitating evaporation. Despite this potential, insufficient understanding of the structure-property relationships between hydrogels and water molecules limits the advancement of efficient hydrogel-based ISSG systems.

This thesis investigates the interactions of polymeric hydrogels with water molecules across nano-, micron-, and macro-scales. At nanoscale, seven different hydrogels with diverse functional groups were synthesized, and their relationships with key properties (*e.g.*, evaporation enthalpy, electrostatic potential) and the corresponding hydrogels' ISSG performance were systematically investigated. Hydrophilic groups were ranked based on their influence on ISSG potential as follows: $-N^{+}(CH_3)_3Cl^{-}$ < $-SO_3H$ < -COOH

< -OH < -C-O-C- < -$N(CH_3)_2$ < -NH_2. Among the tested hydrogels, polyacrylamide (PAM) ISSG containing -NH_2 groups demonstrated superior performance, characterized by rapid water replenishment capability, a high intermediate water (IW) content of 78.2%, low EEW, and an exceptional seawater evaporation rate of 3.41 kg m^{-1} h^{-1}.

At microscale, interconnected pores were constructed by selecting polymer precursors with appropriate glass transition temperatures (T_g), and employing freeze-thaw processing. This approach facilitated water transport, enabling continuous evaporation and achieving an enhanced evaporation rate of 3.59 kg m^{-1} h^{-1}.

Finally, at macroscale, Digital Light Processing (DLP) 3D printing was employed to scale up hydrogel fabrication with optimized monomer consumption by adding poly(vinyl alcohol) (PVA) for improved printability and ensuring consistent layer-by-layer printing. This methodology enabled the successful fabrication of hydrogels with intricate macro/microstructures, allowing tailored control over water and heat transport properties while utilizing record-low polymer dosages. The resulting hydrogels exhibited high porosity, enhanced water uptake, low EEW, and a high evaporation rate of 3.56 kg m^{-2} h^{-1}.

My PhD research has achieved remarkable advancements in freshwater production from seawater and wastewater, representing several significant breakthroughs in ISSG for sustainable water treatment applications.

Keywords: Interfacial Solar Steam Generation, Polymeric hydrogels, Structure-property relationship, Water treatment, 3D-Printing

CHAPTER 1
Introduction

1.1 Background

Water, as a vital element of life, is one of the most crucial resources for both ecological health and economic growth. However, freshwater demand has increased nearly eightfold in recent decades (Wada et al., 2016) because of rapid population growth, climate change, economic progress, and agriculture industrialization (Chakkaravarthy, 2019; Immerzeel et al., 2010). The Massachusetts Institute of Technology MIT Integrated Global System Model for Water Resources forecasts that by 2050, approximately 52% of the world's projected population of 9.7 billion would live in areas facing water scarcity (Schlosser et al., 2014). What's more, this increasing water scarcity is likely to escalate conflicts over resources, raise the risk of food insecurity and crop failures, and pose a significant threat to global peace and public health ((FAO), 2012; UNESCO & UN-Water, 2024). Therefore, it's urgent to develop efficient, affordable, and scalable technologies to produce fresh water from abundant sources like seawater, brackish water, and wastewater, independent of the hydrological cycle.

Hydrogel based Interfacial Solar Steam Generation (ISSG) is an innovative technique that utilizes the renewable and abundant solar energy to evaporate the seawater or wastewater absorbed in the hydrogels, and then the vapor generated can be condensed to obtain freshwater (Deng et al., 2017; Ma et al., 2017; Mao et al., 2022; Neumann et al., 2013; Onggowarsito et al., 2024; Shi et al., 2024; Xu et al., 2020; Zhao et al., 2018; Zhou, Guo, et al., 2019; Zhou et al., 2018; Zhu et al., 2021). Compared to the traditional solar still (Y.

Zhang et al., 2018), the utilization of the polymeric hydrogels can activate water molecules, lowering the equivalent vaporization enthalpy of water (EEW) and significantly boosting the freshwater productivity. This approach has garnered significant interest due to its zero additional energy input and high freshwater yield, positioning it as a promising and cost-effective solution for next-generation water purification (Deng et al., 2017; Ma et al., 2017; Mao et al., 2022; Neumann et al., 2013; Onggowarsito et al., 2024; Shi et al., 2024; Xu et al., 2020; Zhao et al., 2018; Zhou, Guo, et al., 2019; Zhou et al., 2018; Zhu et al., 2021).

In the ISSG system, the composite hydrogel commonly comprises a polymeric hydrogel, which serves as the main component for water management and thermal insulation, and a photothermal material (PTM), which absorbs sunlight and converts it into energy for evaporation. Considerable efforts have been directed towards developing advanced photothermal materials (Ibrahim et al., 2021; Y. Wang et al., 2021; Yang et al., 2020) to enhance light absorption and maximize photothermal conversion efficiency. However, without the polymer network, even if both the light absorption and improved photothermal conversion efficiency reach 100%, the ISSG evaporation rate is still capped at the theoretical maximum of 1.59 kg m^{-2} h^{-1} under solar radiation of 1 kW m^{-2} (Chen et al., 2022; T. Li et al., 2021). Thus, polymeric hydrogel with unique water interactions has become the critical breakthrough to exceed evaporation limit and further enhance freshwater productivity.

The unique water interactions within hydrogels encompasses both water activation and water transport, both of which are intricately tied to hydrogel properties. Interactions between polymer chains and water molecules give rise to intermediate water (IW)— a form of water with weakened or partial hydrogen bonds that separates more readily from neighboring molecules (Guo, Zhou, et al., 2019; Zhou, Zhao, et al., 2019a). This phenomenon reduces the equivalent water vaporization enthalpy, enabling more effective evaporation with the same energy input. Furthermore, water transport within porous hydrogels can be regulated by constructing structural pores to facilitate an optimal flow of water to the evaporation interface and supporting continuous vapor generation. However, research into polymeric hydrogels and their interactions with water remains in its infancy, constraining the development of highly efficient ISSG systems.

Therefore, to advance next-generation hydrogel-based ISSG systems with high efficiency and practical applicability, it is essential to urgently address the following key challenges in hydrogel development across the nano, micro, and macro scales.

- **Influence of polymeric network structure on IW generation**: Investigating how variations in the chemical structure of the polymeric network impact IW formation and subsequently optimize ISSG performance.

- **Optimization of hydrogel pore structures**: Developing strategies to construct appropriate pore architectures that enhance water transport while maintaining continuous, high-efficiency evaporation.

- **Scalability of hydrogel fabrication**: Establishing methods for scaling up hydrogel fabrication processes without compromising ISSG performance, enabling future large-scale industrial applications.

- **Macrostructural regulation of hydrogels**: Exploring precise techniques to regulate the macrostructure of hydrogels to further enhance their ISSG efficiency.

1.2 Research Objectives

The aim of this thesis is to design and develop advanced polymeric hydrogels optimized across nano, micro, and macro scales to achieve enhanced-efficiency ISSG. overarching goal is addressed through the following specific sub-objectives:

1. Designing polymeric hydrogels with enhanced freshwater productivity. This involves identifying and integrating optimal hydrophilic groups by thoroughly understanding the interactions between water molecules and hydrophilic groups and their correlation with the ISSG performance of hydrogels.
2. Developing polymeric hydrogels with optimal pore structures. Employing a facile cost-effective method to construct hydrogels with pore architectures that facilitate water transport, ensuring rapid replenishment to the evaporation interface for efficient and continuous evaporation.
3. Scaling up high-precision hydrogel fabrication. Utilizing Digital Light Processing (DLP) 3D printing technology to achieve large-scale production of hydrogels, while overcoming challenges related to preserving high porosity to ensure excellent ISSG

performance.

4. Optimizing hydrogel micro/macro structures. Leveraging 3D printing to regulate the macrostructural design of hydrogels, achieving a balanced water and thermal management system to further enhance ISSG performance on a macroscale.

1.3 Thesis Outline

This thesis is divided into eight chapters, as outlined below:

Chapter 1: Introduction: This chapter emphasizes the urgency of addressing global water scarcity and presents the advantages of emerging ISSG technology in efficient freshwater extraction. It also identifies the existing technical challenges of ISSG and outlines the objectives of this thesis to advance the technology.

Chapter 2: Literature Review: This chapter summarizes recent advancements in hydrogel-based ISSG, focusing on key strategies to improve performance and addressing the remaining challenges.

Chapter 3: Chemicals and Characterizations: This chapter outlines the chemicals used for hydrogel synthesis in this thesis and details the characterization methods employed to analyze the chemical and physical properties of the materials, the water interactions within the hydrogels, and the water quality before and after ISSG.

Chapter 4: Nanoscale: Interaction Between Water Molecules and Hydrophilic

Groups: This chapter focuses on designing polymeric hydrogels at the nanoscale by examining how variations in the chemical structure of polymer chains influence their interactions with water molecules. Detailed investigations include analyzing swelling ratios and water replenishment capabilities, quantifying IW contents and evaporation enthalpies, and simulating the energy differences involved in IW detachment.

Chapter 5: Microscale: Efficient Water Transport in Optimized Pore Structures: This chapter focuses on the design of polymeric hydrogels at the microscale by constructing interconnected macropores to enable rapid water replenishment for continuous ISSG. This was achieved through the judicious selection of polymer precursors with glass transition temperatures (T_g) below the freezing point.

Chapter 6: Scale Up Hydrogel Fabrication via 3D Printing: This chapter focuses on scaling up the hydrogel fabrication via using DLP 3D Printing, and a novel printing formulation is proposed to overcome the problem of overly dense hydrogels in conventional DLP 3D printing. This low precursor concentration formulation enhances the hydrogel's porosity, water content, and absorption rate, enabling scalable production while preserving high mechanical strength and SSG performance.

Chapter 7: Micro/Macrostructure Design for Hydrogel Water and Heat Balance via 3D Printing and Real Outdoor ISSG: This chapter explores the design of micro/macrostructures in polymeric hydrogels using DLP 3D printing to achieve an optimal balance between water and heat management, further enhancing SSG

performance. Additionally, a custom outdoor device with integrated condensation features was developed for real-world solar water purification applications.

Chapter 8: Conclusion and Recommendation: This chapter highlights the key insights from the preceding chapters and presents recommendations for the future development of hydrogel-based ISSG technology.

The thesis outline is also presented in Figure 1.1.

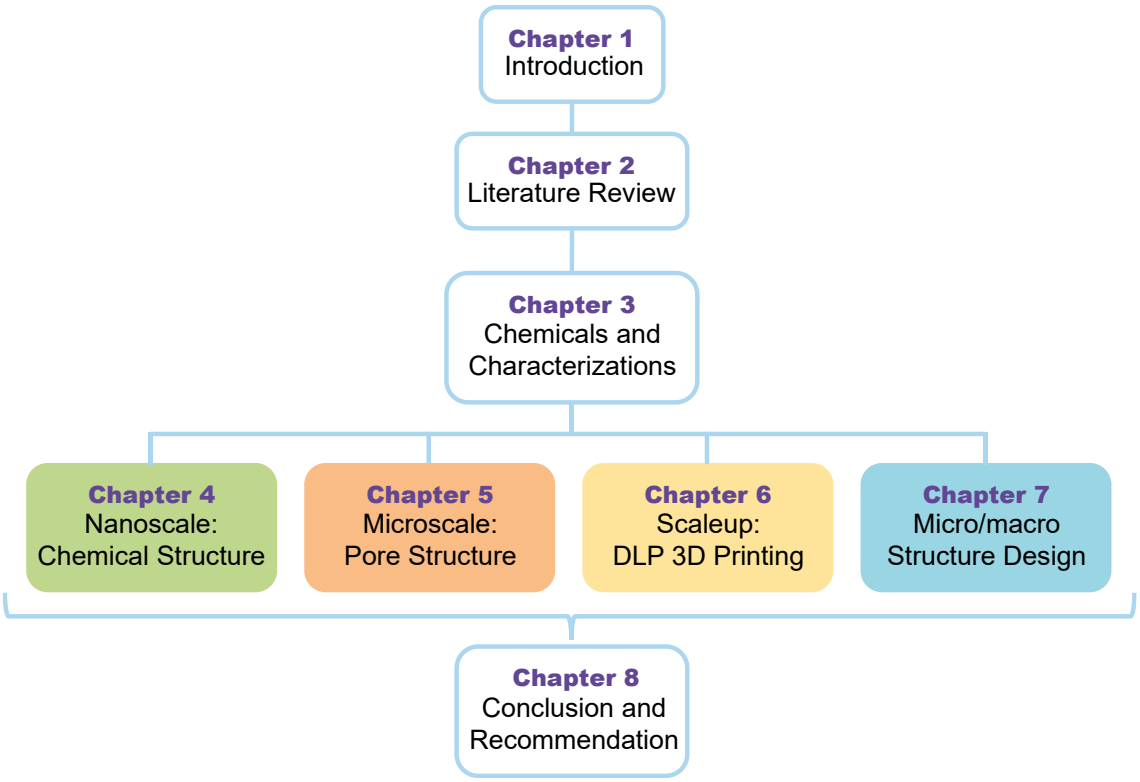

Figure 1.1 Comprehensive diagram of thesis structure.

CHAPTER 2
Literature Review

This chapter has been derived from the published paper of **Mao, S.**, Johir, M., Onggowarsito, C., Feng, A., Nghiem, L., & Fu, Q. (2022). Recent Developments of Hydrogel Based Solar Water Purification Technology. *Materials Advances*, 3(3), 1322-1340.

2.1 Introduction

As an essential substance of life, water is one of the most essential resources for ecological well-beings and economic development. Rapid population growth, economic progress, agriculture industrialisation, dietary changes, and climate change (Chakkaravarthy, 2019; Immerzeel et al., 2010) have led to nearly eightfold increase in fresh water demand between the 1990s and the 2010s (Wada et al., 2016). Despite recent and worldwide economic progress, by 2025, one-third of the world population will still face water scarcity. The Massachusetts Institute of Technology MIT Integrated Global System Model Water Resource System predicted that by 2050, about 52% of the world's projected population (9.7 billion) would live in water-stressed regions (Schlosser et al., 2014). Therefore, there is an ever increasing need to develop efficient, affordable and scalable purification technologies to obtain fresh water from abundant sources such as seawater, brackish water and wastewater that are independent from the hydrological cycle.

Freshwater can be extracted from the ocean or brackish water sources by thermal distillation or filtration technologies (AlMarzooqi et al., 2014; Goh et al., 2019; Khawaji et al., 2008; Panagopoulos et al., 2019; Semiat, 2008). Thermal distillation processes such as multi-stage flash distillation (Morris, 1993), multiple effect distillation (Bamufleh et al., 2017), and membrane distillation have been widely used for seawater desalination applications, especially in the Middle East. These technologies require significant thermal energy input, thus, many of them are co-located with and utilize waste heat from thermal

power plants to lower energy consumption. Even when co-locating with thermal power plants, the energy consumption of these conventional thermal distillation technologies is still quite high, in the range of 5-60 kWh/m^3 of produced freshwater (Al-Karaghouli & Kazmerski, 2013; Semiat, 2008). Filtration-based water purification technologies, such as reverse osmosis (RO)(Qasim et al., 2019) and electrodialysis (Strathmann, 2010), rely mainly on the separation salt from water via a semipermeable membrane. RO has been commercialized at large scale and can achieve relatively low energy consumption of *ca.* 3-4 kWh/m^3 of produced freshwater from seawater (Ghaffour et al., 2013; Werber et al., 2016; Zhao et al., 2013). However, the RO membrane is susceptible to fouling during operation, and hence frequent chemical cleaning is required (Tang et al., 2018). In the electrodialysis process, cation and anion exchange membranes are used to selectively transport salts away from the saline feedwater solution. Electrodialysis is only suitable for brackish water that is about a fifth of the salinity of seawater(Qasem et al., 2020) and the energy consumption is also quite energy (Al-Amshawee et al., 2020). Hence, most of the current full-scale water purification technologies consume a significant amount of energy and are therefore costly, encouraging the researchers to develop next-generation cost-effective water purification technologies. These cost-effective water purification

technologies will reduce energy consumption or will use renewable energy.

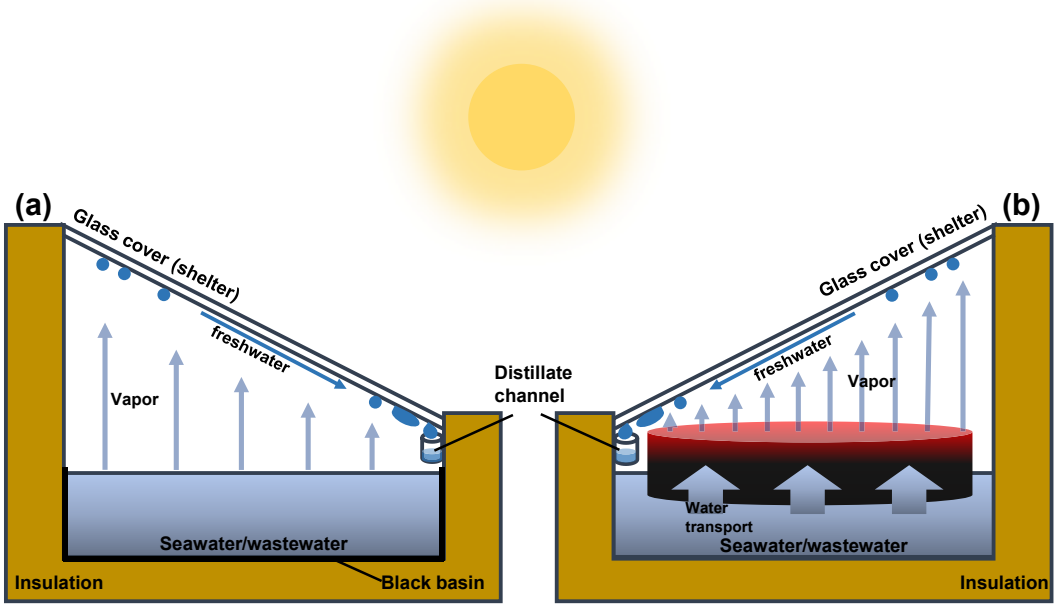

Figure 2.1 Schematic illustrations of a single slope (a) solar still and (b) hydrogel based material platform for solar water purification.

As the most abundant and renewable energy source, solar energy can be used for freshwater production (Duong et al., 2017). Solar still is the simple solar water purification technology (Sharshir et al., 2017). Figure 2.1a illustrates a conventional solar still system, consisting of a sloping glass cover, a black basin with seawater or wastewater, and a thermally insulated enclosure. Because the black basin absorbs solar energy, water evaporates and then condenses on the inner surface of the shelter. As a result, freshwater can be obtained at the cover's lower end. Unfortunately, the solar steam generation efficiency of such solar still system is too low (*ca.* 1-5 L $m^{-2}d^{-1}$) (Y. Zhang et al., 2018) to be widely utilized due to insufficient solar absorption and significant thermal loss. To overcome this challenge, novel hydrogel materials have been introduced and incorporated

into traditional solar still (Figure 2.1b). In this illustrative configuration, the hydrogel is in a swollen equilibrium state and positioned such that it maintains contact with the water reservoir while the upper portion is exposed to sunlight. The thin red layer in Figure 2.1b is above the water surface. It can localize heat in the evaporation interface, reduce heat loss to bulk water, and improve the solar-thermal conversion efficiency, steam generation rate, and freshwater productivity (Guo, Zhou, et al., 2019; Lapotko, 2009; H. Wang et al., 2020; X. Zhang et al., 2020; Zhao et al., 2018). These materials commonly composed of photothermal materials which can transfer solar energy into thermal energy, and porous, low-conductivity, hydrophilic materials that can reduce heat loss and transport water to the evaporation interface. Accordingly, considerable effort has been focused on improving solar-thermal conversion efficiency, enhancing heat insulation, and speeding up water transport. In 2018, Zhao *et al.*(Zhao et al., 2018) introduced a hydrogel-based material to reduce the energy demand for evaporation and improve solar steam generation efficiency. Since then, as a landmark study, it has heightened interest in this field, and more and more publications on hydrogel-based ISSG have appeared recently. While system configurations may vary across studies—for example, some rely on external wicking elements to draw water—hydrogel-based platforms share a unifying design logic: integrating water transport, thermal confinement, and efficient interfacial evaporation within a single material system.

Building upon this foundation, this chapter summarizes the design principles of polymeric hydrogels for ISSG from two primary directions: solar-thermal conversion enhancement

and water management. We also put forward prospects on the future directions and remaining challenges in this field.

2.2 Solar-thermal Conversion Enhancement

Solar–thermal conversion is the core step of ISSG, consisting of light-harvesting, photothermal conversion and heat insulation. The light-harvesting competence of the materials platform, especially the PTMs, is the precondition for attaining sufficient photothermal conversion. Reflection, transmission and absorption might happen to the solar radiation when it strikes the PTMs' surface, but only the absorbed irradiation is the net energy input for subsequent conversion. Thus, PTMs with high irradiation absorptivity and topographical and geometrical designs that reduce reflection and transmission are vital for achieving high conversion efficiency (Xu et al., 2020). The absorbed sunlight energy can be converted into thermal energy by the PTMs instead of being re-emitted. A large number of nanomaterials have been employed as PTMs, and various photothermal conversion mechanisms are presented based on the different interactions between electromagnetic radiation and the specific categories of PTMs (Gao et al., 2019; Liangliang Zhu, Minmin Gao, et al., 2019). In the end, the generated heat will be confined in the evaporation interface layer through the heat insulation designs (Y. Guo, H. Lu, et al., 2020; Tan et al., 2019; X. Zhang et al., 2020) to reduce heat loss to bulk water and thereby improve the efficiency of heat utilization.

Since a diverse array of factors noted above collaboratively contribute to the solar-thermal

conversion competence of the entire ISSG system, the metric solar-to-vapor energy conversion efficiency (η) has been proposed to quantitatively assess its solar-thermal conversion performance, which can be calculated according to equation 1 (Y. Guo, X. Zhao, et al., 2020):

$$\eta = \frac{\dot{m} \times h_v}{C_{opt} \times P_0} \quad (1)$$

where $\dot{m}$, h_v, C_{opt} and P_0 refer to the steady-state evaporation mass flux, the equivalent vaporization latent enthalpy of the water in the hydrogel, the optical concentration on the absorbers' surface, and the solar irradiation power (normally 1 sun or 1 kW m^{-2}), respectively.

In order to enhance energy conversion efficiency, considerable efforts have been devoted to choosing appropriate PTMs, modifying surface topography to reduce light reflection, and mitigating heat loss accordingly.

2.2.1 Photothermal Materials

Choosing an appropriate PTM with full-spectrum strong solar absorption and high solar-thermal conversion capacity is one of the vital design principles. Plentiful nanomaterials have been adapted as PTMs in ISSG, including inorganic semiconductors, plasmonic nanoparticles, carbon-based materials, and conjugated polymers. Different PTMs exhibit diverse solar-thermal conversion mechanisms and thus have different selection principles.

Semiconductors have been extensively used as PTMs due to their highly tunable energy band and inherent thermalization effect (Yu et al., 2017; F. Zhao et al., 2020; Zhao & Burda, 2012). Under light illumination, when the exciting energy is higher than the semiconductors band-gap, electron-hole pairs are generated. Then, electrons and holes relax to the conduction and valence bands' edges, and the energy is released in the form of phonons or photons (Hessel et al., 2011). The non-radiative relaxed phonons can incur lattice localized heating to finally realize the transformation from light to heat (Gao et al., 2019; Liangliang Zhu, Minmin Gao, et al., 2019). In the entire photothermal conversion process, the band-gap width is a critical determinant of the amount of energy and heat that can be released. For the solar spectrum, the majority of the radiant energy lies in the infrared (~52%), visible (~45%) and ultraviolet (~3%) wavelength, ranging from 300 to 2500 nm (Standard, 2012). Since the infrared band occupies the largest proportion, the narrow band-gap semiconductor nanomaterials that can absorb more infrared energy are more suitable as PTMs (F. Zhao et al., 2020).

For instance, as a widely used light-harvesting semiconductor, TiO_2 has been used as PTMs for preparing hydrogel materials (Nabeela et al., 2021; Zhuangzhi Sun et al., 2019; X. Wang et al., 2021; Zhang et al., 2019). However, under 1 sun, these hydrogels showed a low evaporation rate of <1.5 kg m^{-2} h^{-1} and a low energy conversion efficiency of <80%. This can be attributed to the wide intrinsic band-gap of TiO_2 of *ca*. 3 eV, which corresponds to the absorption of UV-light (wavelength <400 nm) (Dette et al., 2014; Tao et al., 2011; F. Zhao et al., 2020). In contrast, the Ti_2O_3 with an extremely narrow band-

gap of ~0.09 eV exhibits excellent energy conversion performance. Guo *et al.*(Guo, Zhou, et al., 2019) incorporated Ti_2O_3 nanoparticles into sponge-like polyvinyl alcohol (PVA) hydrogel with interconnected pores. The resultant Ti_2O_3/PVA hydrogels showed a relatively high solar absorption efficiency of > 96%, a low reflectance over a broadband of the standard solar spectrum, an extremely high evaporation rate of 3.6 kg m^{-2} h^{-1}, and an excellent energy conversion efficiency of *ca.* 90%. In all, semiconducting solar absorbers with a narrow band-gap that can absorb more infrared energy will bring excellent solar-thermal conversion competence to the ISSG system.

Except for TiO_2, MnO_2 (Irshad et al., 2021; X. Li et al., 2021), Co_3O_4 (P. Wang et al., 2019), CuO (X. Li et al., 2021; F. L. Meng et al., 2020; H. Zhang et al., 2020) and other transition metal oxides have been employed as PTMs. Furthermore, transition metal sulfides (such as MoS_2 (C. Li et al., 2020; Y. Li et al., 2021; Q. Wang et al., 2020; Yin et al., 2021), Mo_2S_3 (Z. Guo et al., 2020), and Bi_2S_3 (Geng et al., 2021)), nitrides (such as g-C_3N_4 (Su et al., 2019), TiN (Zhuangzhi Sun et al., 2019), and MoN/Mo_2N (Lin Zhu et al., 2019)), as well as other novel semiconductors (such as MXene(Cao et al., 2020; Y. Chen et al., 2021; Fan et al., 2021; C. Li et al., 2020; W. Li et al., 2020; Yu et al., 2019; Yu & Wu, 2020) and CZTSe (L. Yang et al., 2021; Yang et al., 2019)) have also shown up in recent research progress, mostly with reasonable evaporation rates.

The plasmonic nanomaterials are metallic materials with localized surface plasmon resonance (LSPR) effect, which is the resonant oscillation of free electrons induced by

photons when the frequency of photons matches that of the natural metal surface electrons (Seh et al., 2012; Liangliang Zhu, Minmin Gao, et al., 2019). The LSPR effect causes three consequent phenomena: near-field enhancement, hot electron generation, and photothermal conversion (Gao et al., 2016; Liangliang Zhu, Minmin Gao, et al., 2019). The Photothermal effect aided by plasmon happens when metal nanoparticles are lit at their resonance wavelengths. Hot electrons are generated as the electrons excited from occupied states to unoccupied ones. By electron-electron scattering, the hot electrons decay, and the hot electron energy can be redistributed, leading to the rapid increasing of nanoparticles surface temperature (Liangliang Zhu, Minmin Gao, et al., 2019). Commonly, LSPR spectral band can be expanded by hollow structure, asymmetrical design, particle-size shifts, and dielectric surroundings (Zhu et al., 2018) to compensate for the inherent shortcoming of the narrow absorption spectra of plasmonic nanoparticles caused by their specific geometrics (F. Zhao et al., 2020).

Common plasmonic nanoparticles used as PTMs include Ag (C. Liu et al., 2020; Yanying Shi et al., 2021; Zeyu Sun et al., 2019; Xiao et al., 2020), Au (X. Meng et al., 2020a), CuS (J. Chen et al., 2021; Y. Sun et al., 2019; D. Zhang et al., 2020; D. Zhang et al., 2021), Cu (Tian et al., 2021; Zhang et al., 2019), and so on. Recently, Wang *et al.*(H. Wang et al., 2020) reported a novel plasmonic Cu_7S_4-MoS_2-Au composite nanoparticle with broad absorption and high photothermal conversion efficiency, which arises from the coupling effect among Cu_7S_4, MoS_2 and Au, as well as the comprehensive utilization of their advantages. It is found that the visible absorption of Au (LSPR peak at ~520 nm) and

near-infrared absorption of Cu_7S_4 (LSPR peak at ~1500 nm) were successfully integrated with the LSPR absorption of nanoparticles. The synergy between these three nanoparticles successfully expands the absorption spectrum and enhances the absorption in the infrared region, which matches well with the solar irradiation spectrum. The entire gel material shows enhanced absorption capacity and low reflection, leading to excellent evaporation rate (3.824 kg m^{-2} h^{-1}) and energy conversion efficiency (96.6 %).

Carbon-based materials have been used as PTMs in various studies in recent years, owing to their excellent light absorption over a broad spectrum, ease of preparation, abundant and low cost. Carbon-based materials include activated carbon (Guo, Zhao, et al., 2019; Liang, Zhang, Huang, et al., 2020; Zeng et al., 2019; X. Zhou et al., 2020), polymer (Gong et al., 2019; Jianfei Liu et al., 2021; Z. Liu et al., 2021; Yanying Shi et al., 2021; Y. Xu et al., 2021) or biomass (Chen et al., 2020; Feng et al., 2021; Liu et al., 2018; Long et al., 2019; Lu et al., 2020; Tian et al., 2021) derived carbide, carbon black (Deng et al., 2019; He et al., 2021; Hu et al., 2020; N. Li et al., 2021; Jing Liu et al., 2021; H. Lu et al., 2021) and various amorphous carbon materials and highly graphitized carbon materials, such as graphene (Gao et al., 2021; Geng et al., 2020; Hou et al., 2020; Hu et al., 2019; Huo et al., 2019; Kong et al., 2020; Lei et al., 2021; D. Li et al., 2021; W. Li et al., 2020; Y. Li et al., 2021; C. Liu et al., 2020; C. Liu, Y. Peng, & X. Zhao, 2021; Y. Liu et al., 2020; Lou et al., 2021; X. Meng et al., 2020a, 2020b; Su et al., 2019; Tian et al., 2020; X.-Y. Wang et al., 2019; K. Yu et al., 2020; Zang et al., 2021; C.-R. Zhang et al., 2021; P. Zhang et al., 2018; Zhao et al., 2019; Zhou et al., 2018; Zhuang et al., 2020), carbon nanotubes (CNTs)

(Duan et al., 2021; Guan et al., 2020; Jian et al., 2021; Luo et al., 2021; S. Sun et al., 2021; Xu et al., 2019; X. Zhang et al., 2020; Y. Zhou et al., 2020; Liangliang Zhu, Tianpeng Ding, et al., 2019) and their derivatives.

As for amorphous carbon, the broad light absorption ability comes from the continuous energy levels emanating from the hybrid bonds (Zhao et al., 2011). To address the high reflective energy loss and thus improve their light-harvesting efficiency (F. Zhao et al., 2020), considerable efforts have been made in tailoring surface topography (Guo, Zhao, et al., 2019), constructing internal channels (Liang, Zhang, Huang, et al., 2020; X. Zhou et al., 2020), and introducing a second phase (Tan et al., 2019; X. Zhang et al., 2020). Among these amorphous carbons, activated carbon and carbon black are low cost, readily available materials, and can be easily mass-produced. It is reported that the carbon black can be treated by a concentrated HNO_3 solution to improve its hydrophilicity and the dispersibility in water (H. Lu et al., 2021). Considering the simple processing method and low cost of HNO_3, the carbon black can be arguably considered a low-cost material. Combing with a reasonable light path and design, the evaporation rate of these materials can reach 3.86 kg m^{-2} h^{-1}, and the energy conversion efficiency is as high as 92% (X. Zhou et al., 2020). Using biochar or polymer as the precursor can reduce fabrication costs (Chen et al., 2020) or make the derived carbide more design-oriented (Y. Guo, H. Lu, et al., 2020).

Different from amorphous carbon, the photothermal conversion effect of crystalline

carbon (graphene and highly graphitized carbon materials) arises from the conjugated π bonds. The large number of conjugated π bonds allow electrons to be excited at almost every wavelength of the solar spectrum, resulting in various π-π* transitions. The excited electrons relax through electron-phonon coupling, so energy is transferred from the excited electrons to the vibration mode of the entire atomic lattice, which causes the macroscopic temperature of the material to rise (Liangliang Zhu, Minmin Gao, et al., 2019). It is noted that a ISSG system containing reduced graphene oxide (rGO) generally exhibits a relatively high evaporation rate (2.33 - 2.72 kg m^{-2} h^{-1}) and higher energy conversion efficiency (> 90%) compared to the systems based on graphene and graphene oxide (GO) (Gao et al., 2021; Geng et al., 2020; Hou et al., 2020; Hu et al., 2019; Huo et al., 2019; Kong et al., 2020; Lei et al., 2021; W. Li et al., 2020; C. Liu et al., 2020; C. Liu, Y. Peng, & X. Zhao, 2021; Y. Liu et al., 2020; Lou et al., 2021; X. Meng et al., 2020a, 2020b; Su et al., 2019; Tian et al., 2020; X.-Y. Wang et al., 2019; K. Yu et al., 2020; P. Zhang et al., 2018; Zhao et al., 2019; Zhou et al., 2018; Zhuang et al., 2020). This result may be attributed to the residual functional groups (*i.e.* epoxy, hydroxyl) on the surface of rGO, which can be further investigated.

As the youngest carbon nanomaterials, carbon dots (CDs) (Singh et al., 2019; W. Zhang et al., 2021; Zhou et al., 2021) have attracted attention due to their broad light absorption spectrum (200-800 nm) and high photothermal conversion efficiency (> 90%), so that CDs can meet the requirements of PTMs (Indriyati et al., 2021). To further improve the performance of CDs for ISSG, future development directions include structure

adjustment and surface group modification without lowering crystallinity or wetting properties.

Apart from the aforementioned inorganic materials, unique, organic polymers with conjugated backbone structures are often used as a PTM in ISSG. Due to the π-conjugated backbones of sp^2-hybridized carbon, conjugated polymers have splitting energy levels and adjustable band-gaps, resulting in a similar performance to inorganic semiconductors (Xu et al., 2014; F. Zhao et al., 2020). Similarly, to improve the solar-thermal conversion performance, several strategies have been proposed to reduce the forbidden bandwidth and red-shift the main absorption peak to the near-IR region. For conjugated polymers, this is usually accomplished by oxidation doping (Xu et al., 2014). In addition, another advantage of polymer PTMs is that they have higher compatibility with hydrogel networks, thereby improving manufacturing processability.

A representative polymer PTM is polypyrrole (PPy), which has been reported in recent studies (S. Chen et al., 2021; Li et al., 2019; Loo et al., 2021; Ni et al., 2019; Park et al., 2021; Ye Shi et al., 2021; S. Sun et al., 2021; W. Wang et al., 2019; C. Wei et al., 2021; Y. Wu et al., 2021; Xiao et al., 2020; Xie et al., 2021; T. Xu et al., 2021; Zhao et al., 2018; Zhou, Zhao, et al., 2019b). For instance, Zhao *et al.* (Zhao et al., 2018) introduced PPy into a PVA-based hydrogel network and achieved a high evaporation rate of 3.2 kg m^{-2} h^{-1} with an excellent energy conversion efficiency of 94%. Recent research on conjugated polymer PTMs has been extended to polyaniline (Yin et al., 2018; Zhu et al., 2020),

poly(3,4-ethylene dioxythiophene) (C. Liu, Y. Peng, C. Cai, et al., 2021; Zhao & Liu, 2020), polydopamine (Y. Chen et al., 2021; Huang et al., 2021; Y. Sun et al., 2021; X. Xu et al., 2021; Y. Zou et al., 2021), perovskite hole layer material (Zhao et al., 2021), and covalent organic frameworks (Cui et al., 2021; C.-R. Zhang et al., 2021). Furthermore, conjugated copolymer materials such as poly(aniline-*co*-pyrrole) (Tan et al., 2019) have also shown up in recent research, proving a novel approach for ISSG by combining the advantages of two polymers.

2.2.2 Surface Topography Modification

The most effective strategy to enhance the light-harvesting capacity of the hydrogel platforms is to tailor surface topography to reduce light reflection (Guo, Zhao, et al., 2019; Y. Lu et al., 2021; Y. Sun et al., 2019; Z. Wei et al., 2021; F. Yang et al., 2021; Yin et al., 2018). Some materials (Y. Sun et al., 2019; Yin et al., 2018) are porous, so rough surfaces contribute to higher light-harvesting ability. Recently, researchers have proposed novel design methods to tailor undulating surfaces, including mold embossing (Y. Lu et al., 2021), *in-situ* template-assisted fabrication (Guo, Zhao, et al., 2019), and external

magnetic field-assisted methods (F. Yang et al., 2021).

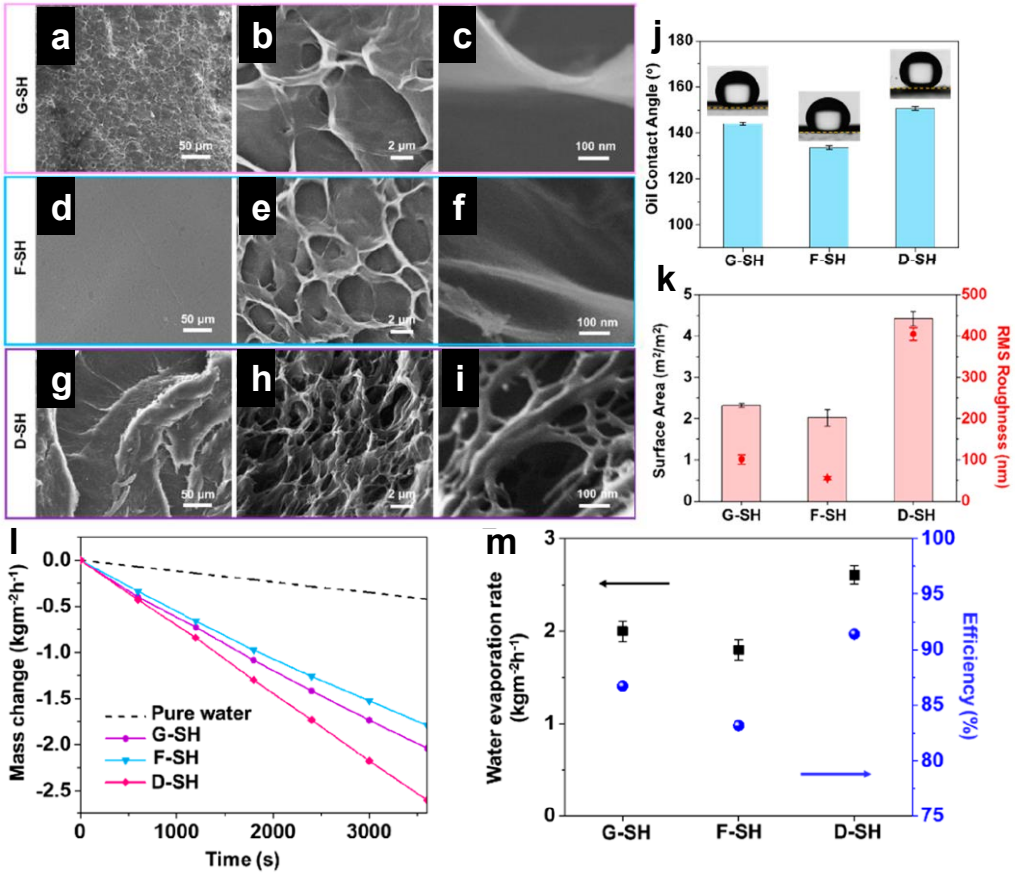

Figure 2.2 SEM images of different surface topography: (a−c) G-SH, (d−f) F-SH and (g−i) D-SH. (j) The underwater oil (1,2-dichloroethane) contact angle of each modified surface. (k) The optical profilometer test results revealed the surface area and root-mean-square (RMS) roughness of each sample. (l) The water mass changes, (m) water evaporation rates and energy conversion efficiencies of different samples under 1 sun. Reproduced with permission (Guo, Zhao, et al., 2019). Copyright 2019, American Chemical Society.

Mold embossing is an ordinary method to give the hydrogel corresponding patterns, but the cost of processing the mold is high and it is troublesome to make modifications to the mold. As a result, it is more suitable for subsequent confirmed mass production. Guo *et al.* first reported the *in-situ* template-assisted fabrication method (Guo, Zhao, et al., 2019). They used air, glass and a specific solvent (pentanol) as templates to produce grooved

surface hydrogel (G-SH), flat surface hydrogel (F-SH) and sharply dimpled surface hydrogel (D-SH), respectively. Commercially available AC paper was used as substrate and PTM, and a transparent PVA hydrogel layer was then prepared on the substrate to prepare a composite solar steam generator. As seen from the SEM images, G-SH has a rough surface with shallow holes (Figures 2.2a and 2.2b), but a higher magnification image (Figure 2.2c) reveals a relatively smooth sheet structure; F-SH tells a reasonably smooth outermost surface that is decorated with very shallow holes (Figure 2.2d) and shows a similar sheet-like structure at higher magnification (Figures 2.2e and 2.2f). For the D-SH sample, distinct "canyons" could be seen, resulting in a strongly dimpled surface topography (Figure 2.2g). The porous structures are strewn through canyon clusters (Figure 2.2h). Furthermore, D-SH has nanoscale pores nested in its microsized porous structure (Figure 2.2i), which neither G-SH nor F-SH has. D-SH has the highest RMS roughness with a surface area about 5 times that of its shadow area (Figure 2.2k). As a result, D-SH also shows super-hydrophobicity (Figure 2.2j), indicating that the super-wettability of PVA can be further tweaked by increasing surface roughness. Due to the roughest surface, the most significant evaporation interface and the highest hydrophilicity, D-SH displays the best ISSG performance (Figure 2.2l and 2.2m) with a water evaporation rate of 2.6 kg m^{-2} h^{-1} and an energy conversion efficiency of *ca.* 91%.

The other novel surface modified method is only effective for PTM particles with magnetism, such as the Ni@RF@SiO_2 core-shell nanoparticles in Yang et al.'s work (F. Yang et al., 2021). The nickel in the center of the core-shell structure is the source of

magnetism. The method primarily involves applying an external magnetic field to the magnetic PTM in order to adjust their distribution and convexity on the polymer surface, thus altering the surface morphology. Increasing the surface roughness of the hydrogel can simultaneously improve the light harvesting competence, and the effective evaporation surface area, which is beneficial to increase the production and energy conversion efficiency of the interfacial evaporator device. In contrast, the template-assisted surface construction method is more general, and suitable templates can be used for various polymers for further development, while the method based on an external magnetic field is only ideal for magnetic PTMs, which has certain limitations.

In addition, 3D printing is a promising technology to construct surface topography. Yuan *et. al.* (Yuan et al., 2021) firstly reported a 3D hierarchically porous cellulose/alginate/carbon black hydrogel via direct ink writing (DIW) 3D printing. Although the evaporation performance in this work is not impressive, it proves that 3D printing technique can be used to produce hydrogels with certain surface patterns for ISSG. DLP 3D printing is another advanced additive manufacturing technique that enables rapid fabrication of hydrogels via a layer-by-layer photopolymerization process, typically achieving more complex and intricate structures than DIW. Some studies (Alketbi et al., 2021; Chaule et al., 2021; Liu & Zheng, 2024; Wu et al., 2020; Yang et al., 2024; Zheng et al., 2023; M. Zou et al., 2021) have successfully utilized DLP for 3D printing hydrogels with complex surface structures for ISSG applications. However, existing formulations often require high precursor concentrations, resulting in dense

hydrogels that hinder water transport.

2.2.3 Reducing Heat Loss

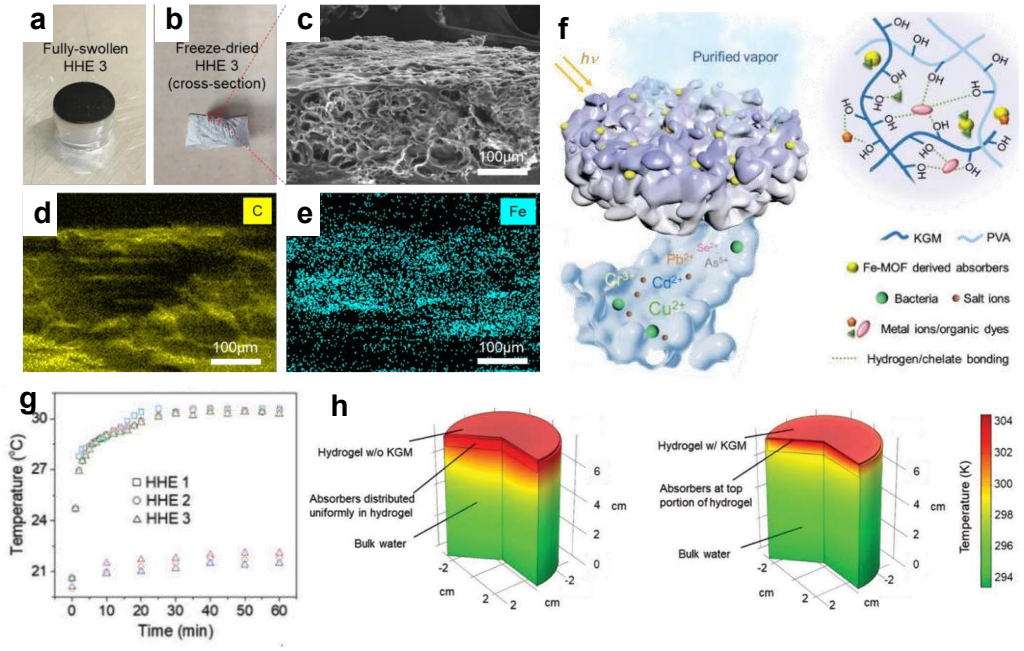

Figure 2.3 Spatial distribution of PTMs in HHE 3. Photographs of (a) fully swollen HHE 3; (b) cross-section of freeze-dried HHE 3; (c) SEM image of the top portion of HHE 3; the corresponding EDS mappings of (d) C and (e) iron elements. (f) Schematic illustration of solar water purification using HHEs. (g) Under 1 sun irradiation, the temperatures at both the hydrogel evaporator surface and in the bulk water. (h) COMSOL simulation results of the temperature distribution of a control sample (pure PVA hydrogel with uniformly distributed absorbers) and HHE 3. Reproduced with permission (Y. Guo, H. Lu, et al., 2020). Copyright 2020, John Wiley and Sons.

Aside from selecting the right PTM and tailoring surface topography, minimizing heat loss to the atmosphere and/or the bulk water is another effective way to boost solar-thermal conversion efficiency and overall water purification output. In principle, heat loss occurs in three ways (F. Yang et al., 2021), including the thermal radiation of the platform, convection between the platform and the ambient air, and heat conduction from the

surface to bulk water, which are all directly linked to the temperature of the platform or bulk water. Therefore, the surface or bulk water temperature is a critical reference value for measuring the heat loss of the platform. Current methods to reduce heat loss primarily rely on changing the distribution of PTMs (Y. Guo, H. Lu, et al., 2020; Guo, Zhao, et al., 2019; Hu et al., 2020; Li et al., 2019; Zeyu Sun et al., 2019; X.-Y. Wang et al., 2019; Xiao et al., 2020; X. Zhang et al., 2020), and incorporating heat-insulating materials.

As for the distribution of PTMs, uniform distribution of PTMs in the hydrogel matrix can reduce the heat flow inside the entire platform, thereby reducing heat loss compared to an unevenly dispersed system. For instance, the simply carboxylation treated CNTs can be uniformly distributed in the PAM matrix, improving energy conversion efficiency (X. Zhang et al., 2020). However, the even distribution of PTMs cannot mitigate heat dissipation to the surrounding environment. Therefore, researchers have designed multi-layered structures with all PTMs in a thin top layer to confine the energy around the evaporation interface (Guo, Zhao, et al., 2019; Hu et al., 2020; Li et al., 2019; Zeyu Sun et al., 2019; X.-Y. Wang et al., 2019; Xiao et al., 2020). On this basis, Guo et al.(Y. Guo, H. Lu, et al., 2020) have developed a ‘top-thin-layer’ with magnetic-driven PTMs to further reduce the interface contact heat loss between different layers. In this work, they use a magnet to carry the iron-based metal-organic framework (Fe-MOF) derived photothermal particles to one side of the PVA/konjac glucomannan (KGM, which also improves the heat insulation capacity) hydrogel to form a layered hybrid hydrogel evaporator (HHE, Figure 2.3f). HHE 3 with a KGM/PVA weight ratio of 0.16:10 shows

the highest evaporation rate (3.2 kg m^{-2} h^{-1}) at the highest energy conversion efficiency (90%). As seen from Figures 2.3a-2.3c, the black PTMs are located at the top of HHE 3, which is also confirmed by the EDS mapping (Figures 2.3d-2.3e). The surface temperature and bulk water temperature reach equilibrium temperatures of 31 and 22 ºC, as shown in Figure 2.3g. According to the COMSOL simulation results (Figure 2.3h), HHE 3 can keep heat close to the evaporation surface to reduce heat loss. This study thus proved its higher energy conversion efficiency compared with the evaporator with evenly distributed PTMs. In addition, there are some other methods to confine the PTMs on the surface layer, such as using the difference in surface tension between ethanol and water (Zhou et al., 2021), concentrating them on one end of the hydrogel under gravity (Tian et al., 2021), carbonized the upper side of the hydrogel (Z. Liu et al., 2021; B. Wen et al., 2021), and so on.

For heat management, in addition to using the PTMs as the heat-generating phase, the other phase in the platform usually exists as heat insulating substances. Hydrogels with high water content have inherent heat insulation ability. To further enhance the overall heat insulation, most studies add a heat insulation layer, such as polystyrene sulfonate (P. Zhang et al., 2018), polystyrene (Gong et al., 2019; Y. Wu et al., 2021), polyethylene (Y. Sun et al., 2019; D. Zhang et al., 2020), expanded polyethylene (Liu et al., 2018) foam and so on, at the bottom of the evaporation flatform. Yet, recent research incorporated heat confinement components such as specific aerogel spheres(Tan et al., 2019) and hydrophobic associations(X. Zhang et al., 2020) into the hydrogels to lift their overall

heat insulation performance. More recently, Wu *et al.*(X. Wu et al., 2021) reported a multi-layer spherical evaporator composed of a PS core and multi-layer outer coatings (PS-cellulose-PDA-PPy-PDA). This design reduces its density and restricts water transport only through the outer hydrophilic layers. Only a small part of the water can contact the water, thereby limiting the heat loss from the evaporation surface to the bulk water. In all, hydrophobic ingredients have been proven to be thermal confinement components to reduce heat loss.

2.3 Enhancing water transport/activation capacity

Water management, including water transport and water activation, is another critical process that determines the overall performance of solar water purification. Fast water transport speed can ensure continuous water supply to the evaporation interface. Adjusting the wettability and tuning the internal water transport channels are the two main design principles to enhance water transport. In addition, the capacity of the platform to promote water activation is essential to decrease the water vaporization enthalpy to improve the evaporation rate.

2.3.1 Adjusting the Wettability

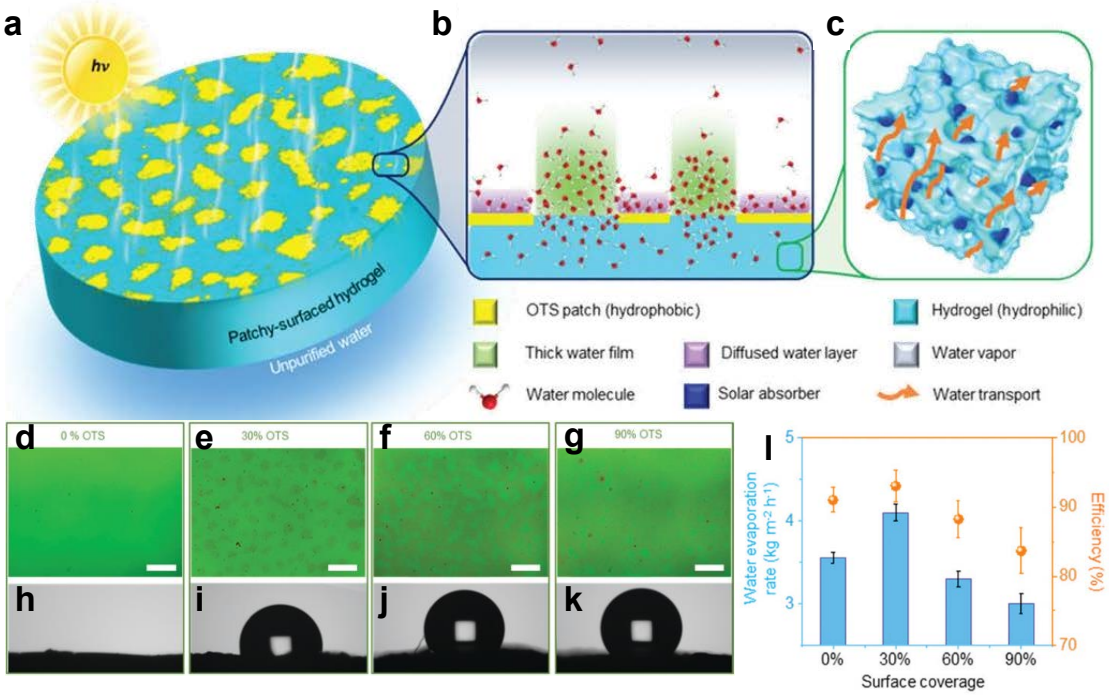

Figure 2.4 (a-c) Schematic illustration of patchy-surface hydrogels (PSHs). (d-k) Optical images and contact angles of PSHs with (d and h) 0%, (e and i) 30%, (f and j) 60%, and (g and k) 90% OTS covered surfaces. The scale bars are all 20 mm. (l) PSHs' evaporation rates and corresponding energy conversion efficiencies under 1 sun. Reproduced with permission (Y. Guo, X. Zhao, et al., 2020). Copyright 2020, Royal Society of Chemistry.

A practical method is to reduce the surface wettability to improve the water transport competence. Examples include using hydrophobic polydimethylsiloxane as the top layer (Jian et al., 2021), adding hydrophobic silicone aerogels mainly in the upper part (Tan et al., 2019; L. Zhao et al., 2020; Zhao et al., 2019), and reducing hydrophilic GO into hydrophobic rGO at the top side via laser (H. Zhang et al., 2021). Furthermore, Guo et al. (Y. Guo, X. Zhao, et al., 2020) have reported a patchy surface with hydrophobic and hydrophilic parts for higher water transport speed and excellent ISSG performance (4 kg m^{-2} h^{-1} with 93% energy conversion efficiency, Figure 2.4). The hydrogel has a partial

trichloro(octadecyl)silane (OTS) modified surface, with the island-shaped patches being hydrophobic and the rest being hydrophilic (Figure 2.4a). The thickness of the water film increased as a large portion of the water is confined in the hydrophilic region; thus, the effect of hydrogel surface on the outmost water molecules is decreased, resulting in faster evaporation (Figure 2.4b). The optical images and increasing water contact angles confirm the successful OTS modification of the surface of the hydrogels (Figures 2.4d-2.4k). Moreover, the introduction of hydrophobic components into the hydrogels can lead to the formation of internal gaps, thus ensuring rapid water replenishment (X. Zhang et al., 2020).

2.3.2 Tuning Internal Water Channels

The internal water channel is a vital channel for rapid water transport that can be constructed from three perspectives: size (C. Li et al., 2020; Liang, Zhang, Huang, et al., 2020; X. Meng et al., 2020b), direction (He et al., 2021; Irshad et al., 2021; Xu et al., 2019; F. Yu et al., 2020; Yu & Wu, 2020), and structure (Liang, Zhang, Liu, et al., 2020) to enhance the pumping force and/or capillary effect.

To tune the size of the water channel, Liang *et al.* have put forward a simple and fast construction method via fermentation. However, the evaporation rate is not high enough (1.611 kg m^{-2} h^{-1}) due to the large pores formed (900-2,540 μm) (Liang, Zhang, Huang, et al., 2020). Li *et al.*(C. Li et al., 2020) used the ice-template method to narrow the size of inner channel sizes to the submicrometer range, inducing a strong capillary force to

achieve rapid water transport over a long distance. The highest evaporation rate is 6.35 kg m^{-2} h^{-1} over a long transport distance of 8 cm. In addition to the uniform size channel, Meng *et al.* (X. Meng et al., 2020b) proposed an N-doped rGO aerogel with ring-like gradient vertically aligned microchannels. It is found that the spacing and wall thickness increase from the center to the edge, and the specific channel sizes distribution is realized by introducing a concentration gradient of NH_4OH (as antifreeze) before freeze-drying. The gradient channel size distribution can ensure concentrated pumping in the center, leading to a high evaporation rate of 2.53 kg m^{-2} h^{-1}.

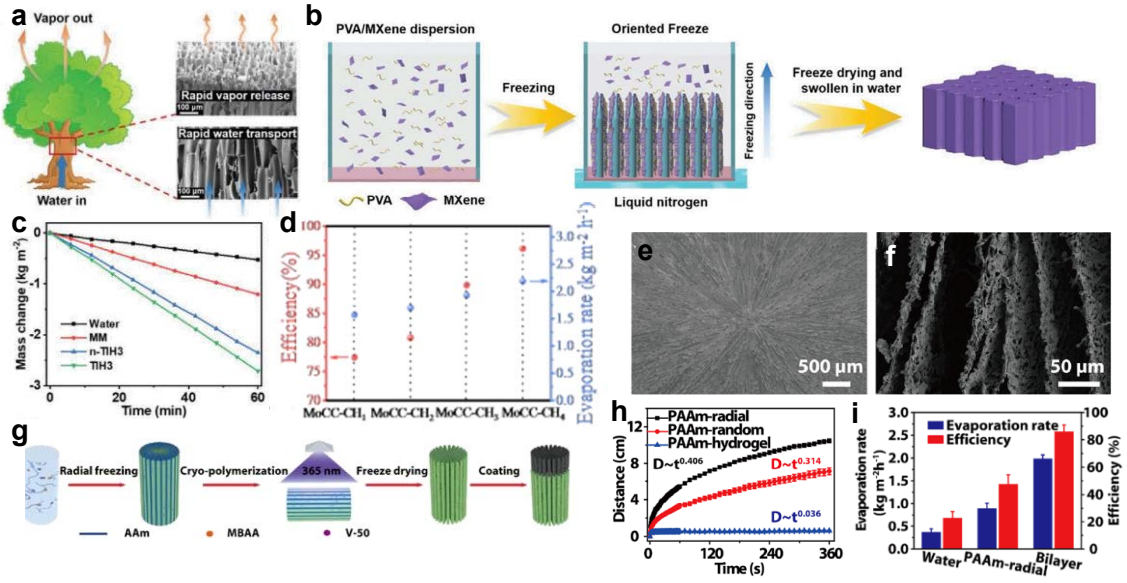

Figure 2.5 (a) Schematic illustration of the water transport in tree from root to the top with the SEM images of the top and bottom of wood. (b) Schematic illustration of the direction freezing method. (c) Water mass loss for pure water, MM, n-TIH3, and TIH3 under 1 sun. Reproduced with permission (Yu & Wu, 2020). Copyright 2020, John Wiley and Sons. (d) Evaporation rates and energy conversion efficiencies of MoCC-CHs. Reproduced with permission (F. Yu et al., 2020). Copyright 2020, American Chemical Society. (e-f) SEM images of radially aligned channels and micropores. (g) Schematic illustration of the radial freezing method. (h) Water transport distance over time. (i) Water evaporation rate and energy conversion efficiency of PAAm-based aerogels with different channel directions. Reproduced with permission (Xu et al.,

2019). Copyright 2019, American Chemical Society.

Inspired by the water transport in the trees in nature, vertically aligned internal channels have the potential to quickly transport water from the bottom of the evaporation generator to the top and release vapor quickly (Figure 2.5a). The direction freezing method (He et al., 2021; Yu & Wu, 2020) is usually used to construct vertically aligned channels. For example, Yu *et al.* (Yu & Wu, 2020) prepared a PVA/MXene hydrogel with wood-like vertically aligned channels using the above method (Figure 2.5b). The hydrogel with vertically aligned channels (TIH3) represents higher water mass change than that of bulk water, MXene membrane and non-tree-inspired hydrogel (n-TIH3) (Figure 2.5c). As a result, the TIH3 shows a high evaporation rate of 2.71 kg m^{-2} h^{-1} as a vapor generator in ISSG. Besides, the tortuosity of the internal channels can be adjusted by introducing chitosan (CTS) content in the hydrogels (Irshad et al., 2021; F. Yu et al., 2020). With a higher content of CTS, lower-tortuosity channels can be achieved to speed the water transport as well as lift the evaporation rate (Figure 2.5d). Xu *et al.* have proposed a radial ice-template method (Figure 2.5g) to achieve the radial vertically-aligned channels, which are more similar to the internal channels of a tree (Figure 2.5e) (Xu et al., 2019). The aerogel with radial vertically-aligned channels shows stronger water transport capacity over a longer distance than others (Figure 2.5h), but it displays a medium ISSG performance with an evaporation rate of 2 kg m^{-2} h^{-1} at 85.7 % energy conversion efficiency (Figure 2.5i). This is relatively lower than the hydrogels with vertically aligned channels.

Gradient capillarity has been proved to facilitate strong direction-limited water transport in hydrogels. Liang *et al.* (Liang, Zhang, Liu, et al., 2020) developed an effective fabrication method based on the G-T template to fabricate gradient structure hydrogels, in which G represents glass while T represents polytetrafluoroethylene. It is found that between the top and bottom of the gradient-structured hydrogel, the sizes of the channel is changing continuously. The improved capillary pumping through the channels from the bottom in water to the surface in air results in rapid, one-way water replenishment, allowing for a high evaporation rate (1.684 kg m^{-2} h^{-1}) and less heat loss.

2.4 Water Activation

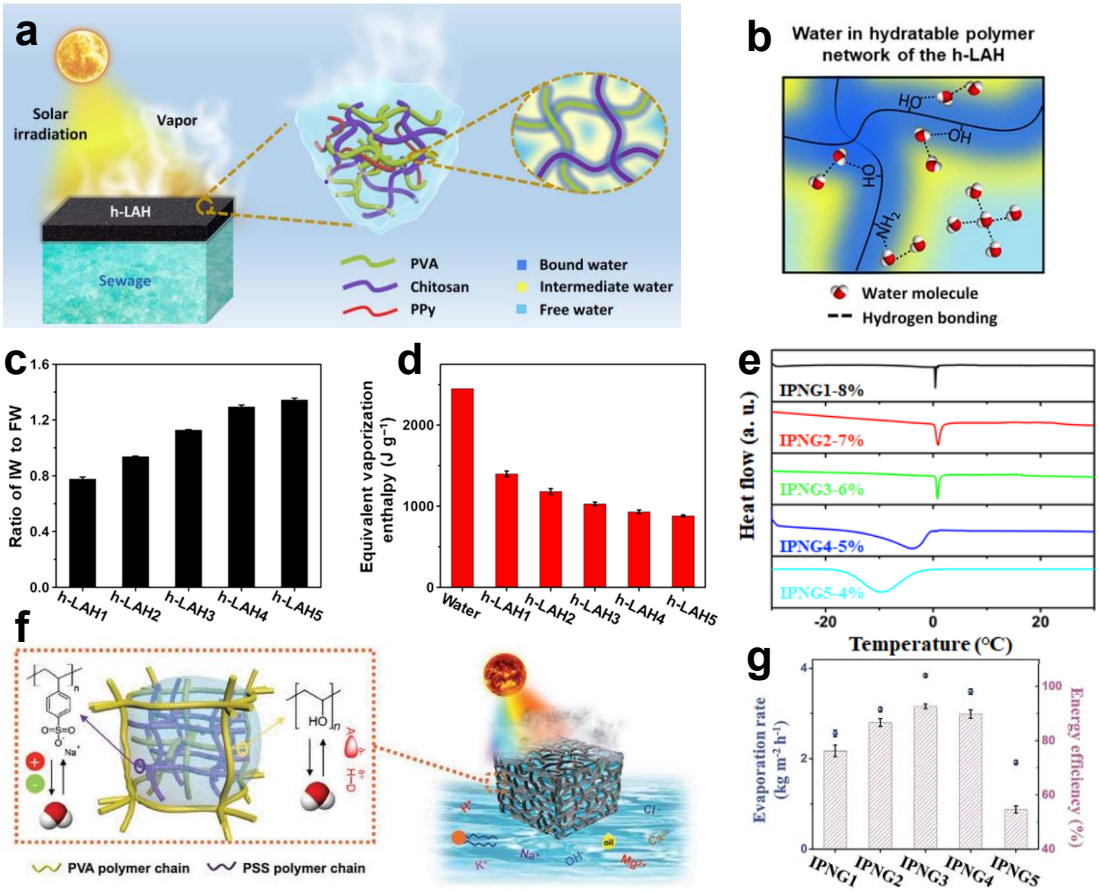

Figure 2.6 (a) Schematic illustration of ISSG based on h-LAH. (b) Water state in h-LAH. (c) In

h-LAHs, the IW/FW ratio. (d) Bulk water and the water in h-LAHs' equivalent water vaporization enthalpy. Reproduced with permission (Zhou, Zhao, et al., 2019b). Copyright 2019, American Association for the Advancement of Science. (e) The melting activity of IW in various frozen IPNGs as depicted by DSC curves. (f) Solar water purification with conrrolled hydration based on IPNG. (g) IPNGs' solar evaporation rate and energy conversion efficiency under 1 sun. Reproduced with permission (X. Zhou et al., 2020). Copyright 2020, John Wiley and Sons.

Specific water states in polymer hydrogels can make the water more active, thereby facilitating the evaporation process. Here, "water activation" refers to the state in which water molecules are less tightly bound and thus require less energy to evaporate, typically exhibiting increased molecular mobility and reduced evaporation enthalpy. Three forms of water have been identified in the hydrated polymer network, including bond water (BW, dark blue color area in Figures 2.6a-2.6b) with water-polymer bonding, free water (FW, light blue color area) with water-water bonding, and IW (yellow color area) with weakened water-polymer and water-water bonding between BW and FW. IW is the key water state which requires less energy to escape from the adjacent molecules as a form of clusters to decrease the water evaporation enthalpy, increasing the evaporation rate. Therefore, in order to reduce the energy demand for water evaporation from the hydrogel, it is desirable to tune the building blocks to achieve a higher amount of IW within hydrogels. In this field, techniques such as differential scanning calorimetry (DSC) and Raman spectroscopy are commonly employed to distinguish and quantify these water states. These methods are also applied in subsequent chapters to investigate how hydrogel structure influences water state distribution.

Considerable efforts have been devoted to tuning the IW content in hydrogel networks,

including the adjustment of polymer concentration, the introduction of hydrophilic functional groups (−OH, −COOH, $-SO_3H$, $-NH_2$ and −CONH−, to form noncovalent interaction), the change of cross-linking density, and the construction of porous structures (Guo & Yu, 2021). For example, Zhou *et al.* (Zhou, Zhao, et al., 2019b) tuned the PVA/CTS ratios from 1:0 to 1:0.25 to form hydrogels, namely h-LAH1-5. Their IW/FW ratios increased, and the equivalent vaporization enthalpy decreased correspondingly, as shown in Figures 2.6c-2.6d. However, the evaporation enthalpy is not the only factor that can influence the water evaporation performance. h-LAH5, which has the lowest vaporization enthalpy, still has a high water content, which hinders effective energy utilization and restricts evaporation rate. After balancing these two factors, h-LAH4 with a relatively higher water vaporization enthalpy and relatively lower water content shows the highest evaporation rate of 3.6 kg m^{-2} h^{-1} and the best energy conversion efficiency of 92%.

In addition, ionic polymers have electrostatic interaction with water molecules, stronger than hydrogen bonding between polymer chains and water molecules. Zhou *et al.*(X. Zhou et al., 2020) incorporated polystyrene sulfonate (PSS), which can be hydrated with water via electrostatic interaction and hydrogen bonding, into the PVA networks to form a semi-interpenetrating polymer networks gel (IPNG, Figure 2.6f). IPNG1-5 have different PSS/PVA ratios of 0:1, 1:1, 1.5:1, 2:1 and 1:0, and their IW/FW ratios can be calculated from the differential scanning calorimetry (DSC) curves (Figure 2.6e). It is found that with the increase of PSS content, the ratio of IW/FW increases in response,

mainly due to the increase of IW. However, when the IW content reaches the maximum limit, the ratio will drop simply because FW content will continue to increase. As a result, IPNG3 with a PSS/PVA ratio of 1.5:1 shows the highest IW/FW ratio and the highest evaporation rate (3.86 kg m^{-2} h^{-1}) with an energy conversion efficiency of 92% (Figure 2.6g).

In addition to the aforementioned methods, some recent researches also use polyelectrolyte-based hydrogels as well as some other strategies to implement strong ionic pumping (Zeng et al., 2019), construct an overall water management system (Y. Li et al., 2021; Y. Sun et al., 2021; C. Wen et al., 2021) and stimulate water transport and evaporation.

2.5 Conclusions and Remaining Challenges

In conclusion, recent progress in interfacial solar steam generation proves that a higher evaporation rate as well as energy efficiency can be achieved by designing the entire system from two key aspects of heat and water management. As for the heat management, tailoring surface topography to enhance light harvesting, selecting adequate photothermal materials with stronger full solar spectrum absorption (especially the infrared band) and higher photothermal conversion ability, and minimizing heat loss to the atmosphere and bulk water through managing the distribution of photothermal materials and heat insulation components, proved to be effective strategies for harvesting sunlight. Concerning water management, adjusting wettability to ensure rapid water replenishment,

tuning the size, direction and structure of the internal channel to enhance the channel pumping, and increasing the IW content in hydrogels to lower the water vaporization enthalpy are the three main approaches that have been successfully implemented.

From the perspective of material development, while significant advancements have been made in photothermal materials, with many achieving nearly 100% photothermal conversion efficiency, evaporation rates remain relatively low, constraining the potential for higher freshwater productivity. This limitation arises from the underexplored role of polymeric hydrogels, the core component of ISSG systems. Even with ideal photothermal conversion, the ISSG evaporation rate is fundamentally capped at the theoretical maximum of 1.59 kg m^{-2} h^{-1}, as dictated by Equation 1, without leveraging the unique interactions between polymeric hydrogels and water. To overcome this barrier and further enhance evaporation rates, research focus must shift toward optimizing water management within polymeric hydrogels.

What's more, to pave the way for the future practical application of hydrogel-based ISSG, several critical challenges must be addressed. First, current research predominantly focuses on small-scale hydrogels prepared using molds for laboratory experiments. While these hydrogels can achieve high evaporation rates, their limited size fails to generate sufficient vapor for practical applications. Scaling up hydrogel fabrication poses challenges, such as restricted flexibility in mold shapes and property inconsistencies within larger hydrogels. Thus, industrial-scale manufacturing techniques like 3D printing

should be thoroughly investigated to produce hydrogels tailored for ISSG. Second, despite achieving high evaporation rates, the low condensation efficiency of ISSG systems remains a significant constraint, limiting freshwater productivity. Lastly, long-term operation introduces additional issues, including salt deposition and contamination from pollutants. Addressing these challenges requires strategic advancements in materials, structural designs, and system configurations to reduce salt buildup and mitigate contamination, ensuring sustainable and efficient ISSG performance.

CHAPTER 3
Chemicals and Characterizations

3.1 Introduction

This chapter provides an overview of all the chemicals utilized throughout this thesis and outlines the characterization techniques employed. Detailed experimental procedures specific to each study are provided in the relevant chapters.

3.2 Chemicals

All the chemicals in this thesis's experiments, involving 2-acrylamido-2-methyl-1-propanesulfonic acid (AMPSA), acrylic acid (AA, 99 wt% in DI water), 2-hydroxyethyl acrylate (HEA, 96 wt% in DI water), poly(ethylene glycol) diacrylate (PEGDA, average M_n = 575 g mol^{-1}), N,N-dimethylacrylamide (DMA, 99 wt% in DI water), acrylamide (AM), [2-(acryloyloxy)ethyl]trimethylammonium chloride (AETAC, 80 wt% in DI water), PVA (MW 89000-98000), graphene oxide (GO, powder, 15-20 nanosheets, 4-10% edge-oxidized), *N,N'*-methylenebis(acrylamide) (MBA), ammonium persulfate (APS), L-Ascorbic acid (Vitamin C, VC), *N,N,N',N'*-tetramethyl-ethylenediamine (TEMED), glutaraldehyde (GA) solution (25 wt% in DI water), hydrochloric acid (HCl, 32 wt% in DI water), lithium phenyl-2,4,6-trimethylbenzoylphosphinate (LAP), sodium chloride (NaCl), and methyl blue (MB) were purchased from Sigma-Aldrich Australia and used directly without any further purification.

3.3 Characterizations

3.3.1 Zeta Potential

The corresponding polymer samples were prepared by omitting the cross-linker in the hydrogel synthesis procedure. Malvern 2000 particle size analyzer (Malvern, United Kingdom) was used to confirm the zeta potential of the polymers.

3.3.2 Scanning Electron Microscope (SEM)

With the help of a Zeiss scanning electron microscope (SEM) (10–30 kV), the hydrogels' pore structure was explored.

3.3.3 Fourier Transform Infrared Spectroscopy (FT-IR)

By using a Shimadzu MIRacle 10 FT-IR, Fourier transform infrared spectroscopy (FT-IR) results were obtained.

3.3.4 UV-visible-NIR (UV-vis-NIR)

The hydrogel films for testing were drop-casting and crosslinking on the glass slides directly. Using a Shimadzu 1700 UV-visible-NIR spectrophotometer operating in the wavelength range of 300-2500 nm, UV-vis-NIR absorbance spectra were gathered.

3.3.5 Raman Spectra

A Renishaw Raman spectroscopy was used to acquire the Raman spectra, and the hydrogel samples were fully saturated before tests.

3.3.6 Differential Scanning Calorimetry-Thermogravimetric Analysis (DSC-TGA)

All the hydrogel samples were fully saturated before tests. A Q600 SDT Thermal Analyser (DSC-TGA) was used to track the heat change of hydrogels from room temperature to 200 °C at a heating rate of 10 °C min^{-1}.

3.3.7 DSC

All the hydrogel samples were fully saturated before tests. Thermal changes in the hydrogels, from room temperature to 200 °C, were monitored with a NETZSCH DSC300 Supreme at a heating rate of 5 °C min^{-1}.

3.3.8 Viscosity Test

The viscosity of the 3d printing ink was confirmed by a Brookfield DV2T viscometer at a constant temperature of 25 ºC using a spindle SC4-29. The spindle speed was controlled at 120 rpm.

3.3.9 Tensile Test

The tensile test of the printed hydrogel was conducted by Shimadzu AGS-X Universal Tester (Max load 10 kN) with a strain rate of 50 mm min^{-1}. The dimensions of the tested samples specimens were length = 100 mm, width = 6 mm, and thickness = 5 mm according to ASTM (E8) subsize standard.

3.3.10 Contact Angle

The contact angle test was conducted by an Attension contact angle meter.

3.3.11 Inductively Coupled Plasma Mass Spectrometry (ICP-MS)

An Agilent 7900 ICP-MS was employed to analyze the concentrations of the four primary ions in both seawater and desalinated water.

3.3.12 UV-Vis Spectroscopy

An Agilent Cary 60 UV-Vis Spectroscopy was used to detect the MB in water before and after SSG purification.

3.3.13 Total Dissolved Solids (TDS)

A portable multimeter called the HQ40D was used to measure the total dissolved solids (TDS) in both seawater and desalinated water.

CHAPTER 4
Nanoscale: Interaction Between Water Molecules and Hydrophilic Groups

This chapter has been derived from the published paper of **Mao, S.**, Feng, A., Zhang, S., Onggowarsito, C., Chen, Q., Su, D., & Fu, Q. (2023). Investigation of structure-property-application relationships of the hydrogel-based solar vapor generator. *Journal of Materials Chemistry A*, 11(42), 23062-23070.

Following the general introduction and methodology overview, the research begins by examining polymer–water interactions at the molecular level. Understanding how hydrophilic groups within polymer chains influence the state and dynamics of water is fundamental to optimizing hydrogel-based solar steam generation. This chapter investigates these interactions by analyzing water state, evaporation enthalpy, and replenishment behavior in hydrogels with varied chemical compositions, providing nanoscale insights into water release mechanisms.

4.1 Introduction

Water is one of the most abundant resources on earth, covering three quarters of the earth's surface. However more than 97% of the earth's water is salt water in the oceans that cannot be used directly (Kalogirou, 2005). In recent decades, the demand for freshwater has been increasing due to factors such as rapid population expansion, climate change, and economic development, and has become increasingly mismatched with freshwater supply (Chakkaravarthy, 2019; Immerzeel et al., 2010). To alleviate the growing water scarcity, it is imperative to develop cost-effective, complementary technologies for desalination to extract more freshwater from the plentiful saline water resources while reducing energy consumption and environmental footprint (AlMarzooqi et al., 2014; Khawaji et al., 2008; Panagopoulos et al., 2019; Semiat, 2008; Shannon et al., 2008). Hydrogel based ISSG is an emerging portable desalination technology that uses the heat converted from solar energy to evaporate absorbed water for freshwater acquisition. It has aroused considerable

interest owing to its zero additional energy input, high solar-thermal conversation efficiency and excellent freshwater productivity (Deng et al., 2017; Ma et al., 2017; Neumann et al., 2013; Xu et al., 2020; Zhu et al., 2021).

Compared with other raw materials, such as natural materials (Xie et al., 2021), carbon-based materials (Gong et al., 2019; Liu et al., 2018; P. Zhang et al., 2018), coordination networks (W. Li et al., 2020; Su et al., 2019) used to manufacture ISSGs, polymeric hydrogels have the advantages of a straightforward fabrication process, a customizable chemical structure, low manufacturing costs and compatibility with a variety of PTMs (Ibrahim et al., 2021; Y. Wang et al., 2021; Yang et al., 2020). Most crucially, polymer hydrogel-based ISSGs are able to evaporate water at a rate greater than the theoretical limit of 1.59 kg m^{-2} h^{-1} under one solar irradiation (1 kW m^{-2}) (Chen et al., 2022; T. Li et al., 2021). The water molecules can be divided into three categories based on how they interact with polymer chains: FW, IW, and BW (Guo, Zhou, et al., 2019; Zhou, Zhao, et al., 2019a). FW with solely water-water bonding has no interaction with the polymer chains, while BW with direct hydrogen bonding has the strongest interaction with polymer chains. IW is the water between BW and FW which has weakened water-water bonding, making it easier to escape from the adjacent molecules. In light of this, the IW aroused by the hydrophilic groups in the polymeric hydrogels can reduce the equivalent water vaporization enthalpy, which is the key to their high evaporation rates beyond the theoretical maximum. It's interesting to note that, in addition to polymer chains with hydrophilic groups, the recent advance in metallic λ-Ti_3O_5 by Bo Yang *et al.*(Yang et al.,

2023), also revealed that the excited water molecules (*i.e.* H_3O^*) can be generated at the evaporation interface to form water clusters, which in turn facilitates the evaporation of water.

Polymeric hydrogels can be made from monomers with various hydrophilic groups, such as hydroxyl group (-OH), carboxy group (-COOH), amino group (-NH_2), ester group (-C-O-C-), sulfonyl hydroxide group (-SO_3H) and others. For instance, PVA hydrogels containing numerous -OH groups initially proposed by Yu's group (Zhao et al., 2018; Zhou et al., 2018), are most often employed as ISSGs due to their excellent chemical stability and low cost (Mao et al., 2022; Onggowarsito et al., 2022; F. Zhao et al., 2020; Zhao et al., 2021; Zhou, Guo, et al., 2019). While, a considerable number of studies have reported ISSGs based on other hydrophilic polymer networks, such as -SO_3H groups in polystyrene sulfonates (X. Zhou et al., 2020), –NH_2 groups in polyacrylamides (Yang et al., 2022; Y. Zhou et al., 2020), -C-O-C- groups in polyethylene glycols (C. Liu, Y. Peng, & X. Zhao, 2021; Zheng et al., 2023). Unfortunately, these studies have overlooked the structure-property-application relationship of hydrogel-based ISSG systems. We saw this is an opportunity to investigate the overall performance of ISSGs from a materials chemistry perspective, and hope that this research will fill the knowledge gap and further provide more guidance for the development of next generation ISSG.

Here, we prepared a series of polymer hydrogels with various functional groups by free radical cross-linking, systematically investigated the interactions between water

molecules and different hydrophilic groups in the hydrogels, and compared their overall ISSG performance. Specifically, monomers used included AMPSA with -SO_3H group, AA with -COOH group, HEA with -OH group, PEGDA with -C-O-C- group, DMA with dimethylamino groups (-$N(CH_3)_2$), AM with -NH_2 group, and AETAC with quaternary ammonium groups (-$N^+(CH_3)_3Cl^-$). The corresponding hydrogels were then fabricated by free radical cross-linking induced by APS with the addition of a trace amount of graphene oxide as PTM. Due to the different preference of hydrophilic groups for water molecules, the highly charged polymer chains with -SO_3H or -$N^+(CH_3)_3Cl^-$ group have stronger interactions with water molecules and therefore show the lowest solar evaporation performance. While, the solar evaporation performance of neutral polymer chain hydrogels were -NH_2 > -$N(CH_3)_2$ > -C-O-C- > -OH > -COOH in descending order due to the gradual decrease in the IW content and the increase in the hydrogen bonding energy and equivalent water evaporation enthalpy.

4.2 Experimental Section

4.2.1 Chemicals

Chemicals involving AMPSA, AA (99 wt% in DI water), HEA (96 wt% in DI water), PEGDA (average M_n = 575 g mol^{-1}), DMA (99 wt% in DI water), AM, AETAC (80 wt% in DI water), GO (powder, 15-20 nanosheets, 4-10% edge-oxidized), MBA, APS, VC, TEMED, were all utilized without any further purification after being acquired from Sigma-Aldrich Australia.

4.2.2 Synthesis of Hydrogels in Acid Condition

As the mixture of acidic monomer (AMPSA or AA), cross-linker and GO solution is in an acid condition, VC served as the catalyst. Typically, 277.11 mg of AMPSA was mixed with 22.89 mg of MBA, 36 mg of VC and 1.9 mL of GO solution (1.5 mg mL^{-1} in DI water) by sociation. Following that, to start the gelation, 0.1 mL of APS solution (0.3 g mL^{-1} in DI water) was added and stirred. The synthesised gel was triple-washed with DI water after being frozen overnight at -18 ℃ and thawed in DI water at room temperature to obtain a pure PAMPSA-GO hydrogel. Similar steps were followed for generating PAA-GO hydrogel, with the exception of the amounts of AA (242.43 mg, 99 wt% in DI water) and MBA (57.57 mg). Before being characterised, all of the hydrogels were freeze-dried. And prior to the ISSG tests, they were all well-saturated in DI water or seawater.

4.2.3 Synthetic Procedure for Other Hydrogels

For the other neutral or alkaline monomers, TEMED worked as the catalyst. Typically, 261.48 mg of HEA was mixed with 38.49 mg of MBA, 10 μL of TEMED and 1.9 mL of GO solution (1.5 mg mL^{-1} in DI water) by sociation. Following that, to start the gelation, 0.1 mL of APS solution (0.3 g mL^{-1} in DI water) was added and stirred. The synthesised gel was triple-washed with DI water after being frozen overnight at -18 ℃ and thawed in DI water at room temperature to obtain a pure PHEA-GO hydrogel. Similar steps were followed for generating PPEG-GO, PDMA-GO, PAM-GO, PAETAC-GO hydrogels, with the exception of the amounts of monomers and MBA (listed in Table 4.1). Before being

characterised, all of the hydrogels were freeze-dried. And prior to the ISSG tests, they were all well-saturated in DI water or seawater.

Table 4.1 The mass of the monomer and crosslinker used for the synthesis of the corresponding hydrogel.

Sample name	Mass of the monomer (mg)	Mass of the cross-linker (mg)
PAMPSA-GO hydrogel	277.11	22.89
PAA-GO hydrogel	242.43	57.57
PHEA-GO hydrogel	261.48	38.49
PPEG-GO hydrogel	300.00	0.00
PDMA-GO hydrogel	258.36	44.22
PAM-GO hydrogel	241.80	58.20
PAETAC-GO hydrogel	344.40	24.49

4.2.4 Characterizations

Malvern 2000 particle size analyzer (Malvern, United Kingdom) was used to confirm the zeta potential of the polymers. With the help of a Zeiss scanning electron microscope (SEM) (10–30 kV), the hydrogels' pore structure was explored. By using a Shimadzu MIRacle 10 FT-IR, FT-IR results were obtained. Using a Shimadzu 1700 UV-visible-NIR spectrophotometer operating in the wavelength range of 300-2500 nm, UV-vis-NIR absorbance spectra were gathered. A Renishaw Raman spectroscopy was used to acquire the Raman spectra. A Q600 SDT Thermal Analyser (DSC-TGA) was used to track the

heat change of hydrogels from room temperature to 200 °C at a heating rate of 10 °C min^{-1}. Using an Agilent 7900 ICP-MS, the principal four ion concentrations in seawater and desalinated water were examined. A portable multimeter called the HQ40D was used to measure the total dissolved solids in both seawater and desalinated water.

4.2.5 Simulation Study

The simulation study was conducted based on Merck Molecular Force Field 94 (mmff94) using *Avogadro* software.

4.2.6 Interfacial Solar Steam Generation Tests

To simulate the sun irradiation, a solar simulator (NBeT HSX-F3000 xenon light source) was utilized. The solar irradiance on the gel surface was calibrate to one sun (1 kW m^{-2}) by a portable power and energy metre console with a thermal power sensor (PM100D and S405C, Thorlabs, Germany). The testing hydrogel was fixed in the middle of a floating expanded polyethylene (EPE) foam on the top of a beaker full of DI water or seawater. To avoid the potential effects of bulk water evaporation, a parafilm was employed to fill a few small areas between the EPE foam and the beaker. During the ISSG testing, the water mass losses over time were recorded by an electronic mass balance (OHAUS Pioneer IC-PX 124). In order to insulate the heat transferred between the mass balance and the beaker, another EPE foam was also placed between them. The slopes of the mass loss-time curve were calculated using linear fitting to determine the evaporation rates.

During the ISSG tests, the temperatures of the hydrogel surface and the bulk water were measured every five minutes using a Fluke PTi120 pocket thermal imager.

4.3 Results and Discussion

4.3.1 Hydrogels' Chemical Structure and Morphology

In this work, seven hydrogels with 15 wt% of polymer contents (the molar ratio of [monomer]:[crosslinker] = 9:1) and 1 wt% of photothermal materials were fabricated through the same free radical cross-linking and freeze-thawing process for fair comparison (Figure 4.1a).

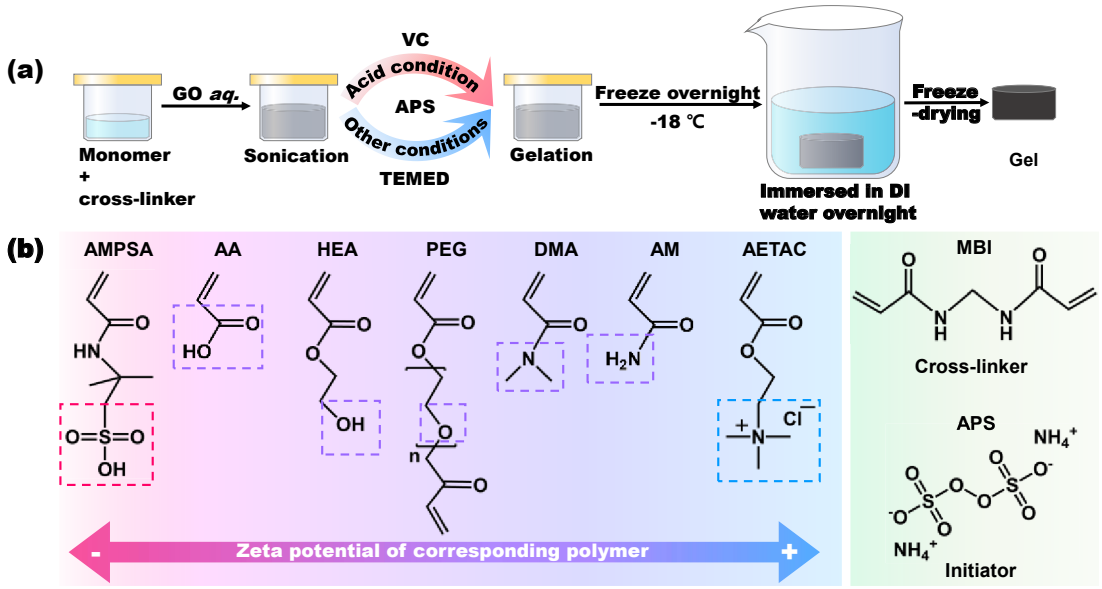

Figure 4.1 (a) Schematic illustration of the preparation of the hydrogel ISSGs. (b) Chemical structures of the monomers, cross-linker and initiator.

Specifically, seven monomers with various hydrophilic groups were dissolved in DI water in seven different vials, including AMPSA with -SO_3H groups, AA with -COOH groups,

HEA with -OH groups, PEG with -C-O-C- groups, DMA with -$N(CH_3)_2$ groups, AM with -NH_2 groups, and AETAC with -$N^+(CH_3)_3Cl^-$ groups (Figure 4.1b). MBA was added into seven vials as the cross-linker, except for the PEGDA vail, which could cross-link with itself. These vials were subsequently infused with the same amount of GO dispersion (PTM), followed by 5 minutes of sonication. Thereafter, APS (initiator) together with apposite catalyst were added to trigger the gelation process. After 5 minutes of gelation at a steady state, the obtained hydrogels were frozen at -20 ºC and thawed in DI water to facilitate the internal pores formation. These hydrogels were freeze-dried before characterization and water evaporation tests. The fabricated gels were denoted as polymer-GO.

We also prepared seven polymers by omitting the cross-linker and tested the zeta potential of the corresponding polymers. The average value from three times of zeta potential testing for PAMPSA, PAA, PHEA, PPEG, PDMA, PAM, and PAETAC polymers was -82.6, -11.3, -1.9, -1.8, 0.6, 3.3 and 68.4 mV, respectively. The high charge of PAMPSA and PAETAC were attributed to the -SO_3H or -$N^+(CH_3)_3Cl^-$ groups, respectively. While the charges of other polymers were close to zero with a slightly gradual increasing trend.

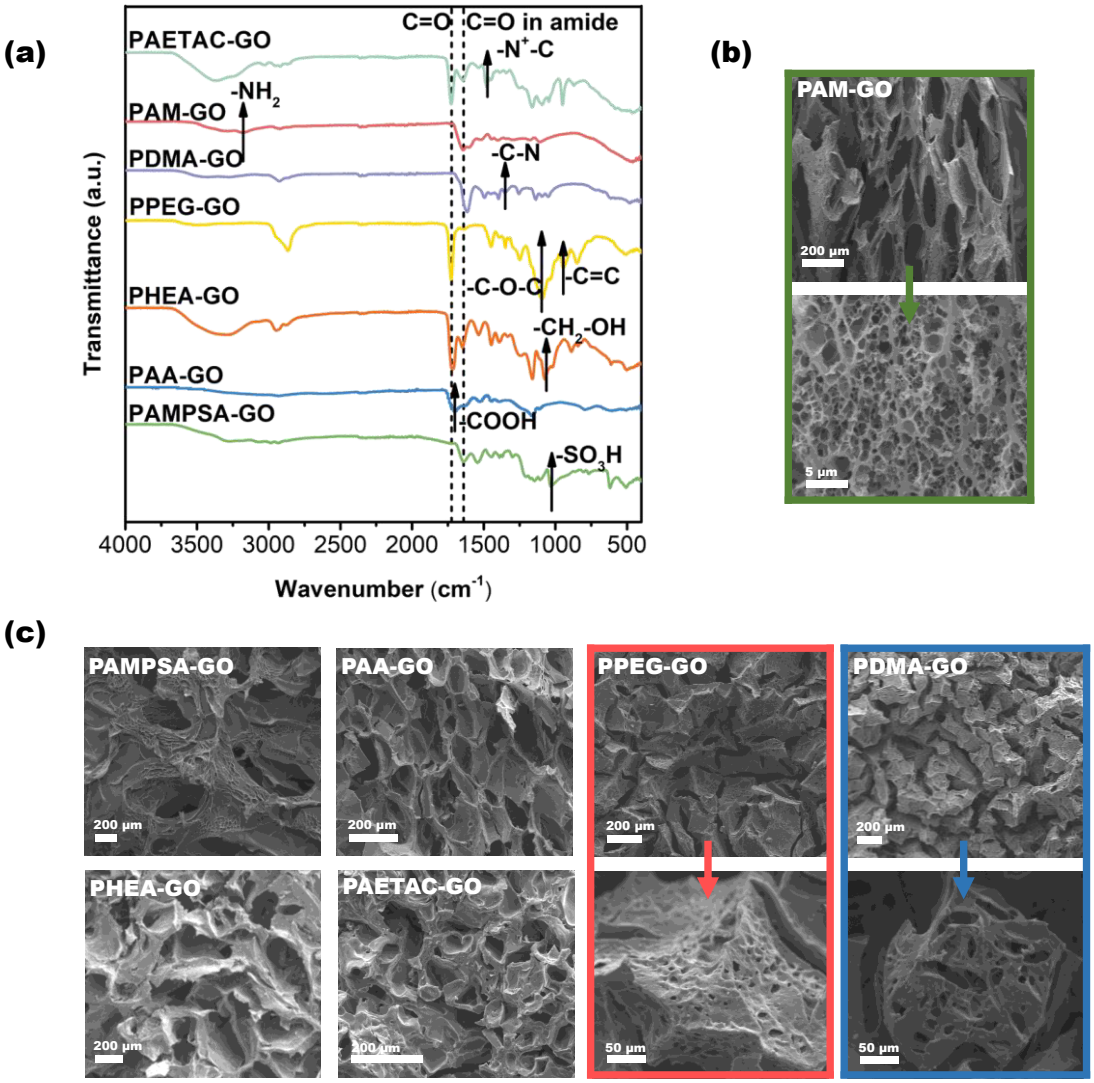

Figure 4.2 (a) FT-IR spectra of PAMPSA-GO, PAA-GO, PHEA-GO, PPEG-GO, PDMA-GO, PAM-GO and PAETAC-GO. Cross-section SEM figures of the fabricated hydrogels: (b) PAM-GO, (c) PAMPSA-GO, PAA-GO, PHEA-GO, PPEG-GO, PDMA-GO, and PAETAC-GO. Among them, PPEG-GO, PDMA-GO and PAM-GO have micropores distribution on their macroporous walls.

The successful fabrication of hydrogel ISSGs was firstly evidenced by confirming their chemical structure from Fourier-Transform Infrared (FT-IR) spectra (Figure 4.2a). With the exception of PAMPSA-GO, PDMA-GO, and PAM-GO, which contain -C(=O)N- in the amide groups (1,640 cm^{-1}), all other hydrogels show a peak at 1,725 cm^{-1}, which is

attributed to the vibration of the carbonyl group (C=O). The characteristic absorption signals of all the hydrogels hydrophilic groups can be vividly distinguished from the spectra, including the peak observed at 1,030 cm^{-1} representing for the -SO_3H groups of PAMPSA-GO, the peak observed at 1,700 cm^{-1} representing for the -COOH groups of PAA-GO, the peak observed at 1,050 cm^{-1} representing for the -OH groups of PHEA-GO, the peak observed at 1,102 cm^{-1} representing for the -C-O-C- groups of PPEG-GO, the peak observed at 1,350 cm^{-1} representing for the -C-N bonding of PDMA-GO, the peak observed at 3,180 cm^{-1} representing for the -NH_2 groups of PAM-GO, and the peak observed at 1,480 cm^{-1} representing for the -N^+-C bonding of PAETAC-GO. In all, the FT-IR results demonstrated the successful synthesis of seven hydrogels.

To confirm the morphology of these hydrogel ISSGs, cross-section SEM has been performed (Figure 4.2b and 4.2c). With the same freeze-thawing process, all of the hydrogels presented numerous uniformly distributed interconnected interior channels for rapid water transport. Among them, PPEG-GO, PDMA-GO and PAM-GO had a hierarchical porous structure with micropores embedded in the microporous walls, allowing for adequate hydration effect with the water molecules. PAM-GO, in particular, exhibited more open macropores and thinner walls with denser and smaller micropores than the other two hydrogels, suggesting higher capacity to water transport and absorption. This distinctive porous structure may be related to differences in polymer chain flexibility and physical behavior during the freezing process, which influence ice crystal growth and phase separation dynamics. However, the correlation between the pore structure and the

ISSG performance is still a knowledge gap to address, as different literature illustrated seemingly contradictory conclusions. For example, a previous literature demonstrated that increasing pore size can ensure rapid water transport for higher evaporation rate (Guo et al., 2022), while another study proved that narrow channels can provide stronger capillary effect for better ISSG performance (C. Li et al., 2020). Therefore, in this work we used a quantifiable characteristic mostly influenced by the pore architectures, *i.e.* the water uptaking speed mentioned below, to assess the ISSG potential of hydrogels.

4.3.2 Hydrogels' Light Absorption and Water Uptaking Capability

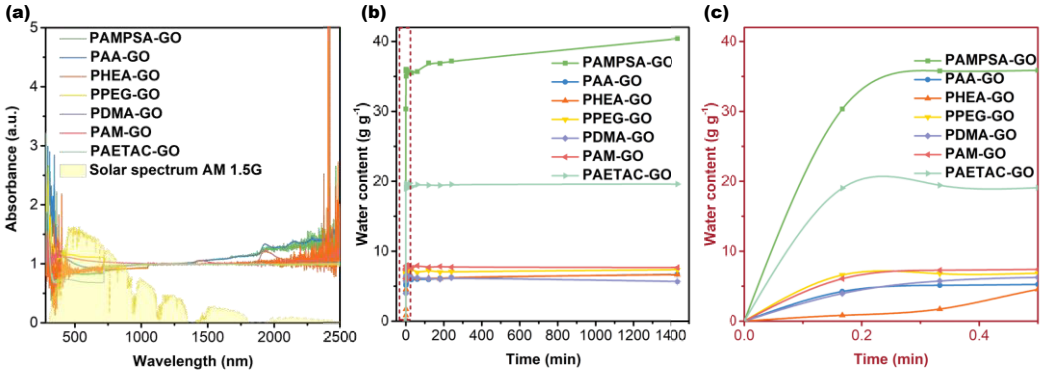

Figure 4.3 (a) UV-vis-NIR spectra of all the hydrogels and the solar spectrum (AM 1.5 G) with normalised spectral solar irradiance density (the light-yellow region) spanning the wavelength range of 280-2,500 nm. The water absorbed in the gel per gram of the dried gel plotted versus the absorption time within (b) 24 hours and (c) 30 s.

We conducted the UV-vis-NIR measurements to determine the light absorption ability of the hydrogels, which is essential for ISSG application (Figure 4.3a). With the same amounts of GO incorporated into the hydrogels as PTM, all the hydrogels exhibit extensive light absorption across the whole solar spectrum (from 280 to 2,500 nm),

indicating their similar light absorption capability.

Rapid water uptaking capacity can ensure sufficient water replenishment to the evaporation interface for continuous solar steam generation. For comparison, we dropped the dried gels into DI water, weighed the hydrogels' weight over time (m_t), and calculated the absorbed water content via equation (2):

$$\boldsymbol{Q = (m_t - m_0)/m_0} \qquad \text{Eq. (2)}$$

where m_0 is the dried gel's weight. As shown in Figure 4.3b, all the hydrogels can reach a saturated state within 30 seconds, suggesting rapid water uptaking capacity. Owing to the high charges of PAMPSA and PAETAC polymer chains, the saturated water content of corresponding hydrogels is much higher than other hydrogels. However, the absorption of too much water in the hydrogel can lead to heat loss to the bulk water and reduce solar steam generation performance. While the saturated water content of other neutral polymer hydrogels is around 7 g g^{-1}. Among them, the PPEG-GO, PDMA-GO and PAM-GO exhibited slightly higher saturated water content as well as faster water uptaking rate (Figure 4.3c), which can be attributed to their hierarchical porous structure. Of particular note, the more porous PAM-GO and PPEG-GO hydrogels showed similar water uptake behaviour, but the PAM-GO hydrogel's ISSG performance was better. This result can be attributed to the different effects of different pendant groups on water molecules.

4.3.3 Water Interaction Within the Hydrogels

To study the interaction between hydrophilic groups and the water molecules, we first used *Avogadro* software to simulate the chemical potential of weakened hydrogen bonding of IW based on mmff94 (Figures 4.4a, 4.4b, and Table 4.2). The strongly polarized electron-rich and -poor zones in the electrostatic potential maps (Figure 4.4c) guarantee the hydrophilicity of these hydrogels (Isikgor et al., 2021). For a simplified and straightforward comparison, we introduced one water molecule to a specific polymer repeating unit as the BW, and then attached the second water molecule to the first as the IW. We subsequently simulated the energy difference E_{hyd} of a single polymer repeating unit before and after an IW escaping. Thus, the E_{hyd} value is arguably to reflect the difficulty of freeing the attracted IW from hydrogen bonding with the BW on different functional groups. The simulated E_{hyd} values for PAMPSA-GO, PAA-GO, PHEA-GO, PPEG-GO, PDMA-GO, PAM-GO and PAETAC-GO are 23.94, 17.17, 12.51, 9.64, 8.96, 6.68, and 26.78 kJ mol^{-1}, respectively. The E_{hyd} values towards different groups can be ranked from low to high: $-NH_2$ < $-N(CH_3)_2$ < -C-O-C < -OH < -COOH < $-SO_3H$ < $-N^+(CH_3)_3Cl^-$.

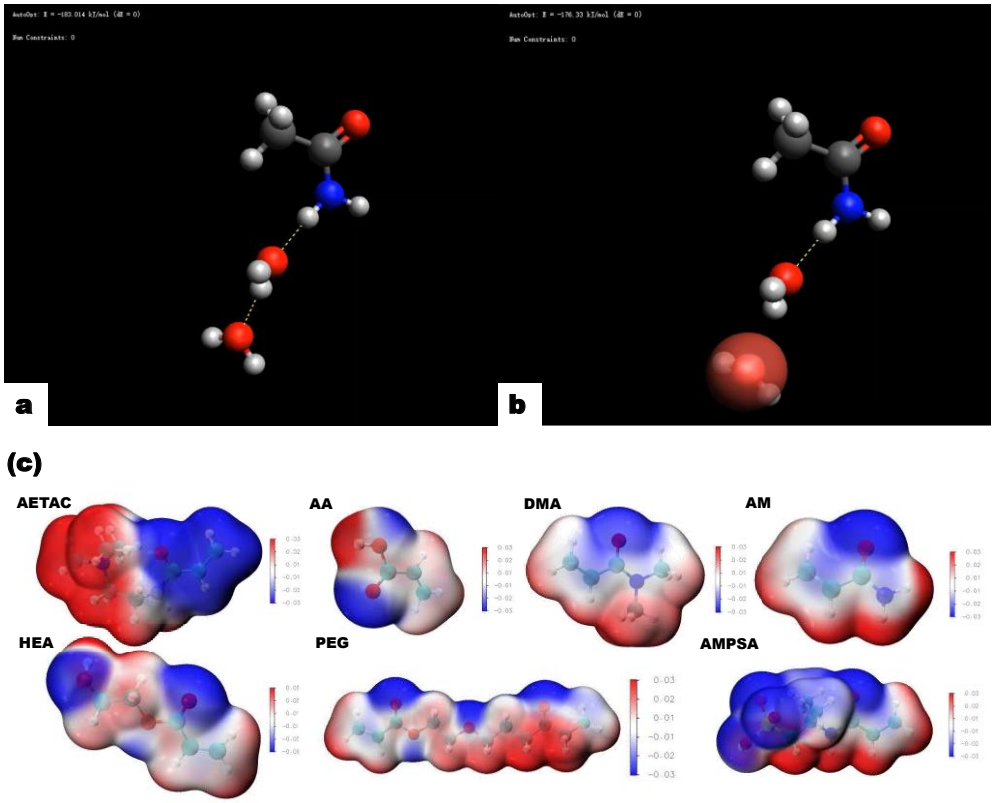

Figure 4.4 The molecule model and the automatic computed energy of (a) the -NH_2 group in PAM connected with two water molecules via hydrogen bonding and (b) the moment of dragging the second water molecule to break the hydrogen bonding between the water molecules. (c) Electrostatic Potential Maps of the polymer repeating unit.

Table 4.2 The energy E_0 and E_1 output by the *Avogadro*, and the simulated hydrogen bonding energy E_{hyd} of IW.

Sample name	E_0 (kJ mol^{-1})	E_1 (kJ mol^{-1})	E_{hyd} (kJ mol^{-1})
PAMPSA-GO	-361.19	-337.25	23.94
PAA-GO	-190.17	-173.00	17.17
PHEA-GO	-24.23	-11.72	12.51
PPEG-GO	150.36	159.99	9.64
PDMA-GO	-124.32	-115.36	8.96
PAM-GO	-183.01	-176.33	6.68

PAETAC-GO	4.32	31.10	26.78

The IW content was then determined by Raman measurements (Figures 4.5a-4.5h). The characteristic peaks of free water with four hydrogen bonds are located around 3,233 cm^{-1} and 3,401 cm^{-1} and were labeled in pink, while the characteristic peaks of intermediate water with weaken bonds are located near 3,514 cm^{-1} and 3,630 cm^{-1} and were indicated in light blue (Zhao et al., 2018; Zhou et al., 2018). The ratio of the intermediate water to the sum of intermediate water and free water [IW:(IW+FW)] derived from the integrated areas under the fitting peaks is commonly used to indicate the intermediate water content. As seen, PAMPSA-GO and PAETAC-GO showed a relatively low IW content of 0.559 and 0.538, respectively, compared to the other neutral polymer-based hydrogels. Although the hydrogels based on highly charged polymers can adsorb large amounts of water, resulting in a high swelling ratio, most of them are FW. For neutral polymer hydrogels, PAM-GO exhibits the highest IW content of 0.782, followed by PDMA-GO, PPEG-GO, PHEA-GO, and PAA-GO. To summarize, the IW content in hydrogels can be ranked from high to low as $–NH_2$ > $–N(CH_3)_2$ > -C-O-C- > –OH > –COOH > $–SO_3H$ > –

$N^{+}(CH_3)_3Cl^{-}$. Interestingly, this is the opposite of the orderliness of hydrogels E_{hyd}.

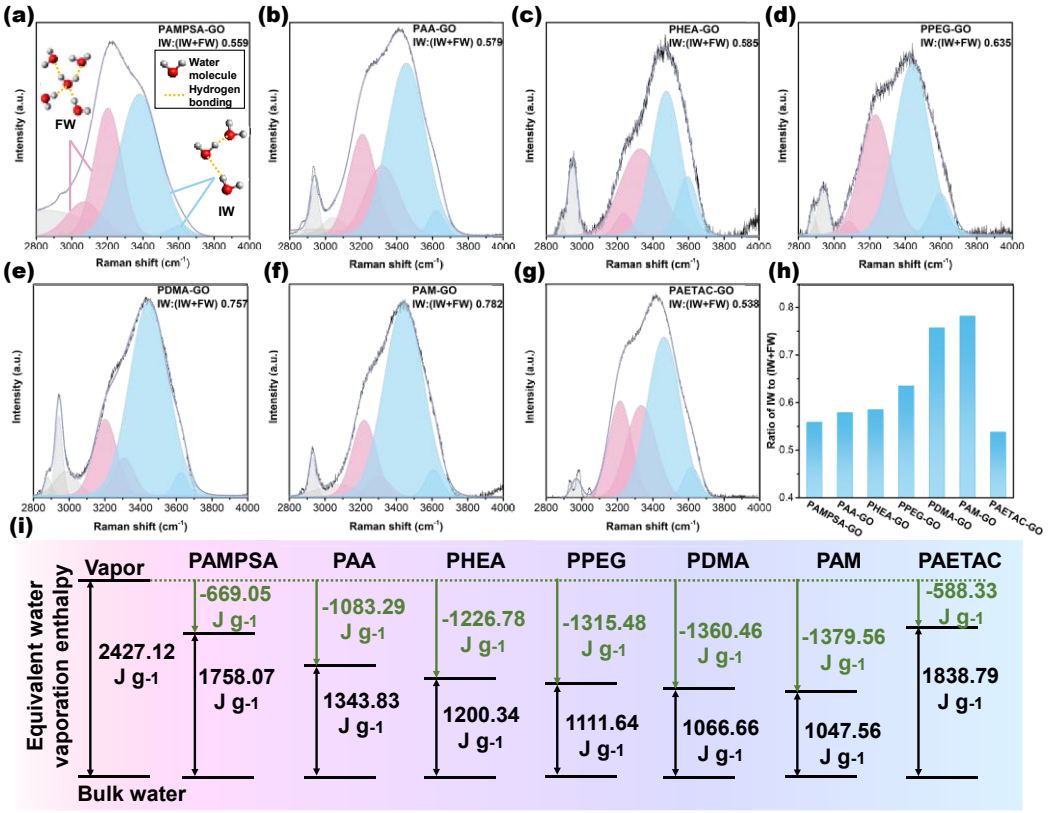

Figure 4.5 The fitting curves for (a) PAMPSA-GO, (b) PAA-GO, (c) PHEA-GO, (d) PPEG-GO, (e) PDMA-GO, (f) PAM-GO, and (g) PAETAC-GO in their Raman spectrum, and the pink and light blue peaks correspond to free and intermediate water, respectively. The inset figures are the schematic illustration of the water molecule configuration. (h) The IW:(IW+FW) ratios of all the hydrogels calculated from their Raman spectrum in the O-H stretching energy area. (i) The equivalent water vaporization enthalpy of the water in the hydrogels, the green enthalpy drop represents for the enthalpy reduced by the interaction between the water molecules and corresponding hydrophilic group.

After investigating the E_{hyd} values and IW/(IW+FW) ratios of the different hydrogels, we calculated the equivalent water vaporization enthalpy of the hydrogels by DSC-TGA measurements (Figure 4.5i). Compared to bulk water, all the hydrogels' equivalent water vaporization enthalpies were reduced due to the generation of large amount of IW in the

hydrogels which require much less energy for evaporation. It can be found that the water absorbed in PAM-GO has the lowest equivalent water evaporation enthalpy of 1047.56 J g^{-1}, while the water absorbed in PAMPSA-GO and PAETAC-GO has a higher equivalent water evaporation enthalpy.

4.3.4 ISSG Tests

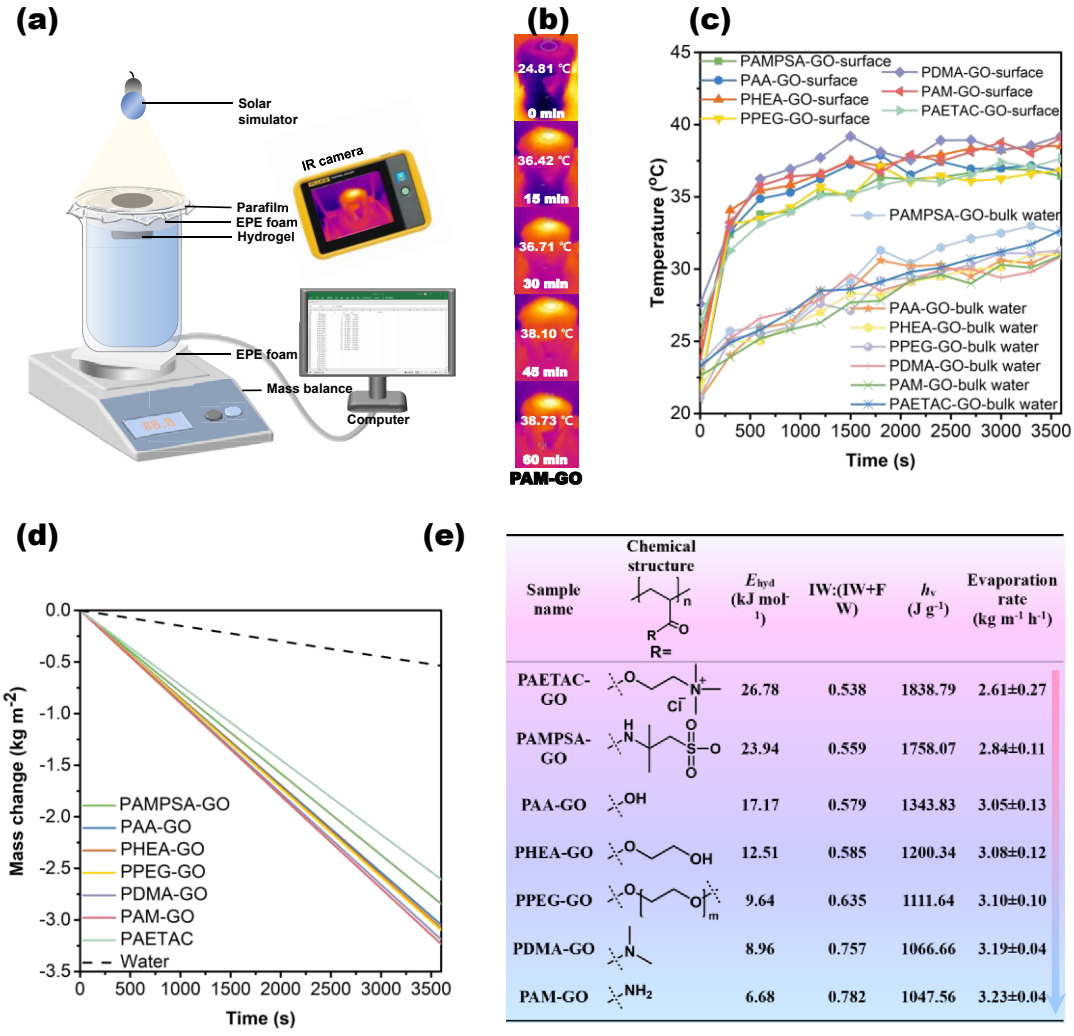

Sample name	Chemical structure (R=)	E_{hyd} (kJ mol^{-1})	IW:(IW+FW)	h_v (J g^{-1})	Evaporation rate (kg m^{-1} h^{-1})
PAETAC-GO		26.78	0.538	1838.79	2.61±0.27
PAMPSA-GO		23.94	0.559	1758.07	2.84±0.11
PAA-GO		17.17	0.579	1343.83	3.05±0.13
PHEA-GO		12.51	0.585	1200.34	3.08±0.12
PPEG-GO		9.64	0.635	1111.64	3.10±0.10
PDMA-GO		8.96	0.757	1066.66	3.19±0.04
PAM-GO		6.68	0.782	1047.56	3.23±0.04

Figure 4.6 (a) Schematic illustration of the ISSG setup. (b) The infrared images of the PAM-GO at the 0 minute, 15 minutes, 30 minutes, 45 minutes and 60 minutes during the ISSG testing. (c) The surface temperatures and bulk water temperatures of the hydrogels calculated from the infrared images during one-hour ISSG testing under one sun. (d) Water mass loss of the hydrogels and pure water under one sun. Notably, all of the data were calibrated with dark evaporation data. (e) Structure-property-application relationships of the polymeric hydrogels.

After thoroughly investigating the interactions between polymer hydrogels and water molecules absorbed, we used a home-made setup (Figure 4.6a) to determine their ISSG performance under one sun. To ensure that the testing hydrogel can perpendicularly float on the water surface, it was fixed in the middle of a EPE foam. For minimizing the impact of additional variables, a parafilm was used to seal minute gaps between the foam edge and the container wall to prevent any bulk water evaporation, while a thick EPE foam was added beneath the container to prevent the heat transfer to the mass balance. A portable infrared camera was used to take thermal images (Figure 4.6b) to record the evaporation surface temperature and the bulk water temperature during the ISSG process. As shown in Figure 4.6c, all hydrogel surfaces could reach a dynamic equilibrium temperature of 37-39 ^{o}C after *approx.* 20 minutes irradiation. The bulk water temperatures (around 30 ^{o}C) were significantly lower than the surface temperatures, suggesting the thermal confining capability of the polymeric hydrogel. The PAMPSA-GO and PAETAC-GO absorbed too much FW, resulting in increased heat loss to the bulk water, and thus higher bulk water temperatures. The mass loss of hydrogels was recorded using a mass balance. As shown in Figure 4.6d, the steam generation rates of all the hydrogel-based ISSGs were significantly quicker than that of pure water. These evaporation rates were also in good agreement with their corresponding intermediate water content and equivalent water vaporization enthalpies. PAMPSA-GO and PAETAC-GO presented much lower evaporation rates than the neutral polymer hydrogels, owing to their lower intermediate water contents, higher heat loss to bulk water, and higher equivalent water

vaporization enthalpies. The evaporation rates of neutral hydrogels with the following functional groups can be ranked from high to low as follows: $–NH_2$ > $–N(CH_3)_2$ > -C-O-C- > –OH > –COOH > $–SO_3H$ > $–N^+(CH_3)_3Cl^-$. Among them, the highest evaporation rate of ISSG based on PAM-GO was 3.23 kg m^{-2} h^{-1}. Furthermore, the solar-to-vapor energy conversion efficiency of ISSG systems were calculated by equation (1) in Chapter 2. The energy efficiency of the PAM-GO based ISSG is 94.1 %.

Overall, the structure-property-application relationships of the hydrogel-based ISSG have been illustrated in Figure 4.6e. The differences in the chemical structure of hydrogels are mainly reflected in the diverse hydrophilic functional groups contained in the repeating units, which can arouse distinct interactions with the BW molecules and hence IW. The groups with high potentials such as $-SO_3H$ and $-N^+(CH_3)_3Cl^-$ groups can establish strong interaction with the water molecules, as evidenced by the high energy that IW required to overcome the hydrogen bonding, the massive quantities of FW, and the high equivalent water evaporation enthalpy. As a result, the corresponding PAMPSA-GO and PAETAC-GO ISSGs showed lower evaporation rates than that of other neutral polymer hydrogels. They are able to establish mild interaction with the water molecules, which is reflected in the fact that IWs are more readily released from hydrogen bonds. The higher content as well as the easier vaporization of the IW can guarantee lower equivalent water vaporization enthalpy and better ISSG performance. Hydrophilic groups in our study can be rated as follows in terms of their potential for ISSG application: $-N^+(CH_3)_3Cl^-$ < $-SO_3H$ < -COOH < -OH < -C-O-C- < $-N(CH_3)_2$ < $-NH_2$, giving a guideline for the selection of

raw materials in the fabrication of the hydrogel ISSGs.

4.3.5 Desalination Performance in Real Seawater

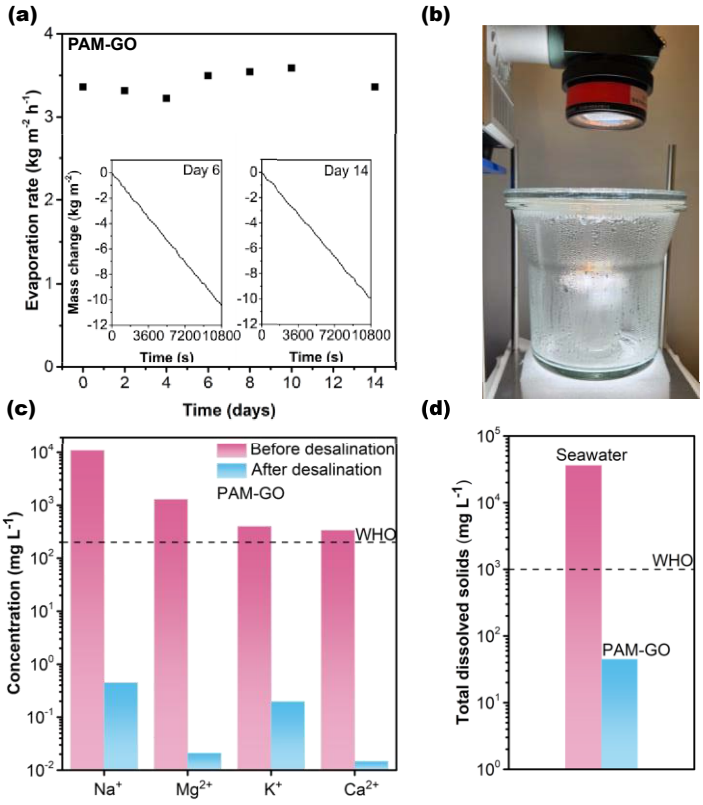

Figure 4.7 PAM-GO hydrogel based SVG desalination performance. (a) The evaporation rates of PAM-GO after being exposed to seawater for different days in 15 days. Insets: Solar vapor generation performance after one and two weeks of exposure to seawater. (b) The sealed jar for the condensed water collection. (c) The four primary ion concentrations of the seawater and the condensed water. (d) The total dissolved solids of the seawater and the condensed water.

Finally, the hierarchical porous PAM-GO ISSG with pendant amino groups, which stands out from the other six hydrogels, has been applied in seawater desalination (Figure 4.7). The seawater used for desalination was obtained from Darling Harbour (Sydney, Australia; E151.20º, S33.87º) with a total dissolved solids of 36.2 g L^{-1}. The PAM-GO has been set in a container same as Figure 4.6a but full of seawater for half a month and was taken to

conduct a three-hours continuous ISSG test everyday (Figure 4.7a). It can maintain its evaporation rate during the fifteen times of repetition, and could reach a high average rate of 3.41 kg m^{-1} h^{-1}, showing good durability in seawater. No appreciable salt accumulation was seen on the hydrogel's surface after daily desalination, indicating good salt resistance. This could be attributed to the hydrogel's rapid water replenishment capability, which impede rapid concentration decline at the evaporation surface and super-saturation of salt solutions (Loo et al., 2021). In addition, the evaporation rates of other hydrogels in seawater desalination followed the similar trend as that in DI water (Figure 4.8). For further analyse the desalination effect, we employed a sealed jar with glass cover to collect the condensed water (Figure 4.7b). After longtime desalination, the condensed water in the jar was collected for ICP-MS analysis (Figure 4.7c) and total dissolved solids measurement (Figure 4.7d). Compared to the untreated seawater, the concentrations of the four principal ions (Na^+, Mg^{2+}, K^+ and Ca^{2+}) and the total dissolved solids in the condensed water have been lowered by three to five orders of magnitude, and of course are lower than the World Health Organization (WHO) recommended levels for drinking water (Organization, 2004, 2009a, 2009b; WHO & Geneva, 2011).

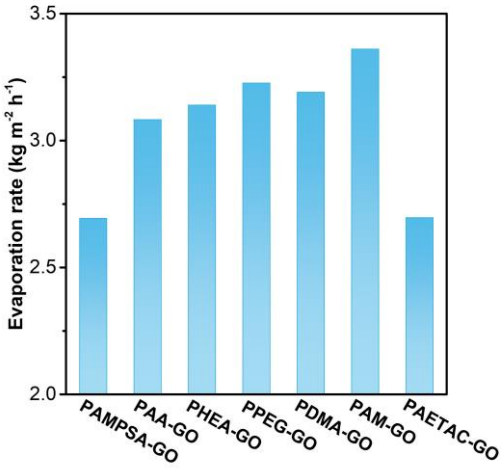

Figure 4.8 Evaporation rates of the hydrogels in real seawater.

4.4 Conclusion

In this chapter, we prepared a series of hydrogels for ISSG application. The highly charged polymeric hydrogels with $-SO_3H$ or $-N^+(CH_3)_3Cl^-$ groups showed relatively poor ISSG performance due to their high FW absorption ratio as well as strong interaction with water molecules. In contrast, the hierarchical porous PAM-based ISSG exhibits excellent water evaporation rate and outstanding durability and desalination capability. To discover the structure-property-application relationships of hydrogel ISSG, we investigated the interactions between polymer chains and water molecules in detail, studied swelling ratio and water replenishment capability, calculated the IW contents and evaporation enthalpies, and fairly compared their ISSG performance. Our study in this chapter shows that under the same experimental conditions, hydrophilic hydrogels can be ranked as follows in terms of their potential for ISSG application: $-N^+(CH_3)_3Cl^-$ < $-SO_3H$ < -COOH < -OH < -C-O-C- < $-N(CH_3)_2$ < $-NH_2$. We thus believe that our study could fill the knowledge gap

in hydrogel ISSGs and promote the development of next generation ISSG technology.

CHAPTER 5
Microscale: Efficient Water Transport in Optimized Pore Structures

This chapter has been derived from the published paper of **Mao, S.**, Onggowarsito, C., Feng, A., Zhang, S., Fu, Q., & Nghiem, L. D. (2023). A cryogel solar vapor generator with rapid water replenishment and high intermediate water content for seawater desalination. *Journal of Materials Chemistry A*, 11(2), 858-867.

Building on the molecular-level understanding of water–polymer interactions established earlier, the focus now shifts toward optimizing hydrogel structure at the microscale. While nanoscale hydrophilicity determines water binding, efficient solar evaporation also requires rapid and sustained water transport. This chapter explores how interconnected macropores can be engineered through careful polymer selection to enhance internal water movement, thereby improving evaporation continuity and overall system performance.

5.1 Introduction

Water scarcity is a serious issue faced by all human beings (Chakkaravarthy, 2019). One of the most effective methods to alleviate this issue is to extract freshwater from the ocean or other abundant salty water resources (AlMarzooqi et al., 2014; Khawaji et al., 2008; Panagopoulos et al., 2019; Semiat, 2008). However, the majority of the desalination technologies in commercial use are energy intensive (Al-Amshawee et al., 2020; Al-Karaghouli & Kazmerski, 2013; Semiat, 2008) or require significant investment, and ongoing operations and maintenance expenses (Tang et al., 2018). ISSG technology has recently emerged as a potential alternative to conventional desalination technologies as it can harvest solar energy and lower the latent evaporation enthalpy to efficiently evaporate water, and then condense the vapor to produce freshwater (Deng et al., 2017; Ma et al., 2017; Neumann et al., 2013).

ISSG performance is regulated by thermal and water management (Mao et al., 2022; F.

Zhao et al., 2020; Zhou, Guo, et al., 2019). Significant efforts have been made to further improve the thermal management, including by developing advanced photothermal materials (Ibrahim et al., 2021; Y. Wang et al., 2021; Yang et al., 2020) to improve photo-thermal conversion, constructing rough surfaces to reduce light reflection (Guo, Zhao, et al., 2019; Y. Lu et al., 2021; F. Yang et al., 2021), and optimizing heat insulation to reduce heat loss (Y. Guo, H. Lu, et al., 2020; Z. Liu et al., 2021; Tan et al., 2019; Tian et al., 2021; B. Wen et al., 2021; X. Wu et al., 2021; X. Zhang et al., 2020; Zhou et al., 2021). However, with enhanced thermal management alone, the ISSG evaporation rate is limited to the maximum theoretical value of 1.59 kg m^{-2} h^{-1} even at solar radiation of 1 kW m^{-2} (Chen et al., 2022; T. Li et al., 2021). Water management, or the balance between evaporation and the supply of liquid water, is also critical and has to date been mostly neglected. Well-designed water management can reduce evaporation enthalpy by increasing the ratio of intermediate water to free water (Guo, Zhou, et al., 2019; Lapotko, 2009; H. Wang et al., 2020; X. Zhang et al., 2020; Zhao et al., 2018).

One strategy to improve water replenishment is to use the direction freezing method (He et al., 2021; Yu & Wu, 2020) or 3D printing technique (Wang et al., 2022) to construct vertically aligned channels within the hydrogels. However, these fabrication methods are cumbersome or time-consuming, hindering the large-scale fabrication and application of these ISSG systems. Since the hydrogels hydrophilic matrix can trigger particular water states, and induce the generation of intermediate water (with weakened water-polymer bonds) that can escape more readily from the neighboring molecules than the other types

of water (*i.e.* free water or bonded water). Thus, another applied strategy is to promote the generation of more intermediate water in the hydrogel ISSG to lower the overall water evaporation enthalpy (Guo, Zhou, et al., 2019; Lapotko, 2009; H. Wang et al., 2020; X. Zhang et al., 2020; Zhao et al., 2018). As a result, the advent of a novel hydrogel-based platform with special water management strategies has brought the material design of ISSG to a new level, enabling evaporation rates beyond the aforementioned limit (Zhao et al., 2018; X. Zhou et al., 2020).

Cryogel (also known as cryotropic hydrogel) is a macroporous material of significant scientific and engineering value (Baimenov et al., 2020; Gun'ko et al., 2013; Lozinsky, 2002, 2014; Lozinsky & Okay, 2014; Okay & Lozinsky, 2014). Compared with conventional hydrogels, cryogels exhibit much higher water uptake rate due to interconnected pores and enhanced mechanical robustness due to the 'thicker' walls. Through judicious selection of monomers, we saw this is an opportunity to develop a novel cryogel ISSG system by a facile approach to improve water replenishment and intermediate water content at the same time.

Herein, we report the development of a novel cryogel ISSG for energy-saving desalination applications. The functional monomers HEA, and PEGDA were employed to synthesize cross-linked hydrogels. Lower precursor concentrations were employed compared to Chapter 4 to provide greater flexibility for pore formation. Due to their low T_gs, we then prepared PHEA- or PPEG-based cryogels by freezing hydrogels at -18 ºC

and thawing them. As expected, the resultant cryogel ISSGs have rapid water replenishment and high intermediate water content at the same time, and hence managed to achieve low evaporation enthalpy (861.5 kJ Kg^{-1}) and high water evaporation rate of 3.59 kg m^{-1} h^{-1} under one sun. Furthermore, such ISSGs also exhibit high durability, high salt resistance and excellent desalination competence in real seawater desalination, making them prospective for future practical applications.

5.2 Experimental Section

5.2.1 Chemicals

Chemicals including GO powder (15-20 nanosheets, 4-10% edge-oxidized), PVA (MW 89000-98000), GA solution (25 wt% in DI water), hydrochloric acid (32 wt% in DI water), HEA (96 wt% in DI water), MBA, TEMED, APS, PEGDA (average M_n = 575 g mol^{-1}) were all purchased from Sigma-Aldrich and used without further purification.

5.2.2 Synthesis of PVA-based Hydrogels

Typically, PVA (100 mg, MW = 89,000-98,000 g mol^{-1}) was added into a GO solution (1.9 mL, 1 mg/mL in DI water) and heated under 80 ℃ for 5 hours (A). Then, GA solution (40 μL, 25 wt% in DI water) and DI water (41 uL) were added in and mixed together by sonication. Next, HCl (50 μL, 32 wt% in DI water) were added to trigger the gelation. The obtained gel was frozen overnight at -18 ℃, thawed in DI water overnight, and washed with DI water three times to obtain a pure PVA-GO-5 hydrogel. PVA-GO-10 was

prepared in a similar manner, merely changing the amount of the PVA and GA used. All the hydrogels were freeze-dried before characterization, and saturated in DI water or seawater before SSG tests.

5.2.3 Synthesis of PHEA-based Cryogels

Typically, HEA (87.16 mg, 96 wt% in DI water), *N,N'*-methylenebis(acrylamide) (12.83 mg), TEMED (10 μL) and GO solution (1.9 mL, 1 mg/mL in DI water) were mixed together by sociation. Then an APS solution (1 mL, 0.03 g/mL in DI water) was added in and mixed together to trigger the gelation. The obtained gel was frozen overnight at -18 ℃, thawed in DI water overnight, and washed with DI water three times to obtain a pure PHEA-GO-5 cryogel. PHEA-GO-10 was prepared in a similar manner, merely changing the amount of the HEA and MBA used. All the cryogels were freeze-dried before characterization, and saturated in DI water or seawater before SSG tests.

5.2.4 Synthesis of PPEG-based Cryogels

Typically, PEGDA (100 mg, average Mn 575 g mol^{-1}), TEMED (10 μL) and GO solution (1.9 mL, 1 mg/mL in DI water) were mixed together by sociation. Then an APS solution (0.1 mL, 0.03 g/mL in DI water) was added in and mixed together to trigger the gelation. The obtained gel was frozen overnight at -18 ℃, thawed in DI water overnight, and washed with DI water three times to obtain a pure PPEG-GO-5 cryogel. PPEG-GO-10 was prepared in a similar manner, merely changing the amount of the PEG used. All the

cryogels were freeze-dried before characterization, and saturated in DI water or seawater before SSG tests.

5.2.5 Characterizations

The internal morphology of the hydrogels was observed using a Zeiss scanning electron microscope (10–30 kV). FT-IR was obtained with Shimadzu MIRacle 10 FT-IR. UV-vis-NIR absorbance spectra was collected using a Shimadzu 1700 UV–Vis-NIR spectrophotometer operating in the wavelength range 300-2500 nm. Raman spectrum was collected by a Renishaw Raman spectroscopy. The heat change of gels from room temperature to 200 °C was monitored using a Q600 SDT Thermal Analyzer (DSC-TGA) at a heating rate of 10 °C min^{-1}. The ion concentrations in the desalinated water and seawater were analyzed with Agilent 7900 ICP-MS. The TDS of the desalinated water and seawater were tested by a HQ40D Portable Multi Meter.

5.2.6 Interfacial Solar Steam Generation Tests

A solar simulator (NBeT HSX-F3000 xenon light source) was used to produce 1 sun irradiation (1 kW m^{-2}) and the solar irradiance on the gel surface was measured by a compact power and energy meter console (PM100D, Thorlabs, Germany) with a thermal power sensor (S405C, Thorlabs, Germany). The gel for testing was fixed in a EPE foam, and floated on the top of a beaker full of DI water or seawater. A Paraffin film was used to cover a few tiny spaces between the EPE foam and the beaker to prevent the potential

impact of bulk water evaporation. The mass changes during the ISSG process were recorded by an electronic mass balance (OHAUS Pioneer IC-PX 124) every 4 minutes. There was also a EPE foam between the beaker and mass balance for thermal insulation. The evaporation rates were estimated by the slopes of the mass−time curve via linear fitting. The temperatures of the hydrogel surface and the bulk water during the ISSG tests were collected every 5 minutes by a Fluke PTi120 pocket thermal imager.

5.3 Results and Discussion

5.3.1 Pore Construction in Hydrogels and Cryogels

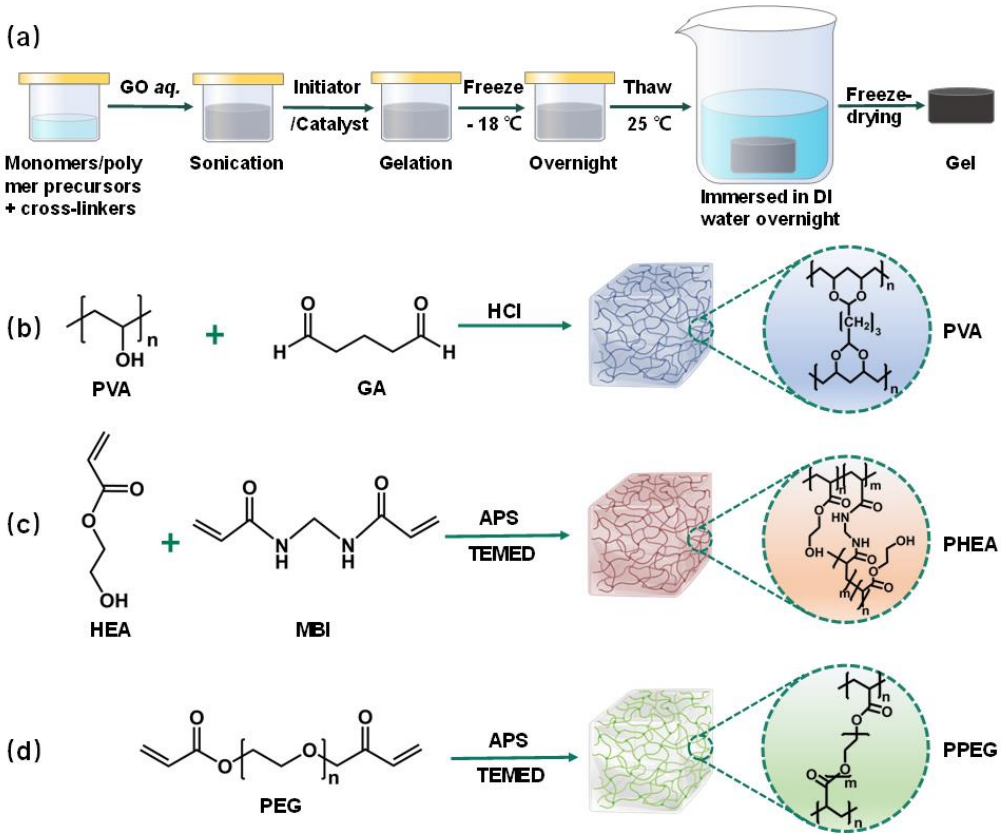

Figure 5.1 (a) Schematic of the preparation process of the gels and the schematic of chemical structures of all the components during the gelation of (b) PVA gels, (c) PHEA gels, and (d) PPEG gels.

In this study, PHEA and PPEG-based cryogels were prepared and evaluated against a conventional PVA hydrogel in the same freeze-thaw process for comparison (Figure 5.1a). Specifically, three vials were charged with PVA and GA (conventional hydrogel), HEA and MBA (PHEA-based cryogel), and PEGDA (PPEG-based cryogel) in DI water (Figure 5.1). These vials were denoted as solutions I, II and III, respectively. Then, the same amount GO dispersion (as PTMs) was added into above solutions, followed by 5 min sonication. Thereafter, the catalyst (HCl) or initiators (APS/TEMED) were added to the solutions I, or II and III, respectively and the mixtures were left steady for 5 min to afford gels (Figure 5.1). The chemical structures of the precursors and the reaction schemes were illustrated in Figures 5.1b-5.1d. Then, these gels were placed in a freezer at -18 ºC overnight, thawed in DI water at room temperature, and freeze-dried overnight for characterization and water evaporation tests. We prepared a series of gel ISSGs with different solid contents, such as 5 or 10 wt%. The resulting ISSGs are denoted as P-GO-x, where P represents PHEA, PPEG or PVA and x represents the corresponding solid contents in the gel.

The T_gs of the PHEA and PPEG chains are *ca.* -30 ºC (Dech et al., 2012) and -60 ºC (Southan et al., 2014; Vrandečić et al., 2010), respectively (< -18 ºC), while the T_g of PVA is *ca.* 60 ºC (Koosha et al., 2015). Therefore, the PPEG and PHEA chains are in a rubbery state and can maintain good mobility (i.e. flexible) during the freezing process, while PVA chains are in a crystalline state (Shrivastava, 2018). As a result, the ice crystals in the PPEG and PHEA gels can grow bigger and bigger until their polymer chains huddle

together (Figure 5.2b-I and II), leading to the formation of thick walls and interconnected macropores after thawing (Figure 5.2b-III). In contrast, the rigidity of PVA chains is due to their relatively high T_g. We, thus, obtained a conventional PVA hydrogel with smaller pore size (Figure 5.2a-III).

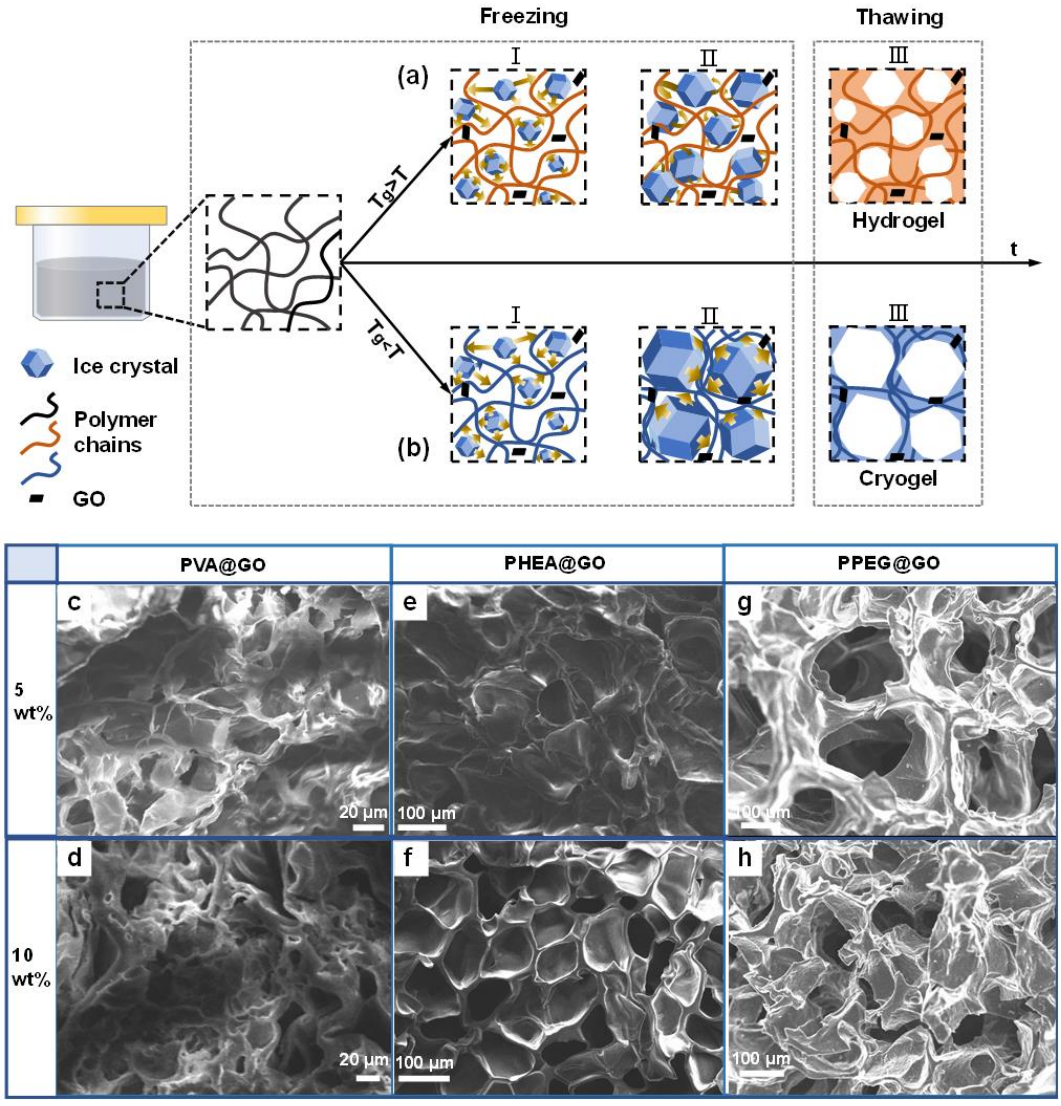

Figure 5.2 Schematic diagram of the formation process of the (a) hydrogel and (b) cryogels. During the freezing process, (I) the ice crystals firstly generated and then (II) grew bigger with or without limitation of the polymer chains. (III) After thawing, the final gels with pores were obtained. Cross-section SEM images of (c) PVA-GO-5, (d) PVA-GO-10, (e) PHEA-GO-5, (f) PHEA-GO-10, (g) PPEG-GO-5, and (h) PPEG-GO-10 gels from a top-view.

The successful synthesis of the hydrogels and cryogels is first evidenced by the SEM images of the samples. Figures 5.2c-5.2h show the cross-section SEM images of all three gels. We found that all the gels are porous with abundant and generally uniform internal channels, which can provide pathways for water transport. As a result of the differences in T_g, PVA hydrogels have relatively smaller internal pores (~5-20 μm) compared with PHEA- (~90-110 μm) and PPEG-based cryogels (~70-130 μm) (Table 5.1). This result is in good agreement with the pore size properties of hydrogels (Zhang et al., 2022; Zhao et al., 2018; Zhou et al., 2018) and cryogels (Hu et al., 2019; Loo et al., 2021; J.-Y. Wang et al., 2021) reported in previous literature. Increasing the solid content of the polymer network usually leads to enhanced mechanical properties (Okay & Lozinsky, 2014). In this study, P-GO-10 samples always have smaller pores and thicker walls than that of the P-GO-5 samples (Table 5.1), as the P-GO-10 gels have double the solid content to form the matrix. To further confirm the freezing temperature's effect on the pore size, we also synthesized a counterpart of PPEG-GO-10 by freezing it with liquid nitrogen (-197 ºC), and denoted it as PPEG-GO-10-LN. As expected, it has a much smaller average pore size of ca. 9.5 μm (Figure 5.3 and Table 5.1).

Table 5.1 The average pore size and wall thickness of all the samples calculated from the cross-section SEMs via 'Imagej'.

Sample	Average pore size (μm)	Average wall thickness (μm)
PVA-GO-5	18.04	1.68
PVA-GO-10	5.69	2.93
PHEA-GO-5	108.22	5.71
PHEA-GO-10	97.96	11.82
PPEG-GO-5	130.52	10.24
PPEG-GO-10	78.70	18.00

PPEG-GO-10-LN	9.56	5.65

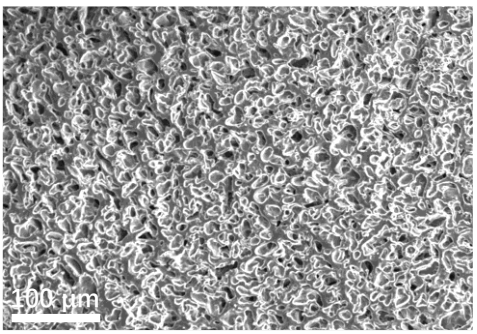

Figure 5.3 The porous structure shown via cross-section SEM image of PPEG-GO-10-LN.

5.3.2 Hydrogels' Water Transport Capability

Compared with a conventional hydrogel, rapid water transport competence is a distinctive and representative feature of cryogel ISSGs due to their interconnected macroporous structure. To investigate the difference in water uptake rate among the three ISSGs, we recorded the amount of water absorbed by the corresponding dried gels over time (m_t) when immersed in deionized water. The water content is calculated using equation (2) in Chapter 4. Figure 5.4a visually shows the capacity for absorbing water of hydrogels and cryogels. The dry PVA hydrogel ISSGs can fast absorb water at the initial stage (<20 min), and then the water uptake rate decreased. After 200 minutes, the water content of PVA-GO-10 and PVA-GO-5 reached a plateau (*aka.* saturated state) of 3.17 and 6.74 g g^{-1}, respectively. In sharp contrast, we found the cryogel ISSGs' weights *vs.* time curves are nearly vertical at first, suggesting they are almost full of water in less than a minute of contact with water. Their water contents fluctuated slightly over time. As shown in Figure 5.4c, with the same polymer contents, PPEG-based ISSGs have the highest saturated

water content of 18.44 and 10.58 g g^{-1} for PPEG-GO-5 and PPEG-GO-10, respectively. While the PHEA cryogels display a saturated water content of 15.68 and 8.08 g g^{-1} for PHEA-GO-5 and PHEA-GO-10, respectively. All these values are higher than that of PVA hydrogel ISSGs. Interestingly, when we doubled the polymer (solid) content of the gels, their saturated water content decreased by *ca.* 50%. This can be attributed to the smaller pores and 'thicker' walls in gels with higher polymer content. Notably, the rapid frozen PPEG-GO-10-LN sample showed a gradual water absorption, much slower than that of PPEG-GO-10 cryogel (Figure 5.4b). The slow water absorption speed and small pore size can further validate the synthesis of a conventional evaporator by freezing them below their T_gs.

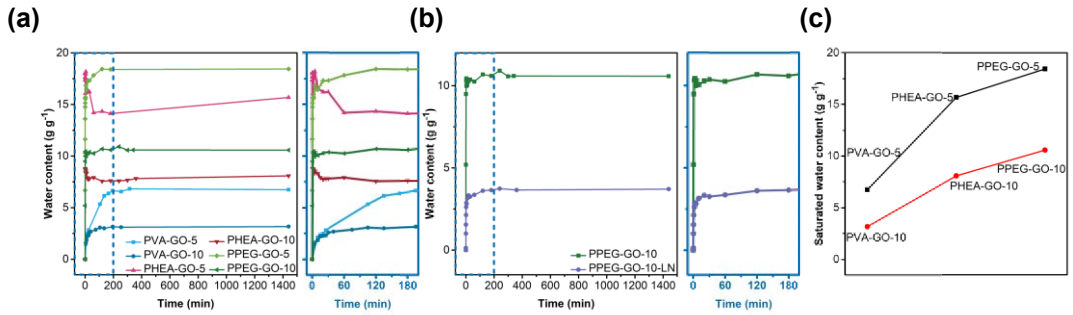

Figure 5.4 The water content of (a) the gel frozen at -18 ºC and (b) the gel rapid frozen by liquid nitrogen per gram of the corresponding dry gel plotted against water absorption time (the right figure represents for the first 200 minutes of water absorption). (c) The saturated water content in the well-saturated gel per gram of the corresponding xerogel.

5.3.3 Hydrogels' Chemical Structure and Light Adsorption Capability

FT-IR spectra of the PVA-GO-10, PHEA-GO-10 and PPEG-GO-10 were performed to confirm the chemical composition of the fabricated SSGs (Figure 5.5a). For PVA-based

hydrogel ISSG, we observed a characteristic absorption signal at 1,100 cm^{-1}, which can be attributed to the stretching vibrations of the secondary hydroxyl group (-CH-OH). In contrast, we observed the vibration peak of the primary hydroxyl (-CH_2-OH) at 1,050 cm^{-1} in the spectrum of PHEA-based cryogel. We also observed the peak at 1,724 cm^{-1}, which can be attributed to the vibration of C=O of PHEA or PPEG. What's more, owing to the cross-linker MBA used in the synthesis of PHEA cryogel, we observed the vibration peak of N-H at 1,650 cm^{-1}. At 1,102 cm^{-1} we found the characteristic peak of C-O-C of PPEG. In addition, we also found a signal at 944 cm^{-1}, which is attributed to the unreacted C=C groups of the PEGDA. Overall, these results demonstrate the successful preparation of PVA-, PHEA- and PPEG-based gels, and we can clearly distinguish these three polymer gels with different chemical structures based on their FT-IR spectra.

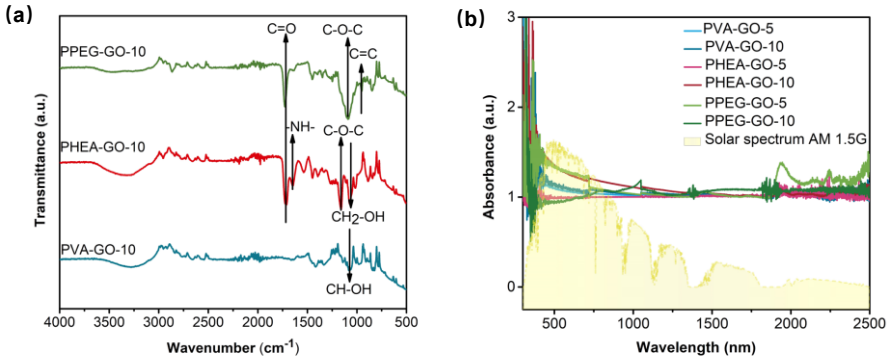

Figure 5.5 (a) FT-IR spectra of the PVA-GO-10, PHEA-GO-10, and PPEG-GO-10 gels showing their hydrophilic groups. (b) UV-vis-NIR spectra of the gels and the solar spectrum of air mass 1.5 global (AM 1.5 G) with normalised spectral solar irradiance density (the light yellow area) over the wavelength of 300-2,500 nm.

We then determine their solar absorption using a UV-vis-NIR spectrophotometer. As can be seen in Figure 5.5b, all ISSG gels containing trace amounts of GO as photothermal

materials (*ca.* < 2wt% of the xerogel weight) show a broad light absorption range over the entire solar spectrum (from 300 to 2,500 nm).

5.3.4 Intermediate Water Content

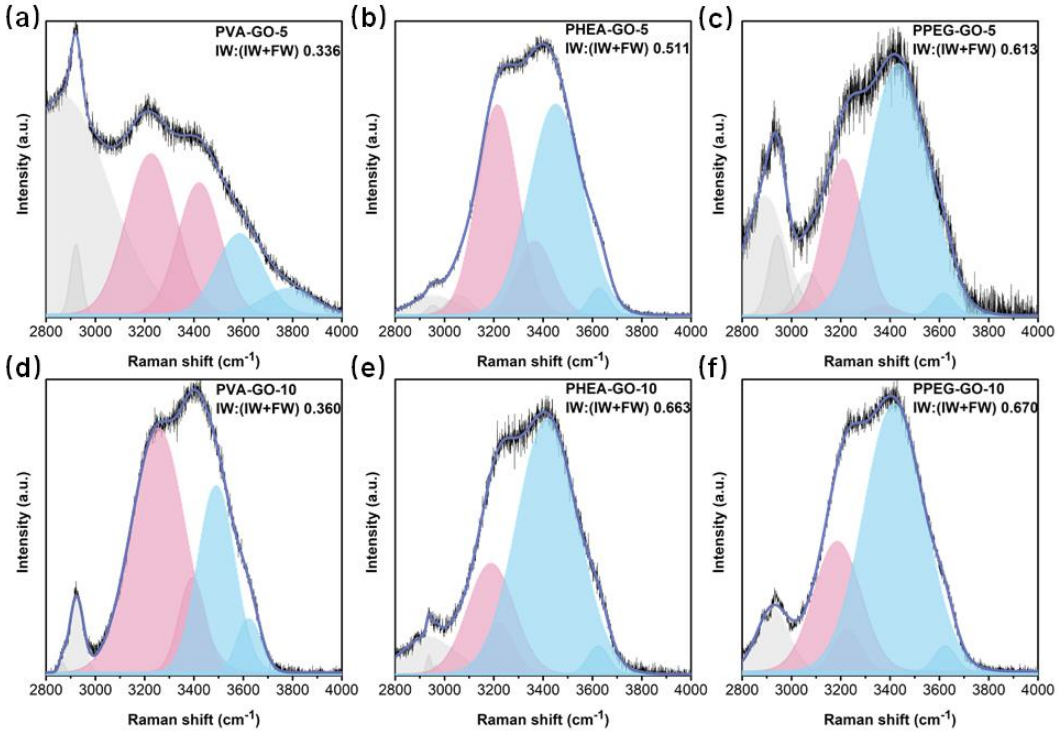

Figure 5.6 Fitting curves in the O-H stretching energy region for (a) PVA-GO-5, (b) PHEA-GO-5, (c) PPEG-GO-5, (d) PVA-GO-10, (e) PHEA-GO-10 and (f) PPEG-GO-10 in Raman spectrum. The pink peaks and light blue peaks represent free water and intermediate water, respectively.

Increasing intermediate water content in an ISSG system is an effective water management strategy to boost evaporation rate. Raman measurements of all gel samples (containing water) were conducted and their intermediate water contents were determined via peak fitting (Figures 5.6a-5.6f). The pink peaks at 3,233 cm^{-1} and 3,401 cm^{-1} represent for the free water with four hydrogen bonds, while the light blue peaks around 3,514 cm^{-1} and 3,630 cm^{-1} represent for the intermediate water with weaken hydrogen bonds (Zhao

et al., 2018; Zhou et al., 2018). The calculated molar ratio of (IW): (IW+FW) in PVA-GO-5, PHEA-GO-5 and PPEG-GO-5 were 0.336:1, 0.511:1 and 0.613:1, respectively. Intriguingly, although the P-GO-5 samples possess larger pore sizes and higher water absorption capacity, the P-GO-10 samples display higher (IW)/(IW+FW) ratio of 0.36:1, 0.663:1 and 0.67:1 for PVA-GO-10, PHEA-GO-10 and PPEG-GO-10, respectively. This result also suggests that different hydrophilic functional groups, such as primary or secondary hydroxyl groups and C-O-C ether groups, would have different activation ability to promote the generation of IW water. Unfortunately, it seems that previous studies have overlooked the impact of hydrophilic functional groups in the water managements.

5.3.5 ISSG Tests

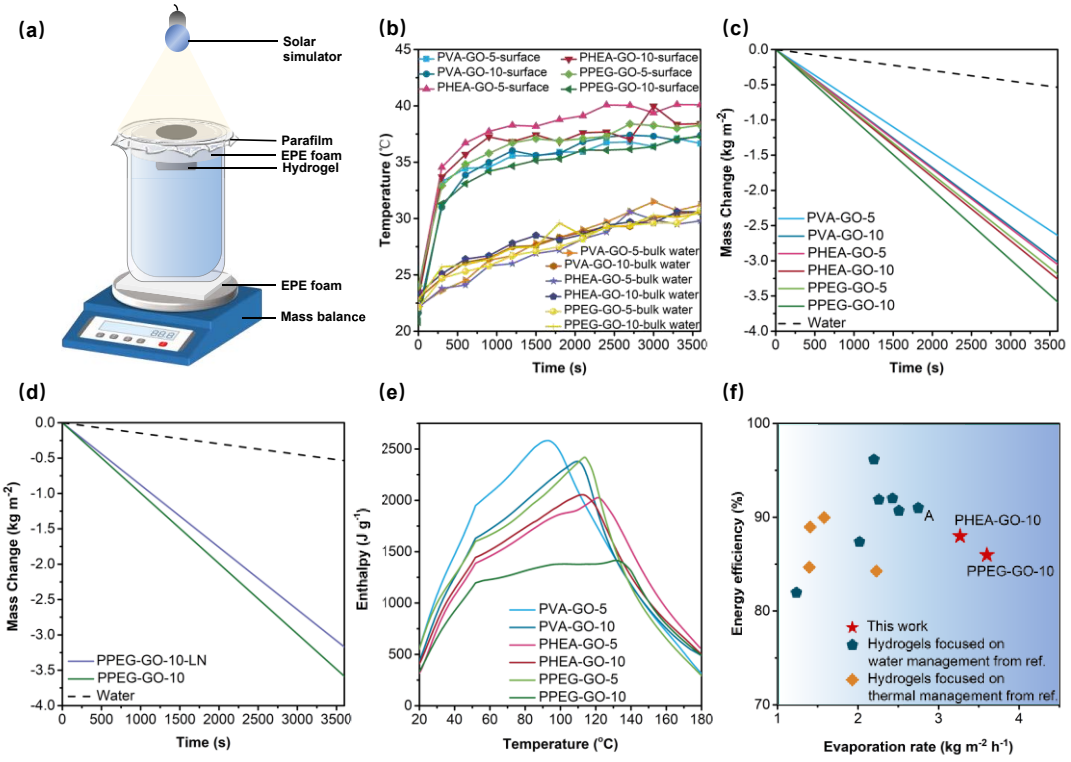

Figure 5.7 (a) The setup for the ISSG test. (b) The temperatures of the gel surface and bulk water

during the one hour of ISSG test under 1 sun. (c) Water mass changes of PVA hydrogels, PHEA cryogels, PPEG cryogels and the pure water without any gels during the solar steam generation test under 1 sun irritation. All the data have been calibrated with dark evaporation data and were estimated by the slopes of the mass−time curve via linear fitting. (d) Water mass changes of PPEG-GO-10, PPEG-GO-10-LN, and the pure water during the solar steam generation test under one sun irritation. (e) The calculated equivalent water vaporization enthalpy in the gel samples at various temperatures by DSC-TGA. (f) Comparison of the evaporation rate and energy efficiency to the hydrogel ISSGs in previous works with similar testing setup (The testing gel is fixed in the middle of a floating foam and the gel itself can directly contact the bulk water. Notely, the gel surface should not be much high above the foam surface). Detailed data are listed in Table 5.3.

With rapid water replenishment capability and higher IW content, the cryogel-based ISSGs are expected to display better solar steam generation performance, which were determined by using a homemade setup under one sun irradiation as shown in Figure 5.7a. The gel was fixed in the middle of the EPE foam to ensure that the ISSG can float on water surface, and paraffin film was used to seal any tiny gaps between the EPE foam and the container wall to prevent the potential bulk water evaporation. A balance was used to record the mass change of the container as a function of irradiation time and a thick EPE foam was also placed under the container to prevent potential heat transfer from the balance to the container. We took infrared images to record the temperatures of the evaporation surface and the bulk water during the solar steam generation process (Figure 5.7b). After 20 min irradiation, all ISSG surfaces could be heated to a dynamic equilibrium temperature of 37-40 ºC, which is higher than that of bulk water (*ca.* 30 ºC), indicating that the converted energy was confined on the surface of the gels. We then recorded the mass changes of the bulk water with ISSGs applied as a function of time. Of particular note, all the mass loss *vs.* time curves shown in Figure 5.7c have been calibrated by subtracting dark evaporation values and were estimated by the slopes of the mass

loss−time curve through a linear fitting. All of the ISSGs demonstrated substantially faster steam generation rate than that of pure water (without gels). Among them, cryogels PPEG-GO-10 and PHEA-GO-10 showed excellent ISSG performance with an evaporation rate of 3.59 and 3.26 kg $m^{-2}h^{-1}$ respectively, higher than that the PVA-GO-10 (3.02 kg $m^{-2}h^{-1}$). It is worth noting that the excessive water in PHEA-GO-5 resulted in heat loss at the evaporating interface (Yang et al., 2022; X. Zhang et al., 2020). As a result, even with a higher intermediate water content, the evaporation rate of PHEA-GO-5 is still similar to that of PVA-GO-10. Additionally, the evaporation rate of PPEG-GO-10-LN is lower than that of PPEG-GO-10 cryogel evaporator (Figure 5.7d).

Table 5.2 The calculated equivalent water evaporation enthalpy in the gel samples at the surface equilibrium temperature.

Sample	Surface equilibrium temperature (^oC)	Equivalent evaporation enthalpy (J g^{-1})
PVA-GO-5	36.66	1348.89
PVA-GO-10	37.38	1172.16
PHEA-GO-5	40.1	1104.17
PHEA-GO-10	38.43	972.74
PPEG-GO-5	38.29	1076.25
PPEG-GO-10	37.27	861.54

The EEW (Table 5.2) in this study were determined by DSC-TGA measurements (Figure 5.7e). The equivalent evaporation enthalpy of PVA-GO-10, PHEA-GO-10 and PPEG-GO-10 was 1172.2 J g^{-1}, 972.74 J g^{-1} and 861.5 J g^{-1}, respectively, which was in good agreement with the corresponding trend of intermediate water content and evaporation rate. The P-GO-5 ISSGs with lower polymer contents but higher saturated water contents showed lower evaporation rates, because of their relative lower intermediate water contents. Furthermore, the solar-to-vapor efficiency were calculated by equation (1) in Chapter 2. Although all the gel SSGs only contain < 2wt% of GO, their photo-thermal energy conversion efficiencies were all above 85%, indicating efficient utilization of solar energy (Figure 5.8).

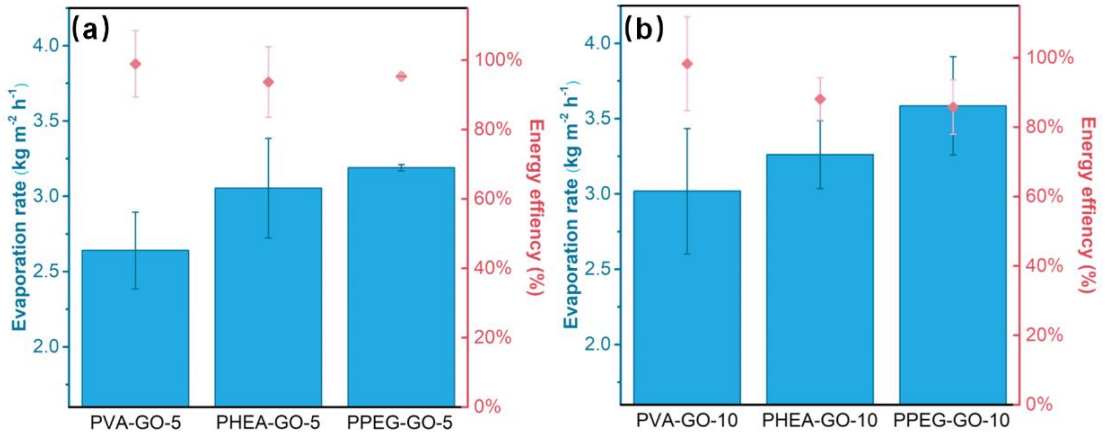

Figure 5.8 The evaporation rates and corresponding solar-to-vapor energy efficiencies of gels with (a) 5 wt% polymers and (b) 10 wt% polymers. We take the equivalent water evaporation enthalpy at the gel surface temperature for the calculation of energy efficiency. Each error bar shows the difference from at least two gel samples.

In previous literature, there have been several gel-based ISSGs showing better performance such as 3D evaporator (Xu et al., 2022) in which the side walls also

contribute to the evaporation. For fair comparison, we only collected the evaporation rate and energy efficiency data of the evaporators using similar ISSG testing setup, and the detailed comparison is shown in Figure 5.7f and Table 5.3. With this setup, all the reported ISSGs have good energy efficiency of >80 %.

Table 5.3 List of the ISSG performance of the hydrogels in previous work with similar testing setup.

Materials	**Evaporation rate (kg m^{-2} h^{-1})**	**Energy efficiency (%)**	**Ref.**
Carbon dots chitosan/carboxymethyl cellulose hydrogel	1.4	89	(Singh et al., 2019)
Molybdenum carbide/carbon-based chitosan hydrogel	2.19	96.15	(F. Yu et al., 2020)
Sodium alginate/PEDOT:PSS 3D hydrophilic network	1.23	82	(Zhao & Liu, 2020)
Bilayer PPy coating pre-pressed melamine foam	1.574	90	(Li et al., 2019)
CNT/cellulose nanocrystals nanocomposite coated on the PDMS sponge	2.01	87.4	(Liangliang Zhu, Tianpeng Ding, et al., 2019)
Benzoxazole-linked COF combined with the PDMS sponge	1.39	84.7	(Cui et al., 2021)
Agar/TiN cryogel	2.74	91	(Tian et al., 2022)
Agar hydrogel (AHG) with Prussian blue (PB) immobilized on cellulose nanofiber	2.22	84.3	(Lim et al., 2022)

PNAGA/chitosan/carbon nanotubes hydrogel	2.42	92	(Lu et al., 2022)
Bilayer lignin-PPy hydrogel	2.25	91.87	(Jiang et al., 2022)
PVA/PEDOT:PSS hydrogel	2.5	90.7	(Li et al., 2022)

We found that the evaporation rates of ISSG systems is not positively correlated with energy efficiency, suggesting that low water-equivalent evaporation enthalpies and fast rehydration rate determine the water evaporation rate of ISSG compared with high energy efficiency. Specifically, the hydrogel-based ISSGs that focused on water management (blue pentagons) mostly have higher evaporation rate than those that focused on thermal management (orange diamonds). For example, the ISSG point A presented (Tian et al., 2022) used the unidirectional freezing method to construct vertically rapid water transport channels, and it has much higher evaporation rate than other gels mainly focused on thermal management. Moreover, instead of using complex fabrication method (i.e. 3D printing), the ISSG PPEG-GO-10 reported in our work, with interconnected rapid water transport channels and high IW content, greatly surpassed all other ISSG systems including point A in term of performance.

5.3.6 Desalination Performance in Real Seawater

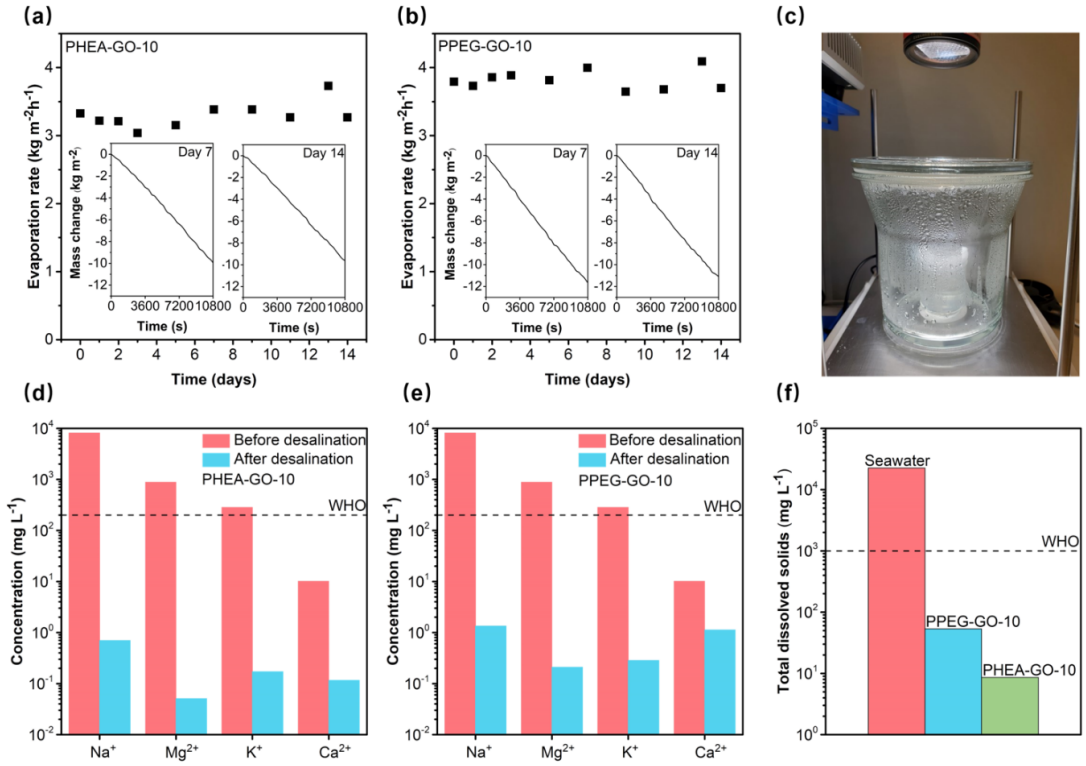

Figure 5.9 Desalination performance of the cryogels. Evaporation rates of (a) PHEA-GO-10 and (b) PPEG-GO-10 immersed in real seawater for half a month. Insets: ISSG performance after seven and fourteen days of exposure to seawater. (c) The setup for desalination and condensed water collection. Four major ions concentrations measured in real seawater both before and after solar desalination via (d) PHEA-GO-10 and (e) PPEG-GO-10. (f) Total dissolved solids of the seawater and the desalinated water of PPEG-GO-10 and PHEA-GO-10.

With promising cryogel ISSGs in hand, we then explored their desalination performance in practical applications. We have repeatedly tested the evaporation performance of PHEA-GO-10 (Figure 5.9a) and PPEG-GO-10 (Figure 5.9b) using seawater (Darling Harbour, Sydney, Australia; E151.20°, S33.87°). We conducted three-hours continuous seawater solar steam generation test every day. During fourteen repeats, both PHEA-GO-10 and PPEG-GO-10 ISSGs presented stable evaporation rates around 3.3 kg m^{-2} h^{-1} and

3.6 kg m^{-2} h^{-1} respectively under one sun irradiation. After each desalination process, no significant salt accumulation was observed on the surfaces of the ISSG gels, suggesting good salt resistance. This might arise from the high water content and rapid water replenishment of cryogel networks, which could hinder the rapid concentration reduction at the evaporation surface and the super-saturation of salt solutions (Loo et al., 2021). To collect the condensed water, the ISSGs were placed in a sealed jar with glass cover and the condensed water at the bottom as well as on the wall of the container was collected for further analysis (Figure 5.9c). The ICP-MS measurements were performed to determine the salt concentrations of the seawater and the collected water, and the results were shown in Figures 5.9d-5.9e. We found that the concentrations of the primary ions (Na^+, Mg^{2+}, K^+ and Ca^{2+}) in the seawater were significantly reduced by 2-5 orders of magnitude after ISSG-based desalination process. The seawater we used has a TDS of 22,500 mg L^{-1}, and the TDS of the condensed water was 8.59 mg L^{-1} and 53.2 mg L^{-1} for PHEA-GO-10 and PPEG-GO-10 ISSGs (Figure 5.9f). Notably, the salt concentrations in the produced water are lower than the WHO drinking water standards (Organization, 2009a, 2009b; WHO & Geneva, 2011). In all, the cryogel ISSGs exhibit high salt resistance and highly stable performance in long-time solar desalination process.

5.4 Conclusion

In this study, we developed novel cryogel-based ISSG materials via facile freeze-thaw method for solar driven desalination applications, and fairly compared their properties

and performance with conventional hydrogel-based ISSG systems. We found that the key for successful constructing macroporous water channels in cryogels is the selection of polymer precursors with T_gs below the freezing temperatures. In addition, the chemical structures of different hydrophilic groups also play an important role in promoting the IW water generation, thereby reducing the overall evaporation enthalpy. The resultant PHEA- and PPEG-based ISSGs show rapid water replenishment ability and possess high intermediate water content, achieving easier water evaporation compared to conventional hydrogels. The cryogel ISSGs also display excellent durability and desalination competence, which makes them promising for future practical desalination applications.

CHAPTER 6
Scale Up Hydrogel Fabrication via 3D Printing

This chapter has been derived from the accepted paper of **Mao, S.**, Zhang, S., Shi, Y., Feng, A., Onggowarsito, C., Xu, X., Aditya, L., Sun, Y., Nghiem, L. D., & Fu, Q. (2024). Precision-Engineered, Polymer-Lean, Digital Light Processing 3D-printed Hydrogels for Enhancing Solar Steam Generation and Sustainable Water Treatment [10.1039/D5MH00018A]. *Materials Horizons*.

With effective pore structures identified as a key enabler for water transport, the next step is to scale up fabrication using advanced manufacturing methods. This chapter introduces a DLP-based 3D printing strategy designed to overcome the limitations of traditional printing inks, which tend to produce overly dense hydrogels. By formulating a low-polymer-concentration ink, the resulting printed hydrogels maintain high porosity, water uptake, and mechanical strength—laying the foundation for scalable, high-performance solar steam generators.

6.1 Introduction

Water scarcity is a pressing global challenge that has drawn growing concern. In recent decades, the problem has intensified due to factors such as climate change, water pollution, rapid population growth, and industrial expansion (Chakkaravarthy, 2019; Immerzeel et al., 2010). According to the Massachusetts Institute of Technology's MIT Integrated Global System Model Water Resource System, approximately 52% of the global population is projected to live in water-stressed regions by 2050 (Schlosser et al., 2014). This increasing water scarcity is likely to escalate conflicts over resources, raise the risk of food insecurity and crop failures, and pose a significant threat to global peace and public health ((FAO), 2012; UNESCO & UN-Water, 2024). Therefore, to address this challenge, it is essential to develop high-yield, energy-efficient, and cost-effective technologies for seawater desalination and wastewater treatment (AlMarzooqi et al., 2014; Khawaji et al., 2008; Panagopoulos et al., 2019; Semiat, 2008; Shannon et al., 2008).

Hydrogel-based ISSG is an emerging technique that leverages sunlight to evaporate seawater or wastewater at the hydrogel interface, offering advantages such as zero additional energy consumption and rapid freshwater production (Deng et al., 2017; Ma et al., 2017; Mao et al., 2022; Neumann et al., 2013; Onggowarsito et al., 2024; Shi et al., 2024; Xu et al., 2020; Zhao et al., 2018; Zhou, Guo, et al., 2019; Zhou et al., 2018; Zhu et al., 2021). However, despite significant advancements in hydrogel design, current research predominantly focuses on small-scale hydrogels fabricated using molds for laboratory experiments. While these hydrogels can achieve high evaporation rates, their limited size restricts their ability to generate sufficient steam for practical applications. Moreover, scaling up hydrogel fabrication presents challenges, including limited mold flexibility and inconsistencies in properties within larger hydrogels. To address these issues and enable the practical implementation of ISSG, it is crucial to explore industrial-scale manufacturing techniques, such as 3D printing, to produce hydrogels specifically tailored for ISSG applications.

The emergence of 3D printing technologies, such as DIW and DLP, offers more versatile and scalable approaches for hydrogel fabrication. Among these, DIW enables the extrusion-based construction of hydrogels but often struggles with precise control over internal structures and lacks the high-resolution printing capabilities required for intricate designs (Huang et al., 2024; Li et al., 2023; Liu et al., 2023; Yuan et al., 2021; S. Zhang et al., 2024). DLP 3D printing represents an Additive Manufacturing technique capable of rapidly fabricating hydrogels through a layer-by-layer photopolymerization process.

Several research groups have investigated its application for producing hydrogels with intricate architectures for ISSG (Chaule et al., 2021; Liu & Zheng, 2024; Sun et al., 2023; Wang et al., 2022; Wu et al., 2020; Xiao et al., 2024; Yang et al., 2024; Zhang et al., 2023; Zheng et al., 2023; M. Zou et al., 2021). However, the printing inks developed in these studies exhibit a high content of precursors, reaching up to 90 wt%, which contributes to reduced hydrogel swelling ratio, slower water transport, and diminished evaporation rates in the resulting 3D printed hydrogels (Guo et al., 2021; Y. Guo, H. Lu, et al., 2020; Guo, Zhao, et al., 2019; Mao, Feng, et al., 2023; Mao, Onggowarsito, et al., 2023; Zhou et al., 2018). This phenomenon occurs because, under the 405 nm near-UV light conditions used in commercial DLP 3D printers, a lower precursor concentration results in the formation of fewer long chains through polymerization within a given exposure time. With limited entanglement between the chains, the printed part is less cured and more susceptible to the ink during the printing process (Dhand. et al., 2024). On the other hand, even though some gel materials can be printed in several layers at low precursor concentrations, repeated soaking of the printed parts in the ink can lead to excessive swelling and severe deformation (Hisham et al., 2022), disrupting the continuity of the 3D printed structures. Some attempts have been made, including ionic locking (Sun et al., 2023), directional freezing (Yang et al., 2024), and post-treatment methods; however, these approaches tend to increase both the manufacturing cycle time and costs. From a materials perspective, we see this as an opportunity to develop a novel DLP 3D printing ink that is better suited for 3D printing hydrogels for ISSG applications.

Herein, we report a viable printing ink formulation with a precursor loading of only 20 wt% for the DLP 3D printing of high water-content hydrogels for efficient ISSG-based desalination and water treatment. The optimal printing ink consists of 5 wt% long chain polyvinyl alcohol, 15 wt% monomer, and a small amount of cross-linker. Upon UV-induced crosslinking in the DLP 3D printer, this formulation forms a semi-interpenetrating polymer network. Following a straightforward freeze-drying process, the 3D-printed hydrogel produced with this formulation exhibits an increased porosity, excellent water hydration capacity, and an impressive water evaporation rate of 3.56 kg m^{-2} h^{-1} in DI water under one-sun irradiation (1 kW m^{-2}). These attributes demonstrate its potential as a scalable method for hydrogel fabrication in ISSG applications.

6.2 Experimental Section

6.2.1 Chemicals

All the chemicals, including HEA (96 wt% in DI water), PVA (MW = 89000-98000 g mol^{-1}), PEGDA (average M_n = 575 g mol^{-1}), LAP, GO (powder, 15-20 nanosheets, 4-10% edge-oxidized), GA solution (25 wt% in DI water), HCl (32 wt% in DI water) were purchased from Sigma-Aldrich Australia and used directly without any further purification.

6.2.2 Development of 3D Printing Inks

The printing ink of 5PVA15PHEA was chosen as a sample to present the detailed

preparation process. 10 g PVA powder was dissolved in 100 mL DI water at 90 ºC for 5 hours to get a 10 wt% PVA solution. 100 mg GO powder was evenly dispersed in 100 mL DI water via sonication for 2 hours to afford a 1 mg mL^{-1} GO solution. 15 mL PVA solution and 15 mL GO solution were mixed together in a light-proof container, then 4.5 g HEA, 67.5 mg PEGDA and 60 mg LAP were added. The mixture is stirred for 5 minutes at 2000 rpm to obtain the 3D printing ink, denoted as 5PVA15PHEA. Compared to the 5PVA15PHEA printing ink, 10PVA15PHEA contains double the amount of PVA, while an additional 1.5 g of HEA and 22.5 mg of PEGDA are added to 5PVA20PHEA.

6.2.3 3D Printing of Hydrogels

Targeted 3D structure was designed by Pro/ENGINEER software and saved as 'obj' files. After opening the 'obj' file with Anycubic Photon Workshop 3D Slicer Software, the following printing parameters were set: the z-axis moving rate was 1 mm s^{-1}, the layer thickness was 50 μm, and each layer's normal exposure time was 25 s. The bottom 10 layers had an exposure time of 30 s. A USB flash drive was used to store the defined slicing 'dl2p' file for 3D printing utilizing a DLP 3D printer (Anycubic Photon D2) with a near-ultraviolet light (λ = 405 nm). The intended printing program was then executed once the prepared photo-responsive ink was poured into the DLP 3D printer's resin tank.

After printing, the remaining ink on the surface of 3D printed objects was cleaned gently with DI water. And then the 3D printed hydrogels were then further cured in a UV curing machine (Anycubic) for 30 minutes to fully cure the uncross-linked components. To

crosslink the PVA chains in the hydrogels, the 3D printed hydrogels was submerged in solution containing 0.75 wt% GA and 0.16 wt% HCl for 30 minutes, and then the process was repeated twice. After washing the hydrogels again with DI water to remove all the residuals. The resultant 3D printed hydrogels were frozen at -18 ºC overnight and freeze-dried prior to characterization. Additionally, they were all thoroughly saturated in DI water piror to the solar steam generation test.

6.2.4 Characterizations

The viscosity of the 3d printing ink was confirmed by a Brookfield DV2T viscometer at a constant temperature of 25 ºC using a spindle SC4-29. The spindle speed was controlled at 120 rpm. The printed structure and pore structure of the hydrogels were investigated using a Zeiss scanning electron microscope (SEM) at an operating voltage of 10–30 kV. FT-IR spectra were acquired with a Shimadzu MIRacle 10 FT-IR system. UV-vis-NIR absorption spectra, covering the wavelength range of 300–2500 nm, were recorded using a Perkin Elmber Lambda 950 UV-vis-NIR spectrophotometer. The tensile test of the printed hydrogel was conducted by Shimadzu AGS-X Universal Tester (Max load 10 kN) with a strain rate of 50 mm min^{-1}. The dimensions of the tested samples specimens were length = 100 mm, width = 6 mm, and thickness = 5 mm according to ASTM (E8) subsize standard. Raman spectra were collected via a Renishaw Raman spectrometer. The contact angle test was conducted by an Attension contact angle meter. Thermal changes in the hydrogels, from room temperature to 200 °C, were monitored with a NETZSCH DSC300

Supreme at a heating rate of 5 °C min^{-1}.

6.2.5 Interfacial Solar Steam Generation Tests

A solar simulator (NBeT HSX-F3000 xenon light source) was used to simulate solar radiation. With the aid of a thermal power sensor and a portable power and energy meter (PM100D and S405C, Thorlabs, Germany), the solar irradiance on the hydrogel surface was calibrated to one sun (1 kW m^{-2}). The test 3D printed hydrogels were placed on the surface of a floating EPS foam atop a beaker filled with DI water, seawater, or a 20 wt% NaCl solution. Several tissues passing through a central hole of the EPS foam were used to supply water to the bottom of the testing hydrogels. Using an electronic mass balance (OHAUS Pioneer IC-PX 124), water mass loss was tracked over time during SSG tests. An EPE foam layer was placed between the balance and the beaker to stop heat transfer. By using linear fitting to calculate the slopes of the mass loss curve over time, the evaporation rates were ascertained. Using a Fluke PTi120 pocket thermal imager, the temperatures of both the bulk water and the hydrogel surface were measured every five minutes during the test.

6.3 Results and Discussion

6.3.1 The Development of 3D Printing Ink

In this study, we utilized a bottom-up DLP printer (Figure 6.1a) to produce 3D printed hydrogels with a variety of structures, where a 405 nm near-UV light source was

positioned beneath the ink tank for curing the precursors layer-by-layer from the bottom up on the printing platform. In order to develop DLP printing inks suitable for printing ISSG hydrogels, we screened various combinations of initiators, monomers and crosslinkers. However, we encountered several challenges and did not achieve satisfactory printing results (Table 6.1). For instance, we tried to prepare printing ink containing monomer AM and cross-linker MBA. However, we observed that the printed hydrogel parts swelled excessively during repeated immersions into the ink and then detached from the printing platform midway through the print run. Although printing can be achieved using a formulation based on poly(ethylene glycol) methyl ether acrylate (PEGMA, M_n = 480 g mol^{-1}) and PEGDA (M_n = 575 g mol^{-1}), the resulting hydrogels exhibit insufficient mechanical strength and are prone to cracking under the swelling force of water, rendering them unsuitable for ISSG applications.

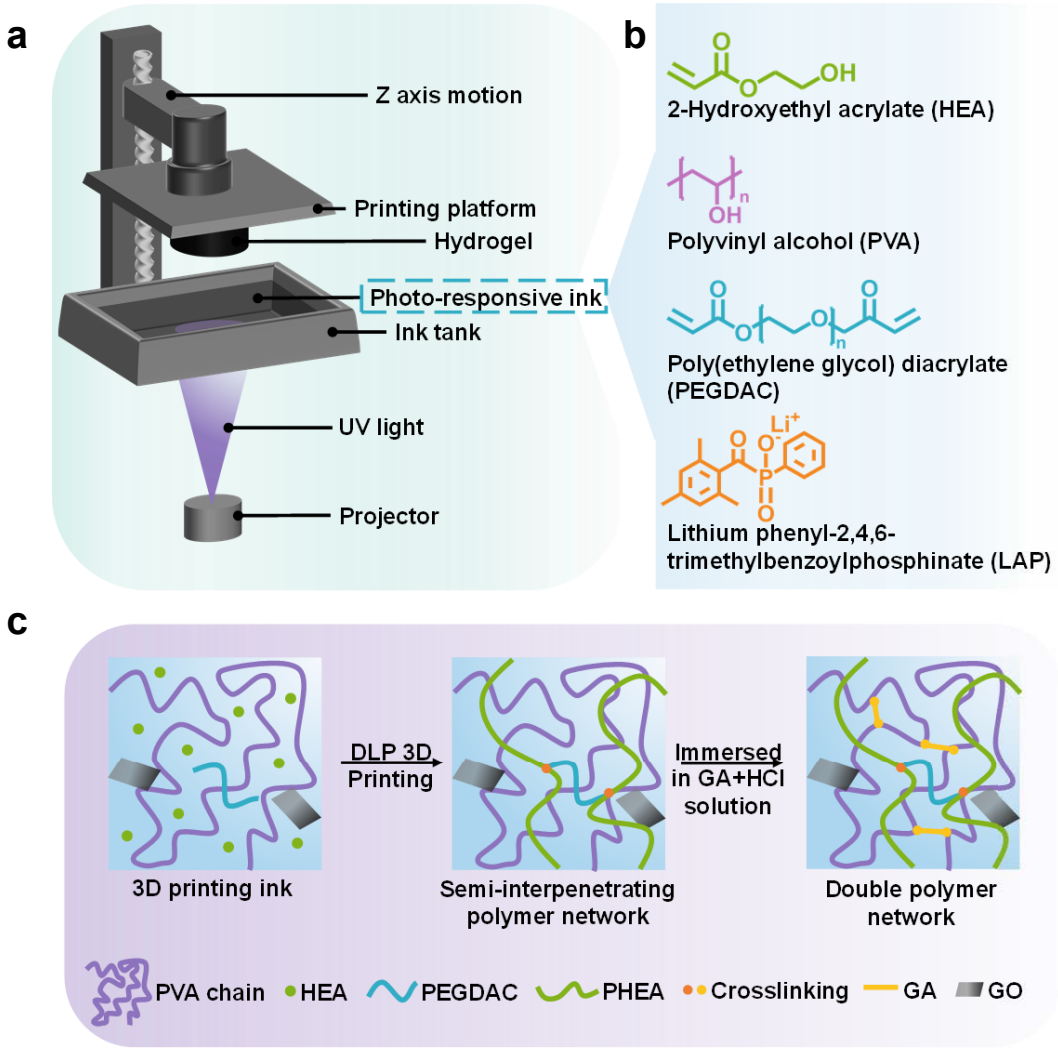

Figure 6.1 (a) Schematic illustration of the bottom-up DLP 3D printing method, (b) the chemical structures of the constituents in the printing ink, and (c) the evolution of the polymer network throughout the UV-induced radical polymerization and post-treatment.

Table 6.1 The development of 3D printing ink for DLP. The concentration of GO is the same in all formulations (0.5 mg mL^{-1}).

Monomer	Crosslinker	Photo-initiator	Solvent and additives	Comments
8.75 g PEGDA (M_n = 575 g mol^{-1})		4 g 2,4,6-trimethyl benzoyld iphenyl phosphin	15.25 g Ethanol	Printing was possible, but cracked when contacting water due to differences in solvent surface tension, not

		e oxide (TPO)		suitable for long-time SSG application.
10 g PEGDA (M_n = 575 g mol^{-1})		75 mg LAP	30 mL Water	Printing was possible, but hard to print fine structures.
7.34 g AM	111.4 mg MBA	75 mg LAP	30 mL Water	Printing failed. Hydrogel swelling during the printing caused wrinkling and detachment from the printing platform.
9.79 g AM	148.5 mg MBA	75 mg LAP	30 mL 5 wt% PVA aqueous solution	Printing failed. The hydrogel is too sticky, leading to failure in separating from the release film.
7.5 g Poly(ethylene glycol) dimethacrylate (Mn = 550 g mol^{-1})		75 mg LAP	30 mL Water	Printing was possible, but has a weak affinity with GO, resulting in a white printed hydrogel.
10 g Poly(ethylene glycol) methyl ether methacrylate (M_n=500 g mol^{-1})	100 mg PEGDA (M_n = 575 g mol^{-1})	75 mg LAP	30 mL Water	Printing failed. Took more than 2 minutes to crosslink one layer.
10 g PEGMA (M_n = 480 g mol^{-1})	150 mg MBA or PEGDA (M_n = 575 g mol^{-1})	75 mg LAP	30 mL Water	Printing successfully, but easily to break after swelling in water.
10.0 g PEGMA (M_n = 480 g mol^{-1}) and 2.5 g AM	125.0 mg MBA	75 mg LAP	30 m L Water	Printing successfully, but too soft, not suitable for long-time SSG application.
16.974 g N-Isopropylacrylamide and 1.81 g AM	30 mg PEGDA (M_n = 575 g mol^{-1})	75 mg LAP	30 mL Water	Printing failed.
5 g Poly(ethylene glycol) dimethacrylate (Mn = 550 g mol^{-1}), 2.5 g PEGMA (M_n = 480 g mol^{-1}), and 2.5 g AM		100 mg LAP	40 mL Water	Printing successfully, but fragile.
5.94 g Diacetone	60 mg PEGDA (M_n =	60 mg	24 mL	Printing failed. The

acrylamide	575 g mol^{-1})	LAP	Water	hydrogel is too sticky, leading to failure in separating from the release film. And has a weak affinity with GO, resulting in a white printed hydrogel.

After a dozen of unsuccessful attempts to maintain the total precursor content below 25 wt%, we ultimately succeeded in formulating an appropriate ink for DLP 3D printing. As shown in Figure 6.1b, this ink with a viscosity of 6.67 mPa·s consists of HEA monomer, a small amount of long-chain PVA, trace amounts of a cross-linker (PEGDA), a photoinitiator (LAP), and GO as a PTM. Water-based inks are more cost-effective and environmentally friendly than ethanol-based inks. Additionally, the use of aqueous inks helps prevent the printed hydrogel from breaking due to difference in solvent tension during the water-ethanol exchange. Long-chain PVA was added to enhance the formation of effective physical entanglement, and thus facilitate UV-curing to ensure the fidelity of the printed layer. GO has an excellent light-absorbing ability throughout the solar spectrum, and was chosen as a photothermal material in this study because the surface functional groups (i.e. –OH, –COOH, –C–O–C–) can form hydrogen bonding with the polymer chains to increase its dispersity in the matrix and act as fillers to enhance the enhance the mechanical properties of the 3D printed hydrogel. Moreover, the dispersed GO can be better exposed to sunlight with the help of its unique 2D geometry, which promotes the photothermal conversion (X. S. Zhang et al., 2024). Instead of using post-treatment to incorporate photothermal materials into the 3D-printed hydrogels, directly

adding GO to the printing formulation introduced several challenges. Certain cross-linker, such as PEGDMA (M_n = 550 g mol^{-1}), exhibited weak affinity with GO, resulting in printed hydrogels appearing white, indicating limited GO incorporation. Additionally, the GO concentration needed to remain low to prevent excessive UV light absorption, which could interfere with LAP activation. As shown in previous study (Liu & Zheng, 2024), a higher concentration of oxidized carbon black was used, necessitating a significant increase in photo-initiator usage for compensation, which also raised the overall cost. We meticulously regulated our GO concentration to 0.5 mg mL^{-1} in all formulations to reduce the cost as well as maintain the light adsorption.

As illustrated in Figure 6.1c, prior to 3D printing, the randomly tangled PVA chains were uniformly mixed with other components in the ink tank. Upon UV irradiation of a 50 μm thick layer with a programmed pattern, LAP in this area absorbed photons and transitioned to an excited singlet state, leading to the formation of two primary radicals: a benzoyl radical ($C_6H_5C(O)\cdot$) and a phosphorus-centered radical. The benzoyl radical generated could initiate the radical polymerization of HEA and PEGDA by attacking their double bonds, thereby creating new reactive sites that propagate the chain reaction. This propagation continued until two active radical chain ended encounter each other or interacted with a radical quencher, resulting in a termination reaction. Most of these reactions could be completed within 25 seconds of UV exposure for each layer. The long PVA chains subsequently intertwined with the formed PHEA chains, resulting in a semi-interpenetrating polymer network. Following 3D printing, the obtained hydrogels were

subjected to post-treatment involving additional UV irradiation and immersion in a GA solution containing HCl to lock the PVA chains within the 3D printed hydrogels.

6.3.2 3D Printed Hydrogels' Chemical Structure and Morphology

All hydrogels were fabricated in a cylindrical structure shown in Figure 6.2a (i) with a diameter of 2.5 cm and a height of 1 cm, incorporating an array of concaves on the surface. Each concave measured 2 mm in diameter, 4 mm in depth, and was spaced 2 mm apart from adjacent concaves. The resulting hydrogels are denoted as xPVAyPHEA-C, where x and y represent the weight concentration of the corresponding precursor, and C stands for the concave arrays on the hydrogel surface.

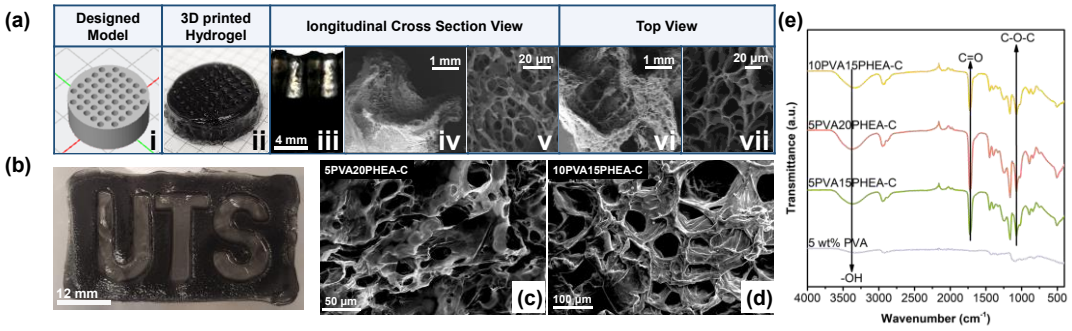

Figure 6.2 Morphology and chemical structure of the 3D printed hydrogels. For the 3D printed 5PVA15PHEA-C: (i) designed 3D model, (ii) physical image, (iii) longitudinal cross section optical image, (iv) longitudinal cross-sectional SEM image, (v) the zoom-in cross-sectional SEM image, (vi) top view SEM image, and (vii) the zoom-in top view SEM image. (b) Physical image of a 3D pattern (with a total height of 4 mm and 2 mm depth of "UTS" patterns). The cross-section SEM images of the pore structure in the concave 3D printed hydrogel of (c) 5PVA20PHEA-C and (d) 10PVA15PHEA-C, respectively. (e) FT-IR spectra of the 5PVA15PHEA-C, 5PVA20PHEA-C, and 10PVA15PHEA-C hydrogels. The control sample is a pristine 5 wt% PVA hydrogel directly crosslinked with GA.

From Figures 6.2a (i and ii), it is evident that the 3D-printed SSG hydrogels exhibit high fidelity, and even after freeze-drying, they effectively retain the intended morphology. We

further characterized their longitudinal slices, where half-pass (Figure 6.2a-iii) channel structures, can be clearly observed. All these images show that the 3D printed hydrogels exhibit a uniform black color, which indicates that the GO nanosheets are uniformly distributed, thus ensuring efficient photothermal conversion. SEM imaging after freeze-drying further revealed the concave structure of the gels, with a homogeneous pore structure clearly visible on the inner and outer surfaces of the concave pore walls (Figures 6.2a iv-vii). Using the printing ink, we also printed other 3D objects with a favorable model fidelity (Figure 6.2b). At higher precursor concentration loadings, fewer pores were formed, and the internal pores tended to be more disordered. This resulted in thicker pore walls and lower porosity, which hinder water transport and affect the interactions between the polymer chains and water. These SEM images (Figures 6.2c and 6.2d) show a cross-sectional view highlighting a region where more pores can be observed. These results confirm the successful 3D printing of hydrogels with macro/micro-engineered structures and high porosity using a water-based, cost-effective ink with low precursor concentration.

FT-IR spectroscopy analysis confirmed the successful preparation of the ISSG hydrogels through DLP 3D printing (Figure 6.2e). All hydrogels displayed a characteristic absorption peak around 3,315 cm^{-1}, which is attributed to the stretching vibrations of the hydroxyl groups (-OH). Notably, the printed hydrogels exhibited a stronger signal compared to that of the pristine PVA hydrogel, a result of the enhanced O-H vibrations from PHEA. Additionally, distinct peaks at 1,724 cm^{-1} and 1,070 cm^{-1} were associated

with the vibrations of the C=O groups of PHEA and C-O-C groups of GO, respectively.

6.3.3 3D Printed Hydrogels' Mechanical Strength, Hydrophilicity and Light adsorption

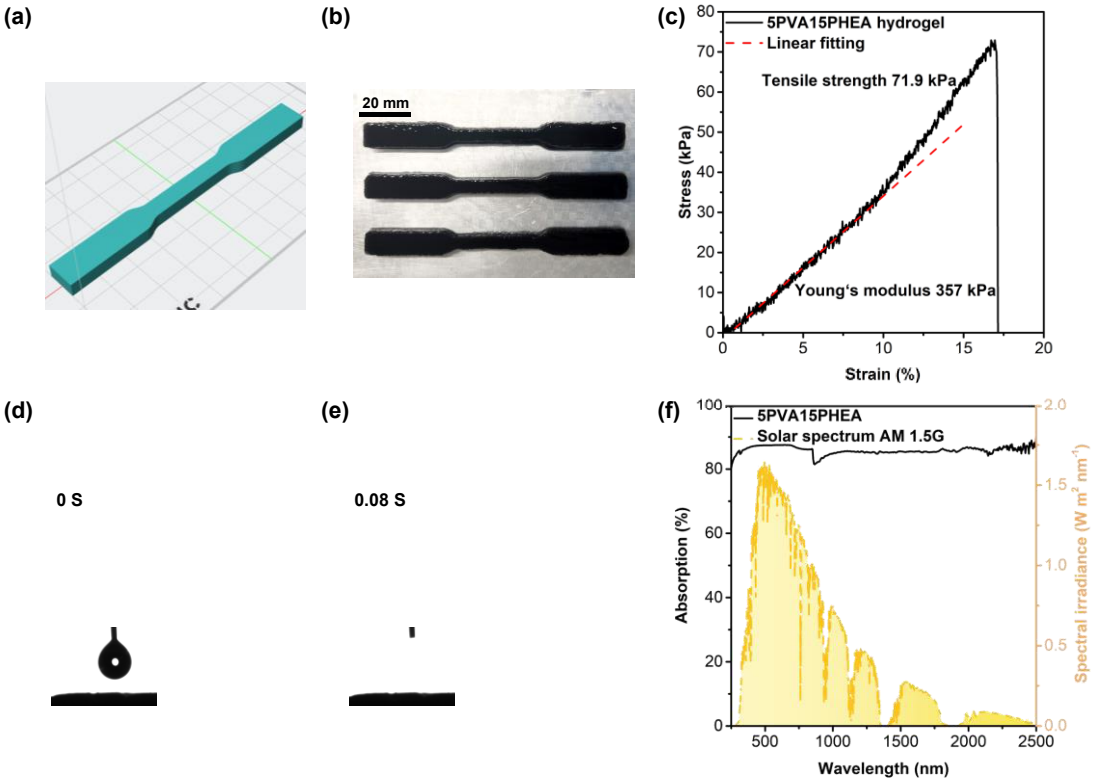

Figure 6.3 (a) The 3D model of ASTM (E8) subsize standard hydrogel specimen for tensile test, and (b) the 3D printed hydrogels from the model. (c) Stress-strain curve of the printed 5PVA15PHEA hydrogel in the tensile test. The contact angle test of 3D printed 5PVA15PHEA hydrogel at (d) 0 s and (e) 0.08 s. (f) UV-vis-NIR adsorption spectrum of the 3D printed 5PVA15PHEA hydrogel and the air mass 1.5 global (AM 1.5 G) solar spectrum with normalized spectral solar irradiance density (the light-yellow region) in the wavelength range from 300 to 2,500 nm.

We 3D printed ASTM (E8) subsize standard hydrogel specimens (Figures 6.3a and 6.3b) for tensile testing with the formulation of 5PVA15PHEA. The stress-strain curve presented in Figure 6.3c indicates that the printed hydrogel exhibits a tensile strength of 71.9 kPa and a Young's modulus of 357 kPa. These findings demonstrate that the printed

hydrogels remain rigidity even at low precursor concentrations, attributable to the incorporation of PVA and GO. This combination enhances the mechanical properties by promoting effective chain entanglements and facilitating H-bonding within the matrix. A minimal concentration of GO at 0.25 wt% to create a hydrogel that demonstrates a broad spectrum of light absorption across the entire solar range, from 300 nm to 2,500 nm, achieving an absorption rate exceeding 80% (Figure 6.3f). The contact angle test depicted in Figures 6.3d and 6.3e demonstrates that the porous structure of the printed hydrogel, combined with its abundant hydrophilic groups, allows for rapid water absorption within 80 ms. These hydrogels exhibit broad light absorption, high mechanical performance, and super-hydrophilicity, making them well-suited for ISSG applications.

6.3.4 Water Interaction within the 3D Printed Hydrogels

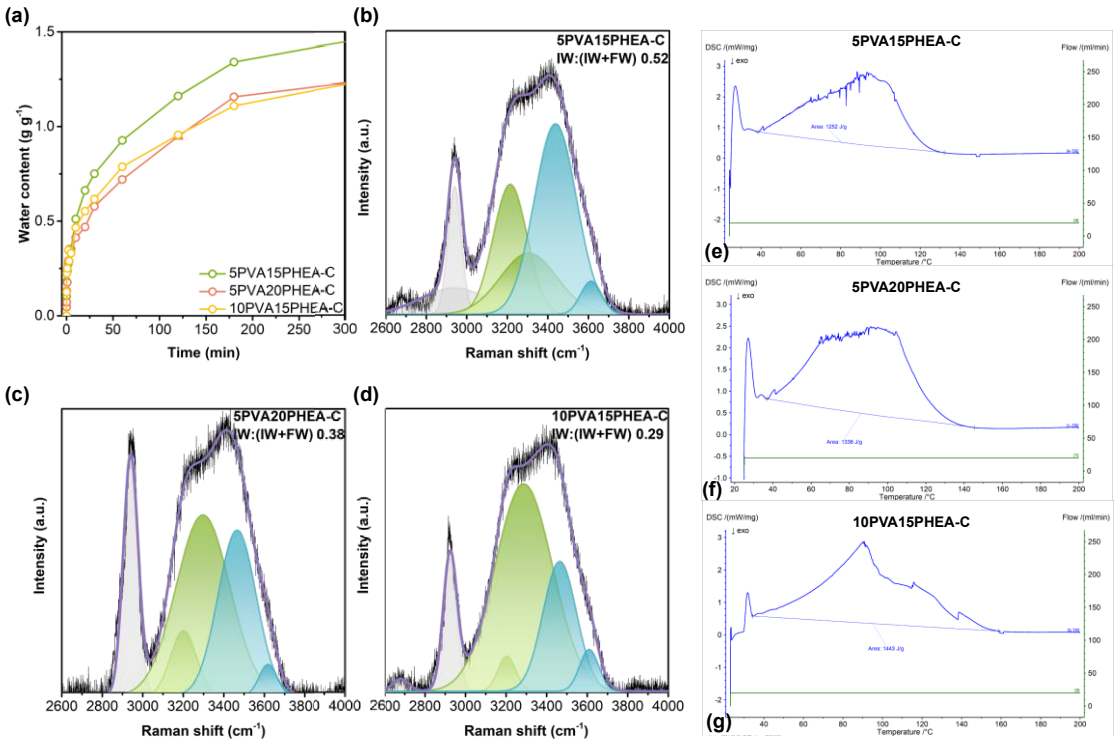

Figure 6.4 (a) The water content vs absorption time of 3D printed hydrogels. The unit is measured gram of water per gram of dry gel. Fitting curves for the (b) 5PVA15PHEA-C, (c) 5PVA20PHEA-C, and (d) 10PVA15PHEA-C hydrogels in the Raman spectra within the O-H stretching energy region. Free water is indicated by the green peaks, whereas intermediate water by blue peaks. Raw DSC curves and the equivalent water vaporization enthalpies calculated from the integrated area of (e) 5PVA15PHEA-C, (f) 5PVA20PHEA-C, and (g) 10PVA15PHEA-C hydrogels, respectively.

Water uptake capacity of these 3D-printed hydrogels, each with a distinct precursor composition, was evaluated by immersing the dried gels in deionized water (Figure 6.4a). Among the samples, 5PVA15PHEA-C exhibited the fastest water transport rate due to its high porosity resulting from the lowest precursor concentration. In contrast, 5PVA20PHEA-C and 10PVA15PHEA-C demonstrated slower water uptake and lower swelling ratios, attributed to their disordered, thicker pore walls and reduced porosity.

The presence of intermediate water (Guo, Zhou, et al., 2019; Lei et al., 2022; Zhou, Zhao, et al., 2019a) is often applied to explain why the water absorbed in hydrogels evaporates more readily than bulk water. IW refers to water molecules characterized by weaker or partially formed hydrogen bonds, positioned between those directly that are directly associated with polymer chains (*aka.* BW) and those that do not interact with the polymer chains (*aka.* FW). Due to the weaker bonding, IW molecules exhibit a greater tendency to dissociate from neighboring molecules. The IW content can be quantified by Raman measurements. For this study, Raman measurements were performed on all 3D-printed hydrogels that had been fully saturated with DI water, and peak fitting was used to calculate the IW contents of each sample (Figures 6.4b-6.4d). The presence of IW molecules, characterized by weaker or partially formed hydrogen bonds, is indicated by

the blue peaks at approximately 3,514 cm^{-1} and 3,630 cm^{-1}. In contrast, the green peaks at 3,233 cm^{-1} and 3,401 cm^{-1} correspond to FW with fully formed hydrogen bonds (Zhao et al., 2018; Zhou et al., 2018). The IW content is typically assessed through the ratio of IW to the sum of IW and FW, expressed as [IW:(IW+FW)], calculated from the integrated areas under the fitting spectral peaks. 5PVA15PHEA-C, with a 20 wt% precursor concentration, exhibited the highest IW content of 0.52, showing the highest potential for ISSG. In contrast, 5PVA20PHEA-C and 10PVA15PHEA-C, formulated with higher precursor concentrations, showed lower IW content, likely due to reduced porosity, which limits the interaction between hydrophilic groups and water molecules.

DSC is used to measure the vaporization energy of water in the printed hydrogels, demonstrating the reduction in water's evaporation enthalpy within these hydrogels. Figures 6.4e-6.4g show the change of heat flow signal as a function of temperature, and the equivalent water vaporization enthalpies can be calculated from the integrated area. Increased IW content lowers the equivalent enthalpy, and 5PVA15PHEA-C showed the lowest equivalent enthalpy of 1,252 J g^{-1}.

The superior water transport capability, highest IW content, and lowest equivalent water vaporization enthalpy of 5PVA15PHEA-C, printed with 20 wt% precursors, highlight its potential for effective ISSG applications.

6.3.5 ISSG Tests

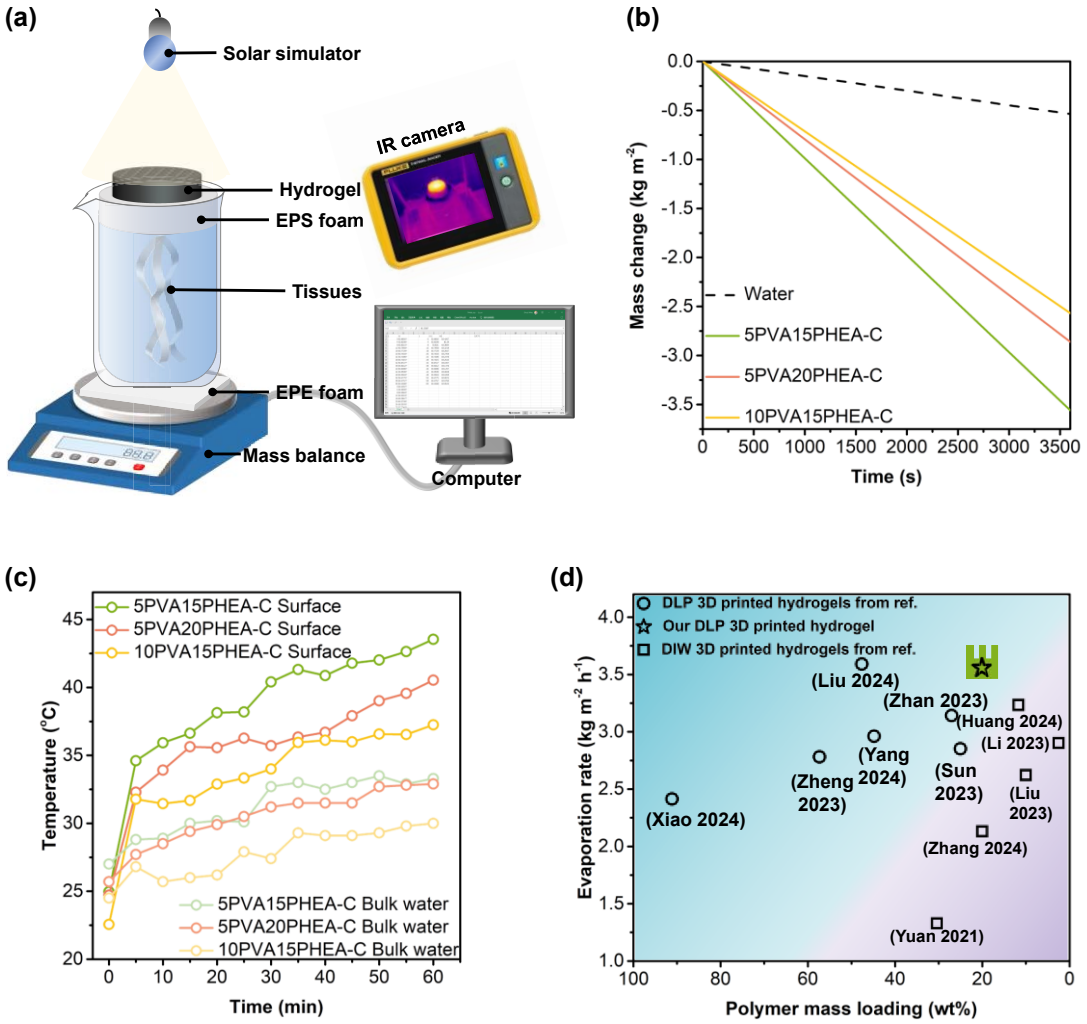

Figure 6.5 The ISSG performance of the printed hydrogels. (a) A home-made set up for the SSG test. (b) Water mass changes under one sun irritation condition for 5PVA15PHEA-C, 5PVA20PHEA-C, and 10PVA15PHEA-C hydrogels, respectively (in DI water). (c) The temperature variations of the 5PVA15PHEA-C, 5PVA20PHEA-C, and 10PVA15PHEA-C hydrogel surfaces and bulk water during the SSG test under one sun irritation. (d) Comparison of the evaporation rates and precursor concentrations to state-of-the-art DLP (Liu & Zheng, 2024; Sun et al., 2023; Xiao et al., 2024; Yang et al., 2024; Zhan et al., 2023; Zheng et al., 2023) and DIW (Huang et al., 2024; Li et al., 2023; Liu et al., 2023; Yuan et al., 2021; S. Zhang et al., 2024) 3D-printed ISSGs (typical three-dimensional ISSGs were not included). Detailed data are listed in Tables 6.2 and 6.3.

We then assessed the solar driven evaporation rates of the 3D-printed hydrogels under standard laboratory conditions (24 ºC and one atmospheric pressure) (Figure 6.5a). To

minimize the influence of external disturbances, the entire water surface in a container was covered with a layer of EPS sheet. To prevent heat from transferring to the balance, a thick layer of EPE foam was laid underneath the container. We tracked the changes in mass of bulk water containing hydrogels over three hours of solar irradiation (Figure 6.5b), and calculated mass loss over time by determining the slope from a linear fit. All 3D-printed hydrogels demonstrated significantly higher steam generation rates than that of water evaporation under static conditions. As expected, among the 3D-printed hydrogels with different precursors content, 5PVA15PHEA-C managed to achieve the highest evaporation rate of 3.56 kg m^{-2} h^{-1}, followed by 5PVA20PHEA-C with a rate of 2.86 kg m^{-2} h^{-1}, while 10PVA15PHEA-C had the lowest evaporation rate at 2.57 kg m^{-2} h^{-1}. Thermal photographs were taken during the ISSG process using a handheld infrared camera to record the temperatures of the bulk water and the evaporation surfaces (Figure 6.5c). Within initial 5 minutes, the surface temperatures of all hydrogels increased rapidly, and then continued to rise to a stabilized temperature. This result can be attributed to the surface patterning of these hydrogels, which enhances light absorption and promotes the temperature increase.

Table 6.2 Evaporation rates and polymer mass loading of the DLP 3D printed hydrogels from previous work.

Ref.	Hydrogel	Polymer mass loading wt%	Evaporation rate kg m^{-2} h^{-1}
(Zheng et al., 2023)	PEGDA based hydrogel	57.3	2.78
(Sun et al., 2023)	Poly(N-Isopropyl acrylamide) based hydrogel	25.0	2.85

(Yang et al., 2024)	PAM-PVA based hydrogel	44.8	2.96
(Liu & Zheng, 2024)	Poly(N-Isopropyl acrylamide) based hydrogel	47.6	3.59
(Zhan et al., 2023)	PAM based hydrogel	27.0	3.14
(Xiao et al., 2024)	PEGDA based hydrogel	91.0	2.41
This work	**PHEA-PVA based hydrogel**	**20.0**	**3.56**

Table 6.3 Evaporation rates and polymer mass loading of the DIW 3D printed hydrogels from previous work.

Ref.	Hydrogel	Polymer mass loading wt%	Evaporation rate kg m^{-2} h^{-1}
(Yuan et al., 2021)	Cellulose-sodium alginate based hydrogel	30.4	1.33
(Huang et al., 2024)	PVA-sodium alginate based hydrogel	11.7	3.23
(S. Zhang et al., 2024)	Corn starch based hydrogel	20.0	2.13
(Li et al., 2023)	Bacterial cellulose-sodium alginate based hydrogel	2.5	2.90
(Liu et al., 2023)	Polyacrylonitrile based hydrogel	10.0	2.62
This work	**PHEA-PVA based hydrogel**	**20.0**	**3.56**

The superior evaporation performance of the 3D-printed hydrogel developed in this study arises from the rational design of the ink formulation. The incorporation of long-chain PVA allows for an exceptionally low polymer concentration, resulting in a less dense hydrogel network with enlarged and interconnected pores. This highly porous architecture

not only facilitates rapid water transport but also enhances water–polymer interactions, leading to an increased proportion of IW and a reduced equivalent water evaporation enthalpy. Compared to state-of-the-art DLP 3D-printed ISSG evaporators, the hydrogel presented here achieves a higher evaporation rate while utilizing the lowest precursor concentration. It also outperforms DIW 3D-printed systems, which lack the same level of precision in internal structural control (Figure 6.5d).

6.4 Conclusion

In this work, we developed an innovative DLP 3D printing ink by introducing a small amount of long-chain PVA, which promotes effective physical entanglements to stabilize the photo-crosslinked PHEA network and maintain the integrity of each printed layer. This optimized formulation significantly lowers the precursor concentration, enabling the 3D-printed hydrogel to achieve higher porosity and enhanced water transport properties. The resulting 5PVA15PHEA-C hydrogel features a highly porous structure, excellent mechanical strength, rapid water absorption, and an impressive evaporation rate of 3.56 kg m^{-2} h^{-1}, providing a scalable and cost-effective solution for hydrogel fabrication well-suited for ISSG applications.

CHAPTER 7
Micro/Macrostructure Design for Hydrogel Water and Heat Balance via 3D Printing and Real Outdoor ISSG

This chapter has been derived from the accepted paper of **Mao, S.**, Zhang, S., Shi, Y., Feng, A., Onggowarsito, C., Xu, X., Aditya, L., Sun, Y., Nghiem, L. D., & Fu, Q. (2024). Precision-Engineered, Polymer-Lean, Digital Light Processing 3D-printed Hydrogels for Enhancing Solar Steam Generation and Sustainable Water Treatment [10.1039/D5MH00018A]. *Materials Horizons*.

Building upon the developed 3D printing approach and optimized ink formulation, the final experimental chapter focuses on refining the overall device design by tuning micro-/macro-scale features. This includes tailoring hydrogel geometries to balance water transport and heat localization, as well as integrating the printed structures into a field-deployable outdoor system with condensation capabilities. Through real-world testing, this chapter demonstrates the practical applicability of the developed hydrogel designs in solar water purification.

7.1 Introduction

Water scarcity is an urgent global issue, increasingly exacerbated by climate change, pollution, population growth, and industrialization (Chakkaravarthy, 2019; Immerzeel et al., 2010). Approximately 52% of the global population is projected to reside in water-stressed regions by 2050 (Schlosser et al., 2014). This escalating water scarcity is likely to intensify resource conflicts, contribute to food insecurity, and pose a significant threat to global peace and public health ((FAO), 2012; UNESCO & UN-Water, 2024). Therefore, to address this challenge, it is essential to develop high-yield, energy-efficient, and cost-effective technologies for seawater desalination and wastewater treatment (AlMarzooqi et al., 2014; Khawaji et al., 2008; Panagopoulos et al., 2019; Semiat, 2008; Shannon et al., 2008).

ISSG leveraging hydrogels represents an energy-efficient strategy for freshwater production, providing a sustainable solution to global water scarcity. It utilizes the

plentiful energy from sunlight to induce evaporation of seawater or wastewater at the hydrogel interface, offering benefits such as energy-free operation and efficient freshwater production (Deng et al., 2017; Ma et al., 2017; Mao et al., 2022; Neumann et al., 2013; Onggowarsito et al., 2024; Shi et al., 2024; Xu et al., 2020; Zhao et al., 2018; Zhou, Guo, et al., 2019; Zhou et al., 2018; Zhu et al., 2021). The macro/microstructure of hydrogels is intricately tied to their SSG performance, with specific surface patterns enhancing light capture (Guo, Zhao, et al., 2019; Y. Lu et al., 2021), internal channels improving water transport (Guo et al., 2021; Liang, Zhang, Huang, et al., 2020), and unique shapes resisting fouling (Chen et al., 2020). However, the construction of hydrogels with these advanced structures typically relies on responsive molds, which are time-consuming, labor-intensive, and often inflexible, limiting adaptability to evolving requirements. These challenges highlight the need for innovative manufacturing methods that offer precision, efficiency, and scalability.

DLP 3D printing allows for comprehensive and multidimensional adjustments of hydrogel micro/macrostructures, surpassing the limitations of traditional mold-based methods. Herein, we utilized the high-performance formulation developed in Chapter 6 to 3D print hydrogels with three distinct micro/macrostructures: concave arrays, raised-node arrays, and vertical through-hole arrays on their surfaces. We then investigated the balance between water and heat management in different hydrogels to optimize ISSG performance. Furthermore, the 3D-printed hydrogels demonstrate excellent salt resistance and durability in practical seawater desalination, highlighting their potential for future

applications. By incorporating advanced condenser designs into the real outdoor device, the condensation efficiency was enhanced to 81.4%, resulting in a freshwater productivity of 10.36 L m^{-2} day^{-1} under an average solar flux of 0.47 kW m^{-2} during spring in Sydney.

7.2 Experimental Section

7.2.1 Chemicals

All chemicals used in this chapter were purchased from Sigma-Aldrich Australia and utilized without further purification. These included HEA (96 wt% in DI water), PVA (MW = 89000-98000 g mol^{-1}), PEGDA (average M_n = 575 g mol^{-1}), LAP, GO (powder, 15-20 nanosheets, 4-10% edge-oxidized), GA solution (25 wt% in DI water), HCl (32 wt% in DI water), NaCl, and MB.

7.2.2 Preparation of 3D Printing Ink

10 g PVA powder was dissolved in 100 mL DI water at 90 ºC for 5 hours to get a 10 wt% PVA solution. 100 mg GO powder was evenly dispersed in 100 mL DI water via sonication for 2 hours to afford a 1 mg mL^{-1} GO solution. 15 mL PVA solution and 15 mL GO solution were mixed together in a light-proof container, then 4.5 g HEA, 67.5 mg PEGDA and 60 mg LAP were added. The mixture is stirred for 5 minutes at 2000 rpm to obtain the 3D printing ink, denoted as 5PVA15PHEA.

7.2.3 3D Printing of Hydrogels

Three targeted 3D structures were designed by Pro/ENGINEER software and saved as ‘obj’ files. After opening the ‘obj’ file with Anycubic Photon Workshop 3D Slicer Software, the following printing parameters were set: the z-axis moving rate was 1 mm s^{-1}, the layer thickness was 50 μm, and each layer's normal exposure time was 25 s. The bottom 10 layers had an exposure time of 30 s. A USB flash drive was used to store the defined slicing ‘dl2p’ file for 3D printing utilizing a DLP 3D printer (Anycubic Photon D2) with a near-ultraviolet light (λ = 405 nm). The intended printing program was then executed once the prepared photo-responsive ink was poured into the DLP 3D printer's resin tank.

After printing, the remaining ink on the surface of 3D printed objects was cleaned gently with DI water. And then the 3D printed hydrogels were then further cured in a UV curing machine (Anycubic) for 30 minutes to fully cure the uncross-linked components. To crosslink the PVA chains in the hydrogels, the 3D printed hydrogels was submerged in solution containing 0.75 wt% GA and 0.16 wt% HCl for 30 minutes, and then the process was repeated twice. After washing the hydrogels again with DI water to remove all the residuals. The resultant 3D printed hydrogels were frozen at -18 ºC overnight and freeze-dried prior to characterization. Additionally, they were all thoroughly saturated in DI water, seawater or a 20 wt% NaCl solution piror to the solar steam generation test.

7.2.4 Characterizations

The printed and pore structures of the hydrogels were analyzed using a Zeiss scanning

electron microscope (SEM) operating at 10–30 kV. FT-IR spectra were recorded with a Shimadzu MIRacle 10 FT-IR system, while Raman spectra were collected using a Renishaw Raman spectrometer. Thermal transitions in the hydrogels, ranging from room temperature to 200 °C, were monitored with a NETZSCH DSC300 Supreme at a heating rate of 5 ^{o}C min^{-1}. Ion concentrations in seawater and desalinated water were measured with an Agilent 7900 ICP-MS. Additionally, the presence of MB in water before and after SSG purification was detected using an Agilent Cary 60 UV-Vis spectrometer.

7.2.5 Interfacial Solar Steam Generation Tests

A solar simulator (NBeT HSX-F3000 xenon light source) was utilized to simulate solar radiation, with the solar irradiance on the hydrogel surface calibrated to one sun (1 kW m^{-2}) using a thermal power sensor and a portable power and energy meter (PM100D and S405C, Thorlabs, Germany). The test 3D-printed hydrogels were placed on floating EPS foam positioned atop a beaker containing DI water, seawater, or a 20 wt% NaCl solution. Water was supplied to the bottom of the hydrogels through tissues inserted into a central hole in the EPS foam. Water mass loss during the SSG tests was tracked over time using an electronic mass balance (OHAUS Pioneer IC-PX 124), with an EPE foam layer placed between the balance and the beaker to prevent heat transfer. Evaporation rates were calculated by applying linear fitting to the slopes of the mass loss curve over time. A Fluke PTi120 pocket thermal imager was used to monitor the temperatures of the hydrogel surface and bulk water at five-minute intervals throughout the tests.

7.2.5 Outdoor Experiments

The outdoor solar steam generation test was performed using a home-made evaporation device (Figure 7.1). Specifically, Clear acrylic sheets (thickness: 5 mm) were cut into designed shapes and sticked together with water-proof glue. The assembled device was divided into two separate chambers: a larger evaporation chamber and a smaller condensation chamber. Two 6 cm x 6 cm square fans were embedded in the partition between these two chambers, with the airflow directed from the evaporation chamber toward the condensation chamber. Two TEC1-12706 thermoelectric (TE) modules were embedded at the other end of the condensation chamber, with their cooling sides fully immersed in the condensation chamber, while the heating sides were located outside the device and cooled by a water-cooling system to prevent overheating. The evaporation chamber contained an independent seawater reservoir, where a piece of EPE foam completely covered the seawater, and several tissue strips passed through small holes in the foam to supply water to the hydrogel. The hydrogels, electric fans, and cooling side were positioned on the same horizontal plane to ensure that a larger amount of vapor could be transferred to the condensation chamber and promptly condensed by the cooling side. The independent seawater evaporation chamber could also condense vapor around its perimeter due to the lower temperature of the seawater, making it easier to collect any vapor not transferred to the condensation chamber. The TE module, electric fans, and water-cooling pump were all connected to the output of a Powertech Portable 155W

Power Centre as the charger controller, powered in real-time by a 12V 10W solar panel.

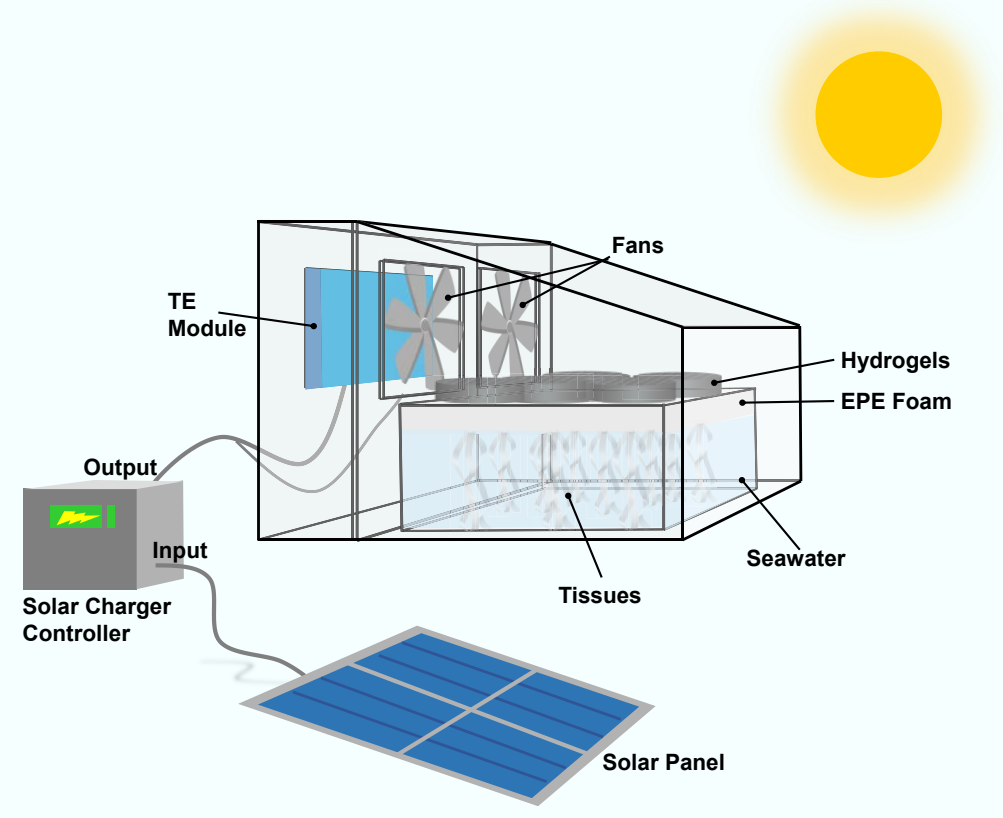

Figure 7.1 Schematic illustration of the custom-designed outdoor SSG device

7.3 Results and Discussion

7.3.1 3D Printed Hydrogels' Chemical Structure and Morphology

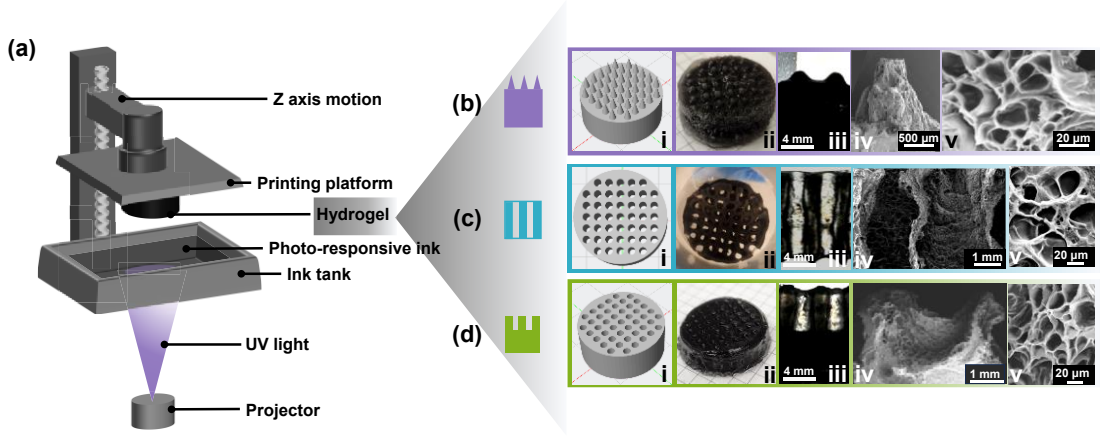

Figure 7.2 (a) Schematic illustration of the bottom-up DLP 3D printing method. For the 3D printed 5PVA15PHEA-N (b), 5PVA15PHEA-H (c), and 5PVA15PHEA-C (d) hydrogels: (i) designed 3D models, (ii) physical images, (iii) longitudinal cross section optical images, (iv) cross-sectional SEM images, and (v) the zoom-in SEM images showing the pores on the raised node structure of 5PVA15PHEA-N, the hole wall of 5PVA15PHEA-H, and the concave structure of 5PVA15PHEA-C, respectively.

A bottom-up DLP 3D printer (Figure 7.2a) was used to fabricate the hydrogels. A 405 nm near-UV light source located beneath the ink tank cured the precursors layer by layer, starting from the bottom and progressively forming the structure on the printing platform. The printing formulation used was the same as in Chapter 6, designed to generate abundant pores for excellent hydration property. It consisted of the HEA monomer, a small amount of long-chain PVA, trace amounts of the cross-linker PEGDA, the photoinitiator LAP, and GO as the PTM.

The resulting hydrogels are denoted as 5PVA15PHEA-X, where 5 and 15 represent the weight concentration of the corresponding precursor, and X stands for the designed shape of the hydrogel. Specifically, C, N, and H represent 3D printed hydrogels with concave, raised-node, and vertical through-hole arrays on their surface, respectively. The width of

the concave, raised-node, and vertical through-hole structures was 2 mm, with a spacing of 2 mm between them (Figure 7.2). Comparative analysis of Figures 7.2a-7.2c (i and ii) reveals that the 3D-printed SSG hydrogels demonstrate high structural fidelity, retaining their designed morphology even after freeze-drying. Characterization of longitudinal sections shows distinct raised nodes (Figure 7.2a-iii), as well as full-pass (Figure 7.2b-iii) and half-pass (Figure 7.2c-iii)) channel structures. The uniform black coloration of the printed hydrogels confirms even distribution of GO nanosheets, ensuring effective photothermal conversion. SEM imaging post-freeze-drying further highlights the internal architecture, displaying a homogeneous pore structure on both the raised nodes and channel walls (Figures 7.2a-7.2c, iv and v).

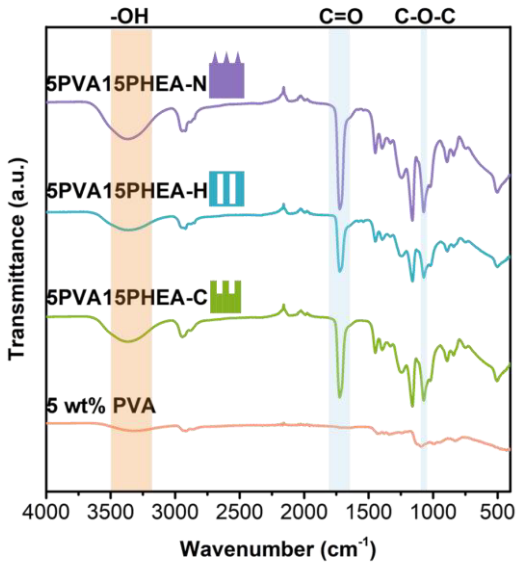

Figure 7.3 FT-IR spectra of the 3D printed 5PVA15PHEA-N, H, C hydrogels. A control sample of pristine 5 wt% PVA hydrogel is included.

FT-IR spectra of the 3D printed hydrogels were performed to confirm their chemical composition (Figure 7.3). All the hydrogels exhibited a characteristic absorption peak

between 1,050 and 1,100 cm^{-1}, which can be ascribed to the stretching vibrations of the -OH of PVA, but our printed hydrogels had a stronger signal than the pristine PVA hydrogel due to the -OH group vibrations of PHEA. Additionally, characteristic peaks at 1,724 cm^{-1} and 1,170 cm^{-1} were also observed, which are attributed to the vibration of C=O and C-O groups of PHEA, respectively. Overall, these FT-IR spectra indicate the successful preparation of SSG hydrogels via DLP 3D printing.

7.3.2 Intermediate Water within the 3D Printed Hydrogels

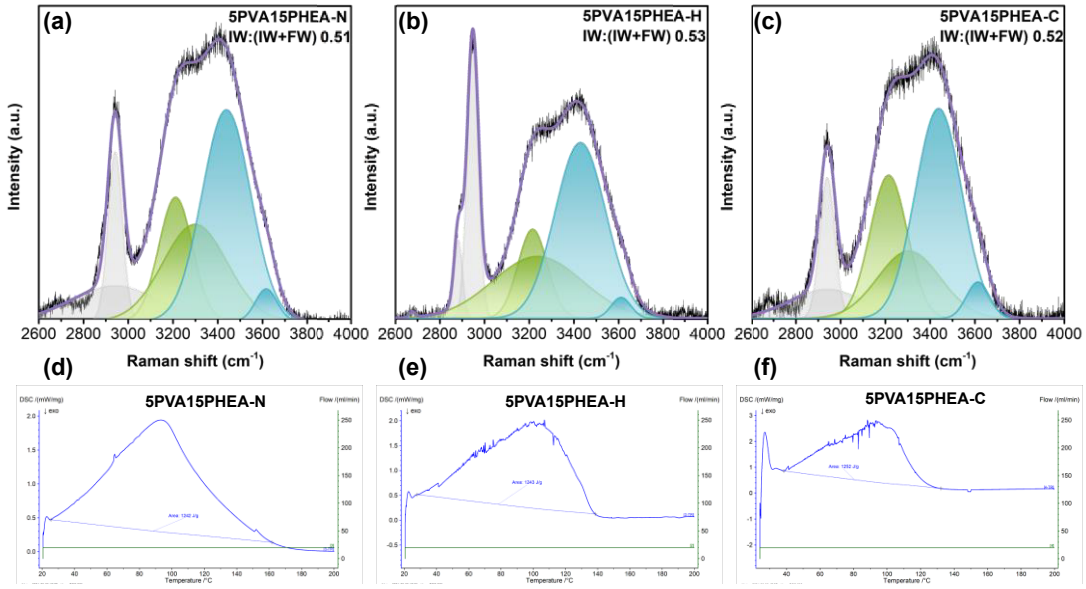

Figure 7.4 Fitting curves for the (a) 5PVA15PHEA-N, (b) 5PVA15PHEA-H, and (c) 5PVA15PHEA-C hydrogels in the Raman spectrum within the O-H stretching energy region. Free water is represented by the green peaks, whereas intermediate water is represented by the blue peaks. Raw DSC curves and the equivalent water vaporization enthalpies calculated from the integrated area of (d) 5PVA15PHEA-N, (e) 5PVA15PHEA-H, and (f) 5PVA15PHEA-C hydrogels, respectively.

For the later fair comparison in 7.3.3, although the same printing formulation was used for 5PVA15PHEA-C, N, and H, their IW contents were quantified using Raman

spectroscopy. For this study, Raman measurements were performed on all 3D-printed hydrogels that had been fully saturated with DI water, and peak fitting was used to calculate the IW contents of each sample (Figures 7.4a-7.4c). The presence of IW molecules, characterized by weaker or partially formed hydrogen bonds, is indicated by the blue peaks at approximately 3,514 cm^{-1} and 3,630 cm^{-1}. In contrast, the green peaks at 3,233 cm^{-1} and 3,401 cm^{-1} correspond to FW with fully formed hydrogen bonds (Zhao et al., 2018; Zhou et al., 2018). The IW content is typically assessed through the ratio of IW to the sum of IW and FW, expressed as [IW:(IW+FW)], calculated from the integrated areas under the fitting spectral peaks. As anticipated, the IW contents of 5PVA15PHEA-C, N, and H are nearly identical, averaging 0.52, as they were all 3D-printed using the same formulation. Correspondingly, the equivalent water vaporization enthalpies, measured via differential scanning calorimetry (DSC) (Figures 7.4d–7.4f), also yielded similar results, with an average value of 1,242 J g^{-1}.

7.3.3 Water and Heat Balance during ISSG Tests

Then, the solar driven evaporation rates of the 3D-printed hydrogels at 24 ºC and 1 atm was assessed (Figure 7.5a). To minimize the influence of external disturbances, the entire water surface in a container was covered with a layer of EPS sheet. To prevent heat from transferring to the balance, a thick layer of EPE foam was laid underneath the container. We tracked the changes in mass of bulk water containing hydrogels over three hours of solar irradiation (Figure 7.5d), and calculated mass loss over time by determining the

slope from a linear fit. All 3D-printed hydrogels demonstrated significantly higher steam generation rates than that of water evaporation under static conditions. Among the 3D-printed hydrogels with different structures, 5PVA15PHEA-C managed to achieve the highest evaporation rate of 3.56 kg m^{-2} h^{-1}, followed by 5PVA15PHEA-H with a rate of 3.04 kg m^{-2} h^{-1}, while 5PVA15PHEA-N had the lowest evaporation rate at 2.86 kg m^{-2} h^{-1}. To further investigate the impact of hydrogel structures on SSG performance, the heat and water management properties of these hydrogels were discussed as follows.

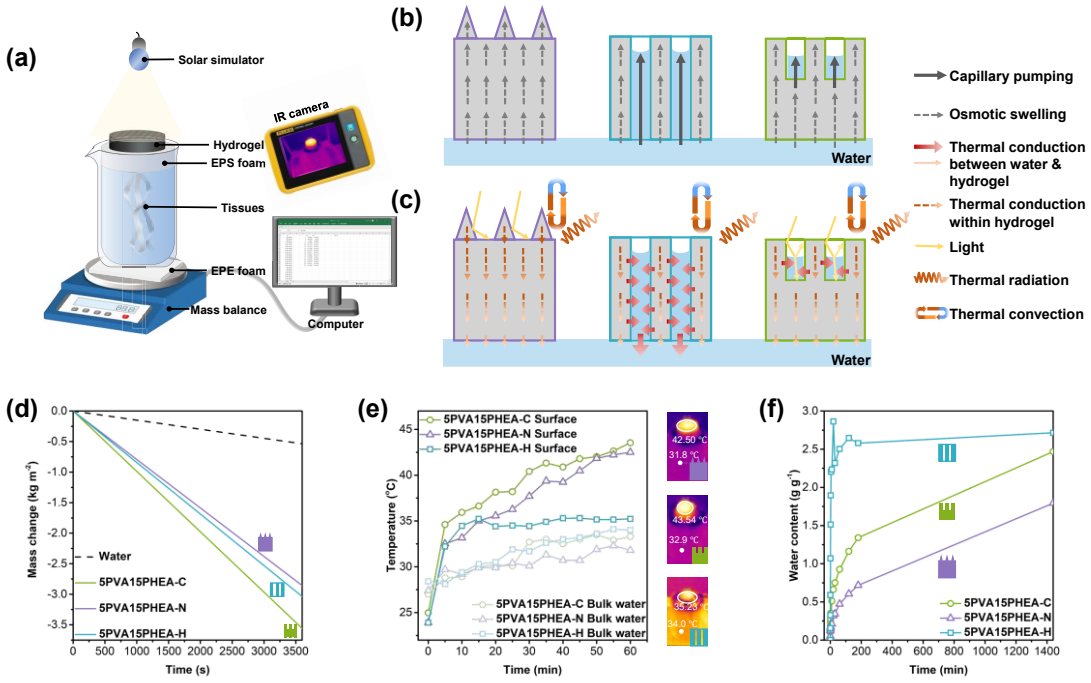

Figure 7.5 The SSG performance of the printed hydrogels. (a) A home-made set up for the SSG test. The schematic illustrating of the (b) water transport and (c) thermal transfer in 5PVA15PHEA-N, 5PVA15PHEA-H, and 5PVA15PHEA-C. (d) Water mass changes under 1 sun irritation condition for 5PVA15PHEA-N, H, C hydrogels, and pure water. (e) The temperature variations of the 5PVA15PHEA-N, H, and C hydrogel surfaces and bulk water during the SSG test under one sun irritation. The infrared images showing the temperature equilibrium of these three differently shaped hydrogels after one hour of irritation are displayed on the right. (f) The graph showing the link between the water absorption time and the water content per gramme of the corresponding dry gel.

Thermal photographs were taken during the SSG process using a handheld infrared camera to record the temperatures of the bulk water and the evaporation surfaces (Figure 7.5e). During the initial 5 minutes of exposure, the surface temperatures of all hydrogels exhibited a rapid increase. Then, the surface temperatures of 5PVA15PHEA-N and 5PVA15PHEA-C continued to rise to approximately 43 ºC, while the bulk water temperature stabilized at around 32 ºC. This result can be attributed to the surface patterning of these hydrogels, which enhances light absorption and promotes the temperature increase (Figure 7.5c). In contrast, the surface temperature of 5PVA15PHEA-H with vertical through-holes, increased during the initial 15 minutes and then decreased to a stable equilibrium temperature of 35°C, while the temperature of the bulk water continued to raise, reaching 34°C. This observation indicates a greater heat loss to the water body through the holes (Figure 7.5c).

The structure of hydrogels affects not only thermal management but also water management, both of which influence their SSG performance. We assess the water uptake amounts among the three hydrogels by contacting the corresponding dried gels with deionized water. As shown in Figure 3d, 5PVA15PHEA-H exhibited the fastest water absorption rate and the highest swelling ratio due to the capillary effect of its 2 mm-wide vertical holes (Figure7.5b). The 5PVA15PHEA-C showed moderate water uptake speed and swelling ratio due to weaker capillary effect of its shorter concave structure. Lacking any holes or concave surfaces, 5PVA15PHEA-N relied solely on water transport in the pores of the hydrogel, and thus had the slowest water uptake and the lowest swelling.

Considering both thermal and water management of hydrogels in SSG process, 5PVA15PHEA-C stands out due to its surface concaves, which promote a higher temperature at evaporation surface and more efficient water transport. Although 5PVA15PHEA-H benefits from rapid capillary water transport through its vertical through-holes, the significant amount of bulk water in these holes leads to a significant heat loss, and thus resulting in a moderate evaporation rate. In contrast, while 5PVA15PHEA-N achieves a higher surface temperature due to its raised-node array surface structure does not have an enhance water transport structure, and the slow water transport rate is insufficient to sustain continuous evaporation.

7.3.4 Desalination and Wastewater Purification Performance

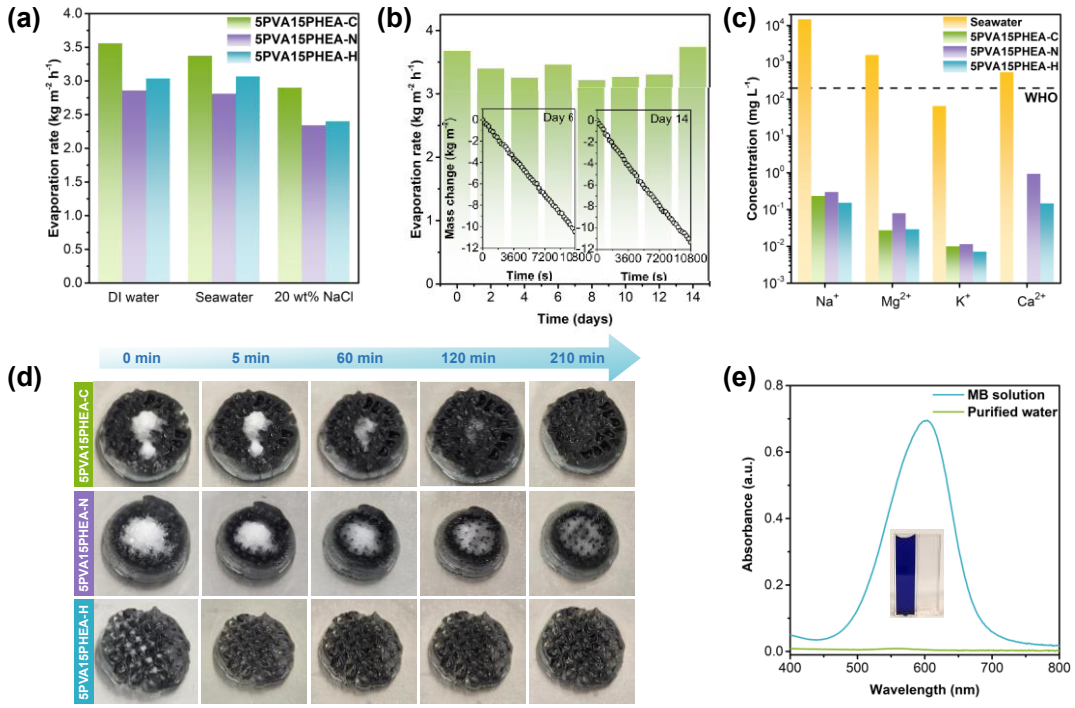

Figure 7.6 (a) The evaporation rates of 5PVA15PHEA-C, N, H in DI water, seawater and simulated brine (20 wt% NaCl solution). (b) Evaporation rates of 5PVA15PHEA-C in seawater

over two weeks. Insets: SSG performance after six and fourteen days of seawater exposure. (c) Four significant ion concentrations in seawater before and after the desalination of 5PVA15PHEA-C, N, and H hydrogel based solar steam generators. (d) The physical images of self-desalting behavior of 5PVA15PHEA-C, N, and H hydrogels. (e) The UV-vis spectra of simulated wastewater containing dye (MB) before and after the purification of 5PVA15PHEA-C hydrogel based solar steam generator. Insert: the optical photos of the MB solution before and after SSG.

Building upon the successful application of the 3D-printed hydrogels in solar driven interfacial evaporation, we further evaluated their potential for desalination and water purification in practical scenarios. Specifically, the performance of the 5PVA15PHEA-C, N, and H hydrogels was tested against real seawater (collected from Darling Harbour, Sydney, Australia; E151.20º, S33.87º) and simulated brine (20 wt% NaCl solution). The evaporation rates in these saline environments exhibited consistent trends with those observed in DI water, thereby confirming the influence of 3D- printed structural configurations (Figure 7.6a). The 5PVA15PHEA-C hydrogel achieved an evaporation rate of 3.37 kg m^{-2} h^{-1} in the seawater, and sustained a rate of 2.90 kg m^{-2} h^{-1} in the brine solution. Notably, no visible salt accumulation was detected on the hydrogel evaporation surface 6 hours of operation in seawater. To further investigate potential anti-salting-out property, an equivalent amount of NaCl powder (0.5 g) was placed on the hydrogel surface to simulate salt accumulation (Figure 7.6d). The 5PVA15PHEA-H hydrogel rapidly dissolved the surface salt within 5 minutes, facilitated by efficient water transported via capillary action through its through-pores. In comparison, the 5PVA15PHEA-C completely dissolved the salt over approximately 200 minutes, aided by the Marangoni effect associated with its concave structure (Lei et al., 2024; Wu et al.,

2020). Conversely, the 5PVA15PHEA-N hydrogel retained some salt, attributed to its relatively limited water transport capability.

Following the verification of the 5PVA15PHEA-C hydrogel's evaporation performance and anti-salting-out property, its long-term durability was assessed by immersing it in the seawater and conducting a 3-hour SSG teat under one-sun irradiation every two days. The hydrogel demonstrated stable performance for at least two weeks (Figure 7.6b).

To assess the desalination and wastewater treatment efficiency, a sealed jar was used to collect condensate (Figure 5.9c), and ICP-MS analysis was performed on the condensate obtained from the jar (Figure 7.6c). Compared to untreated seawater, the concentrations of the four major ions (Na^+, Mg^{2+}, K^+, and Ca^{2+}) in the condensate water were reduced by four to five orders of magnitude, which is well below the WHO recommended limits for drinking water (Organization, 2004, 2009a, 2009b; WHO & Geneva, 2011). We also used solutions containing organic dyes such as MB to simulate industrial effluents and used SSG technology for their treatment. After SSG process, in the UV-vis spectrum of the obtained freshwater, we found that the characteristic peak of MB at 663 nm disappeared (Figure 7.6e), which indicates that the 3D-printed hydrogel has excellent effluent purification capability.

7.3.5 Real Outdoor Desalination

Following a comprehensive laboratory investigation of the 3D-printed 5PVA15PHEA-C

hydrogel's potential for seawater desalination and effluent purification, a number of larger hydrogel samples were produced (Figure 7.7a) and a custom-designed outdoor SSG device was constructed (Figures 7.1 and 7.7b). Enhancing vapor condensation efficiency emerged as a critical factor for maximizing freshwater productivity (W. Zhang et al., 2024). To address this, the outdoor setup incorporated fan to direct the generated vapor into a separate condensation chamber, while a TE module was employed to efficiently lower the chamber temperature, thereby accelerating vapor condensation. All electronic components were powered by a solar panel. On 7th October 2025 in Sydney, Australia, the system achieved a freshwater productivity of 10.36 L m^{-2} day^{-1}, with an average solar flux of 0.47 kW m^{-2} and peak solar flux of only 0.72 kW m^{-2} (Figure 7.7c). The optimized device design facilitated a maximum condensation efficiency of 81.4%, significantly enhancing freshwater output. Overall, the 3D-printed hydrogel-based SSG hydrogel demonstrates robust anti-salting-out properties, excellent desalination capabilities, considerable potential for water treatment applications, and high freshwater productivity during outdoor testing.

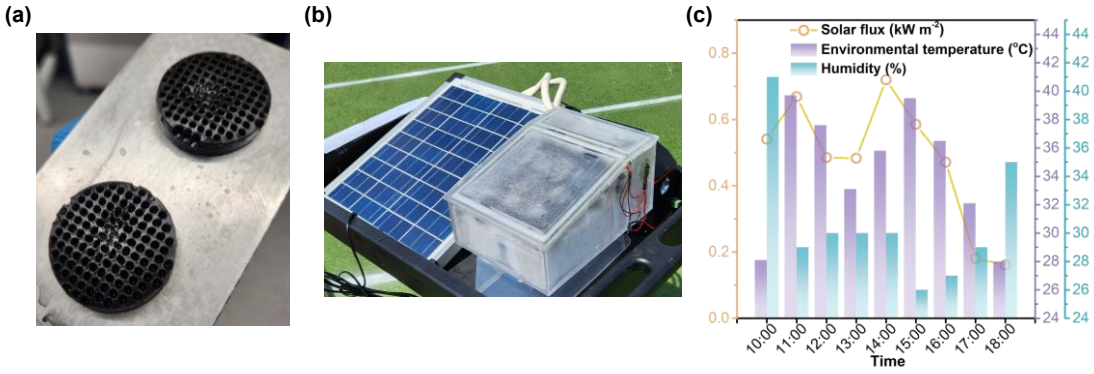

Figure 7.7 (a) Physical image of the 3D printed larger 5PVA15PHEA-C hydrogels (with a

diameter of 4 cm) for outdoor SSG. (b) The digital photo of our outdoor SSG device. (c) The environment temperature, humidity, and solar light intensity during the day of outdoor SSG test on 7th October 2024 in Sydney, Australia.

7.4 Conclusion

In this chapter, we precisely adjusting the micro/macrostructure of the hydrogels via DLP 3D printing to achieve heat and water balance. The resulting 5PVA15PHEA-C hydrogel with concave arrays on its surface demonstrates a highly porous structure, rapid water absorption, a high evaporation rate of 3.56 kg m^{-2} h^{-1} and excellent desalination performance. Additionally, freshwater productivity of our custom-designed outdoor device can reach 10.36 L m^{-2} day^{-1} freshwater and 81.4% condensation efficiency, under an average solar flux of 0.47 kW m^{-2}, offering a scalable, cost-effective solution for water purification and addressing global water scarcity.

CHAPTER 8
Conclusion and Recommendation

8.1 Conclusions

This thesis reports the development of innovative polymeric hydrogels for ISSG in water purification applications and studies the structure-properties relationship of polymeric hydrogels across nano, micro, and macro scales. At the nanoscale, the interaction between water molecules and various hydrophilic groups is investigated to enhance the intermediate water content. At the microscale, a simple freeze-thawing method utilizing low T_g polymers is introduced to construct interconnected macropores, enabling continuous water replenishment to the evaporation interface. At the macroscale, DLP 3D printing is employed to scale up hydrogel fabrication, with a novel low-precursor-concentration formulation introduced to preserve the hydrogel's porosity and hydration capacity for ISSG. Finally, leveraging DLP 3D printing, the micro/macrostructure of hydrogels is engineered to achieve a balanced management of heat and water, optimizing ISSG performance. Coupled with a custom outdoor device incorporating condensation strategies, high freshwater productivity is achieved, paving the way for the industrialization of ISSG in water purification. The main findings on polymeric hydrogels for ISSG are as follows:

For the polymeric hydrogel design at the nanoscale:

- The hydration ability of different hydrophilic groups is correlated to the varying performance of their corresponding hydrogels in ISSG. As a result, we established the relationships between structure, property, and application.

- The weakening of different IW hydrogen bonding energies induced by different groups is also simulated to assess the difficulty of freeing the IW from hydrogen bonding.

- Highly charged polymer chains with $-SO_3H$ or $-N^+(CH_3)_3Cl^-$ groups interact strongly with water molecules, so high energies are required to overcome the hydrogen bonding. This is evidenced by the large amount of FW produced therein as well as the high equivalent enthalpy of water evaporation.

- In contrast, relatively neutral hydrogels (e.g. -COOH, -OH, -C-O-C-, $-N(CH_3)_2$, and $-NH_2$) are able to establish mild interactions with water molecules, which is reflected in the fact that IWs are more readily released from hydrogen bonds. The higher content as well as the easier vaporization of the IW can guarantee lower equivalent water vaporization enthalpy and better ISSG performance.

- For the first time, the hydration ability and ISSG performance of seven different hydrogels including PAMPSA, PAA, PHEA, PPEG, PDMA, PAM, and PAETAC hydrogels synthesized by the same method and same photothermal materials loading under the same conditions are fairly compared. In all, their ISSG performance can be sorted in the following order: $-N^+(CH_3)_3Cl^- < -SO_3H <$ -COOH < -OH < -C-O-C- < $-N(CH_3)_2 < -NH_2$.

For the polymeric hydrogel design at the microscale:

- For rapid water replenishment, interconnected macroporous structure was successfully constructed via a facile freeze-thawing method compared to other complicated and costly strategies (i.e., direction-freezing), which has the potential for future low-cost, large-scale production.

- We provided a guidance on the selection of polymer precursors for the cryogel synthesis, and identified the key role of glass transition temperature.

- The experimental results show that this cryogel solar steam generator exhibits rapid rehydration rate, high intermediate water content (67 %), lower equivalent water evaporation enthalpy (861.5 J g^{-1}), excellent evaporation rate (3.59 kg m^{-1} h^{-1} under one sun), high salt resistance and long-term durability, prospective for future practical applications.

For the development of a DLP 3D printing formulation:

- We are the first to overcome the limitations of DLP 3D printing for efficient ISSG by developing high-porosity hydrogels optimized for high-water-content, achieving through the incorporation of long-chain polymers that allow for reduced precursor concentrations.

- By adding long-chain PVA for effective physical entanglements and GO as a filler, we maintained high structural fidelity and mechanical strength in the 3D-printed hydrogels, despite using only 20 wt% precursor material.

- Our high-porosity hydrogels achieved an exceptional evaporation rate of 3.56 kg m^{-2} h^{-1} — the highest reported value among all 3D-printed hydrogels to date — while using less than half the precursor concentration compared to previous studies, underscoring the remarkable cost-effectiveness of our approach.

For the polymeric hydrogel design at the micro/macroscale and outdoor device:

- Using our innovative 3D printing formulation, we printed hydrogels with three distinct high-fidelity surface structures — raised nodes, concave surfaces, and vertical through-hole arrays — each exhibiting abundant porosity for effective ISSG.

- Among these structures, the concave-surfaced hydrogel displayed an optimal balance of water and heat management, achieving excellent solar water purification performance.

- Concave-surfaced hydrogels also show great anti-salt property aided by the Marangoni effect.

- Combined with a custom outdoor device utilizing condensation strategies, significant freshwater productivity of 10.36 L m^{-2} day^{-1} is achieved, laying the foundation for the industrial application of ISSG in water purification.

8.2 Recommendations for Future Works

Although hydrogel-based ISSG has achieved significant progress over its six years as an

emerging field—such as the development of novel photothermal materials for improved solar-thermal conversion efficiency and strategies to enhance light capture, thermal insulation, and water management—efforts to delve deeply into its fundamental principles for further performance optimization, establish advanced characterization and testing methods, and promote industrialization remain in their infancy. Therefore, future research on polymeric hydrogel-based ISSG should focus on the following key aspects:

Firstly, as for the fundamental mechanism, most research in this field has established that the presence of intermediate water is a critical factor in enhancing interfacial solar steam generation performance in polymeric hydrogels compared to other materials, such as natural materials (Xie et al., 2021), and carbon-based materials (Gong et al., 2019; Liu et al., 2018; P. Zhang et al., 2018). The IW with weakened or partially hydrogen bonding can readily detach from adjacent water molecules. This allows clusters of water molecules to transition to the gas phase much more easily compared to bulk water. However, the mechanisms behind the formation of intermediate water and strategies to promote its generation remain significantly underexplored. In Chapter 4 of this thesis, we try to investigate this from the angle of chemical structure of polymer chains, and demonstrate how various hydrophilic groups can influence the generation of intermediate water. The recent advancement in metallic λ-Ti_3O_5 by Bo Yang *et al.*(Yang et al., 2023), also revealed that the excited water molecules (*i.e.* H_3O^*) can be generated above the U-shaped grooves, leading to the formation of water clusters. These clusters, in turn, enhance the evaporation of water. Another work hypothesized a Photomolecular Effect (Tu et al., 2023) different

from the mainstream Photothermal Effect, where photons detach water clusters from the surface region. This effect is driven by quadrupole forces on polar water molecules connected by hydrogen bonds, arising from rapid changes in the electric field perpendicular to the interface, as described by Maxwell's equations. Furthermore, in seawater desalination, Mg^{2+} and Ca^{2+} ions accumulated at the evaporation interface (Yu et al., 2024) by incorporated ion-exchange materials can directly disturbed the hydrogen bonding of water molecules to produce more IW. In all, the mechanisms underlying the formation of intermediate water and water clusters, as well as strategies to promote their generation, are actively being explored, but remain inconclusive. Greater efforts are needed in this direction to achieve fundamental insights that can drive significant performance improvements in hydrogel-based ISSG.

Secondly, the methods for calculating the interfacial evaporation enthalpy of water in polymeric hydrogels remain inadequately rigorous. Some studies have employed a dark evaporation method, wherein saturated hydrogels are placed in a sealed container with supersaturated potassium carbonate solution, and the evaporation enthalpy is inferred from the amount of water evaporated over a fixed period. However, this method fails to replicate the actual temperature and pressure conditions of the ISSG process, undermining its reliability. Another commonly used approach is the determination of equivalent water vaporization enthalpy via DSC or TGA-DSC, as applied in this thesis. Although these instruments provide high precision, they analyze only small hydrogel fragments, and the pressure conditions during the tests differ from those in real ISSG applications, limiting

the accuracy of the measurements. As a result, while the relative trends of equivalent water vaporization enthalpy calculated with these methods are often deemed reliable, the absolute values are frequently overestimated compared to the actual interfacial evaporation enthalpy. This overestimation can lead to inconsistencies, such as solar-to-vapor energy efficiency calculations based on Equation (1) exceeding 100%. Furthermore, current methods typically measure the evaporation enthalpy of an entire hydrogel sample or a small section rather than focusing on the evaporation enthalpy specifically at the interface. To address these limitations, collaborative efforts among researchers are essential to develop more accurate and representative methods for determining interfacial evaporation enthalpy in hydrogels. Such advancements would significantly enhance the rigor and reliability of studies in this field, paving the way for more precise performance assessments and improvements in ISSG technologies.

For the future real-world application of hydrogel-based ISSG, several critical challenges must be addressed. The first key challenge is the large-scale production of hydrogels while preserving their structural integrity, functional properties, and high ISSG efficiency. As demonstrated in Chapter 6, we develop a low-precursor-concentration 3D printing formulations that enhance scalability. However, further optimization of manufacturing techniques, such as industrial-scale 3D printing or other cost-effective fabrication methods, is required to meet the demands of large-scale deployment. The second challenge focuses on advancing device design, particularly in the integration of efficient condensation systems. High-performance condensation mechanisms are critical for

maximizing freshwater productivity and improving the overall efficiency of ISSG systems. Future research should explore novel condenser materials and structures, as well as strategies to minimize heat loss and enhance water recovery rates in outdoor environments. The third aspect emphasizes the use of sustainable and recyclable materials. Future efforts should prioritize biodegradable hydrogels or materials that are non-toxic and environmentally benign, ensuring minimal ecological impact even under prolonged exposure to natural conditions. Additionally, the development of biocompatible, or biodegradable ISSG hydrogels to minimize the environmental hazards of discarded hydrogels will further enhance the sustainability and practicality of this technology. Addressing these challenges will require a multidisciplinary approach, involving material science, engineering, and environmental research, to bridge the gap between laboratory prototypes and real-world applications. These advancements will play a pivotal role in scaling up hydrogel-based ISSG for widespread use in water purification.

References

(FAO), F. a. A. O. o. t. U. N. (2012). *Coping with Water Scarcity: An Action Framework for Agriculture and Food Security* (FAO, Ed.).

Al-Amshawee, S., Yunus, M. Y. B. M., Azoddein, A. A. M., Hassell, D. G., Dakhil, I. H., & Hasan, H. A. (2020). Electrodialysis desalination for water and wastewater: A review. *Chemical Engineering Journal, 380*. https://doi.org/10.1016/j.cej.2019.122231

Al-Karaghouli, A., & Kazmerski, L. L. (2013). Energy consumption and water production cost of conventional and renewable-energy-powered desalination processes. *Renewable Sustainable Energy Reviews, 24*, 343-356. https://doi.org/10.1016/j.rser.2012.12.064

Alketbi, A. S., Raza, A., Sajjad, M., Li, H., AlMarzooqi, F., & Zhang, T. (2021). Direct solar vapor generation with micro-3D printed hydrogel device. *EcoMat, 4*(1). https://doi.org/10.1002/eom2.12157

AlMarzooqi, F. A., Al Ghaferi, A. A., Saadat, I., & Hilal, N. (2014). Application of capacitive deionisation in water desalination: a review. *Desalination, 342*, 3-15. https://doi.org/10.1016/j.desal.2014.02.031

Baimenov, A., Berillo, D. A., Poulopoulos, S. G., & Inglezakis, V. J. (2020). A review of cryogels synthesis, characterization and applications on the removal of heavy metals from aqueous solutions. *Adv Colloid Interface Sci, 276*, 102088. https://doi.org/10.1016/j.cis.2019.102088

Bamufleh, H., Abdelhady, F., Baaqeel, H. M., & El-Halwagi, M. M. (2017). Optimization of multi-effect distillation with brine treatment via membrane distillation and process heat integration. *Desalination, 408*, 110-118. https://doi.org/10.1016/j.desal.2017.01.016

Cao, S., Jiang, J., Tian, Q., Guo, C., Wang, X., Dai, K., & Xu, Q. (2020). Building of Multifunctional and Hierarchical HxMoO3/PNIPAM Hydrogel for High-efficiency Solar Vapor Generation. *Green Energy & Environment*. https://doi.org/10.1016/j.gee.2020.12.012

Chakkaravarthy, D. N. (2019). Water Scarcity- Challenging the Future. *International Journal of Agriculture Environment and Biotechnology, 12*(3), 187-193. https://doi.org/10.30954/0974-1712.08.2019.2

Chaule, S., Hwang, J., Ha, S. J., Kang, J., Yoon, J. C., & Jang, J. H. (2021). Rational Design of a High Performance and Robust Solar Evaporator via 3D-Printing Technology. *Adv Mater, 33*(38), e2102649. https://doi.org/10.1002/adma.202102649

Chen, J., Lee, M., Qiu, Y., Wu, C., Li, B., & Yin, Y. (2022). Emulsion-templated synthesis of 3D evaporators for efficient solar steam generation. *SmartMat, 4*(2), e1140. https://doi.org/10.1002/smm2.1140

Chen, J., Wang, D., Li, X., Sun, H., Zhao, H., Li, Y., Liu, X., & Shi, G. (2021). Photothermal Membrane of CuS/Polyacrylamide–Carboxymethyl

Cellulose for Solar Evaporation. *ACS Applied Polymer Materials, 3*(5), 2402-2410. https://doi.org/10.1039/C7MH01064H

Chen, S., Liu, Y., Wang, Y., Xu, K., Zhang, X., Zhong, W., Luo, G., & Xing, M. (2021). Dual-functional superwettable nano-structured membrane: From ultra-effective separation of oil-water emulsion to seawater desalination. *Chemical Engineering Journal, 411*, 128042. https://doi.org/10.1016/j.cej.2020.128042

Chen, X., Wu, Z., Lai, D., Zheng, M., Xu, L., Huo, J., Chen, Z., Yuan, B., & Fu, M.-L. (2020). Resilient biomass-derived hydrogel with tailored topography for highly efficient and long-term solar evaporation of high-salinity brine. *Journal of Materials Chemistry A, 8*(43), 22645-22656. https://doi.org/10.1039/d0ta07040h

Chen, Y., Yang, J., Zhu, L., Jia, X., Wang, S., Li, Y., & Song, H. (2021). Integrated highly hydrated cellulose network with synergistic photothermal effect for efficient solar-driven water evaporation and salt resistance. *Journal of Materials Chemistry A, 9*, 15482-15492. https://doi.org/10.1039/D1TA04325K

Cui, W. R., Zhang, C. R., Liang, R. P., Liu, J., & Qiu, J. D. (2021). Covalent Organic Framework Sponges for Efficient Solar Desalination and Selective Uranium Recovery. *ACS Appl Mater Interfaces, 13*(27), 31561–31568. https://doi.org/10.1021/acsami.1c04419

Dech, S., Wruk, V., Fik, C. P., & Tiller, J. C. (2012). Amphiphilic polymer conetworks derived from aqueous solutions for biocatalysis in organic solvents. *Polymer, 53*(3), 701-707. https://doi.org/10.1016/j.polymer.2011.12.027

Deng, Z., Miao, L., Liu, P.-F., Zhou, J., Wang, P., Gu, Y., Wang, X., Cai, H., Sun, L., & Tanemura, S. (2019). Extremely high water-production created by a nanoink-stained PVA evaporator with embossment structure. *Nano Energy, 55*, 368-376. https://doi.org/10.1016/j.nanoen.2018.11.002

Deng, Z., Zhou, J., Miao, L., Liu, C., Peng, Y., Sun, L., & Tanemura, S. (2017). The emergence of solar thermal utilization: solar-driven steam generation. *Journal of Materials Chemistry A, 5*(17), 7691-7709. https://doi.org/10.1039/C7TA01361B

Dette, C., Pérez-Osorio, M. A., Kley, C. S., Punke, P., Patrick, C. E., Jacobson, P., Giustino, F., Jung, S. J., & Kern, K. (2014). TiO2 anatase with a bandgap in the visible region. *Nano Lett, 14*(11), 6533-6538. https://doi.org/10.1021/nl503131s

Dhand., A. P., Davidson., M. D., Zlotnick., H. M., Kolibaba., T. J., Killgore3., J. P., & Burdick., J. A. (2024). Additive manufacturing of highly entangled polymer networks. *science, 385*(6708), 566-572. https://doi.org/10.1126/science.adn69

Duan, Y., Weng, M., Zhang, W., Qian, Y., Luo, Z., & Chen, L. (2021). Multi-functional carbon nanotube paper for solar water evaporation combined with electricity generation and storage. *Energy Conversion and Management, 241*, 114306. https://doi.org/10.1016/j.enconman.2021.114306

Duong, H. C., Xia, L., Ma, Z., Cooper, P., Ela, W., & Nghiem, L. D. (2017). Assessing the performance of solar thermal driven membrane distillation for seawater desalination by computer simulation. *Journal of Membrane Science, 542*, 133-142. https://doi.org/10.1016/j.memsci.2017.08.007

Fan, D., Lu, Y., Zhang, H., Xu, H., Lu, C., Tang, Y., & Yang, X. (2021). Synergy of photocatalysis and photothermal effect in integrated 0D perovskite oxide/2D MXene heterostructures for simultaneous water purification and solar steam generation. *Applied Catalysis B: Environmental, 295*, 120285. https://doi.org/10.1016/j.apcatb.2021.120285

Feng, J., Bai, B., Yang, L., Hu, N., & Wang, H. (2021). Low-cost and facile hydrophilic amplification of raw corn straws for the applications of highly efficient interfacial solar steam generation. *Materials Chemistry and Physics, 271*, 124904. https://doi.org/10.1016/j.matchemphys.2021.124904

Gao, M., Connor, P. K. N., & Ho, G. W. (2016). Plasmonic photothermic directed broadband sunlight harnessing for seawater catalysis and desalination. *Energy Environmental Science, 9*(10), 3151-3160. https://doi.org/10.1039/C6EE00971A

Gao, M., Zhu, L., Peh, C. K., & Ho, G. W. (2019). Solar absorber material and system designs for photothermal water vaporization towards clean water and energy production. *Energy & Environmental Science, 12*(3), 841-864. https://doi.org/10.1039/c8ee01146j

Gao, T., Wu, X., Wang, Y., Owens, G., & Xu, H. (2021). A Hollow and Compressible 3D Photothermal Evaporator for Highly Efficient Solar Steam Generation without Energy Loss. *Solar RRL, 5*(5), 2100053. https://doi.org/10.1002/solr.202100053

Geng, H., Lv, C., Wu, M., Ma, H., Cheng, H., Li, C., Yuan, J., & Qu, L. (2020). Biomimetic Antigravity Water Transport and Remote Harvesting Powered by Sunlight. *Glob Chall, 4*(11), 2000043. https://doi.org/10.1002/gch2.202000043

Geng, X., Zhang, D., Zheng, Z., Ye, G., Li, S., Tu, H., Wan, Y., & Yang, P. (2021). Integrated multifunctional device based on Bi2S3/Pd: Localized heat channeling for efficient photothermic vaporization and real-time health monitoring. *Nano Energy, 82*, 105700. https://doi.org/10.1016/j.nanoen.2020.105700

Ghaffour, N., Missimer, T. M., & Amy, G. L. (2013). Technical review and evaluation of the economics of water desalination: current and future challenges for better water supply sustainability. *Desalination, 309*, 197-207. https://doi.org/10.1016/j.desal.2012.10.015

Goh, P., Ismail, A., & Hilal, N. (2019). Desalination Technology and Advancement. In *Oxford Research Encyclopedia of Environmental Science*.

Gong, F., Li, H., Wang, W., Huang, J., Xia, D., Liao, J., Wu, M., & Papavassiliou, D. V. (2019). Scalable, eco-friendly and ultrafast solar steam generators based on one-step melamine-derived carbon sponges toward water purification. *Nano Energy, 58*, 322-330. https://doi.org/10.1016/j.nanoen.2019.01.044

Guan, Q. F., Han, Z. M., Ling, Z. C., Yang, H. B., & Yu, S. H. (2020). Sustainable Wood-Based Hierarchical Solar Steam Generator: A Biomimetic Design with Reduced Vaporization Enthalpy of Water. *Nano Lett, 20*(8), 5699-5704. https://doi.org/10.1021/acs.nanolett.0c01088

Gun'ko, V. M., Savina, I. N., & Mikhalovsky, S. V. (2013). Cryogels: morphological, structural and adsorption characterisation. *Adv Colloid Interface Sci, 187-188*, 1-46. https://doi.org/10.1016/j.cis.2012.11.001

Guo, Y., de Vasconcelos, L. S., Manohar, N., Geng, J., Johnston, K. P., & Yu,

G. (2021). Highly Elastic Interconnected Porous Hydrogels through Self-Assembled Templating for Solar Water Purification. *Angew Chem Int Ed Engl,* *134*(3), e202114074. https://doi.org/10.1002/anie.202114074

Guo, Y., de Vasconcelos, L. S., Manohar, N., Geng, J., Johnston, K. P., & Yu, G. (2022). Highly Elastic Interconnected Porous Hydrogels through Self-Assembled Templating for Solar Water Purification. *Angewandte Chemie International Edition,* *134*(3), e202114074. https://doi.org/10.1002/ange.202114074

Guo, Y., Lu, H., Zhao, F., Zhou, X., Shi, W., & Yu, G. (2020). Biomass-Derived Hybrid Hydrogel Evaporators for Cost-Effective Solar Water Purification. *Adv Mater,* *32*(11), 1907061. https://doi.org/10.1002/adma.201907061

Guo, Y., & Yu, G. (2021). Engineering Hydrogels for Efficient Solar Desalination and Water Purification. *Accounts of Materials Research,* *2*(5), 374–384. https://doi.org/10.1021/accountsmr.1c00057

Guo, Y., Zhao, F., Zhou, X., Chen, Z., & Yu, G. (2019). Tailoring Nanoscale Surface Topography of Hydrogel for Efficient Solar Vapor Generation. *Nano Lett,* *19*(4), 2530-2536. https://doi.org/10.1021/acs.nanolett.9b00252

Guo, Y., Zhao, X., Zhao, F., Jiao, Z., Zhou, X., & Yu, G. (2020). Tailoring

surface wetting states for ultrafast solar-driven water evaporation. *Energy & Environmental Science, 13*(7), 2087-2095. https://doi.org/10.1039/d0ee00399a

Guo, Y., Zhou, X., Zhao, F., Bae, J., Rosenberger, B., & Yu, G. (2019). Synergistic Energy Nanoconfinement and Water Activation in Hydrogels for Efficient Solar Water Desalination. *ACS Nano, 13*(7), 7913-7919. https://doi.org/10.1021/acsnano.9b02301

Guo, Z., Yu, F., Chen, Z., Shi, Z., Wang, J., & Wang, X. (2020). Stabilized Mo2S3 by FeS2 based porous solar evaporation systems for highly efficient clean freshwater collection. *Solar Energy Materials and Solar Cells, 211*, 110531. https://doi.org/10.1016/j.solmat.2020.110531

He, J., Fan, Y., Xiao, C., Liu, F., Sun, H., Zhu, Z., Liang, W., & Li, A. (2021). Enhanced solar steam generation of hydrogel composite with aligned channel and shape memory behavior [Article]. *Composites Science and Technology, 204*, 9, Article 108633. https://doi.org/10.1016/j.compscitech.2020.108633

Hessel, C. M., Pattani, V. P., Rasch, M., Panthani, M. G., Koo, B., Tunnell, J. W., & Korgel, B. A. (2011). Copper selenide nanocrystals for photothermal therapy. *Nano Lett, 11*(6), 2560-2566. https://doi.org/10.1021/nl201400z

Hisham, M., Saravana Kumar, G., & Deshpande, A. P. (2022). Process optimization and optimal tolerancing to improve dimensional accuracy of vat-photopolymerized functionally graded hydrogels. *Results in Engineering, 14*. https://doi.org/10.1016/j.rineng.2022.100442

Hou, S., Lv, Y., Wu, X., Guo, J., Sun, Q., Wang, L., & Jia, D. (2020). Ultralight and highly compressible coal oxide-modified graphene aerogels for organic solvent absorption and light-to-heat conversion. *New Journal of Chemistry, 44*(6), 2228-2235. https://doi.org/10.1039/c9nj05447b

Hu, C.-S., Li, H.-J., Wang, J.-Y., Haleem, A., Li, X.-C., Siddiq, M., & He, W.-D. (2019). Mushroom-Like rGO/PAM Hybrid Cryogels with Efficient Solar-Heating Water Evaporation. *ACS Applied Energy Materials, 2*(10), 7554-7563. https://doi.org/10.1021/acsaem.9b01530

Hu, N., Xu, Y., Liu, Z., Liu, M., Shao, X., & Wang, J. (2020). Double-layer cellulose hydrogel solar steam generation for high-efficiency desalination. *Carbohydr Polym, 243*, 116480. https://doi.org/10.1016/j.carbpol.2020.116480

Huang, B., Tang, R., Zheng, X., Chen, G., Li, Q., Zhang, W., & Peng, B. (2024). Structurally regulated hydrogel evaporator with excellent salt-

resistance for efficient solar interfacial water evaporation. *Journal of Environmental Chemical Engineering, 12*(1), 111827. https://doi.org/10.1016/j.jece.2023.111827

Huang, Z., Wei, J., Wan, Y., Li, P., Yu, J., Dong, J., Wang, S., Li, S., & Lee, C. S. (2021). Aligned Millineedle Arrays for Solar Power Seawater Desalination with Site-Specific Salt Formation. *Small, 17*(43), 2101487. https://doi.org/10.1002/smll.202101487

Huo, B., Jiang, D., Cao, X., Liang, H., Liu, Z., Li, C., & Liu, J. (2019). N-doped graphene /carbon hybrid aerogels for efficient solar steam generation. *Carbon, 142*, 13-19. https://doi.org/10.1016/j.carbon.2018.10.008

Ibrahim, I., Seo, D. H., McDonagh, A. M., Shon, H. K., & Tijing, L. (2021). Semiconductor photothermal materials enabling efficient solar steam generation toward desalination and wastewater treatment. *Desalination, 500*, 114853. https://doi.org/10.1016/j.desal.2020.114853

Immerzeel, W. W., Van Beek, L. P., & Bierkens, M. F. (2010). Climate change will affect the Asian water towers. *science, 328*(5984), 1382-1385. https://doi.org/10.1126/science.1183188

Indriyati, Primadona, I., Permatasari, F. A. A., Irham, M. A., nasir, D. E. M., & Iskandar, F. (2021). Recent advances and rational design strategies

of carbon dots towards highly efficient solar evaporation. *Nanoscale, 13*(16), 7523-7532. https://doi.org/10.1039/d1nr00023c

Irshad, M. S., Wang, X., Abbasi, M. S., Arshad, N., Chen, Z., Guo, Z., Yu, L., Qian, J., You, J., & Mei, T. (2021). Semiconductive, Flexible MnO2 NWs/Chitosan Hydrogels for Efficient Solar Steam Generation. *ACS Sustainable Chemistry & Engineering, 9*(10), 3887-3900. https://doi.org/10.1021/acssuschemeng.0c08981

Isikgor, F. H., Subbiah, A. S., Eswaran, M. K., Howells, C. T., Babayigit, A., De Bastiani, M., Yengel, E., Liu, J., Furlan, F., & Harrison, G. (2021). Scaling-up perovskite solar cells on hydrophobic surfaces. *Nano Energy, 81*, 105633.

Jian, H., Qi, Q., Wang, W., & Yu, D. (2021). A Janus porous carbon nanotubes/poly (vinyl alcohol) composite evaporator for efficient solar-driven interfacial water evaporation. *Separation and purification technology, 264*, 118459. https://doi.org/10.1016/j.seppur.2021.118459

Jiang, S., Zhang, Z., Zhou, T., Duan, S., Yang, Z., Ju, Y., Jia, C., Lu, X., & Chen, F. (2022). Lignin hydrogel-based solar-driven evaporator for cost-effective and highly efficient water purification. *Desalination, 531*, 115706. https://doi.org/10.1016/j.desal.2022.115706

Kalogirou, S. (2005). Seawater desalination using renewable energy sources.

Progress in Energy and Combustion Science, 31(3), 242-281. https://doi.org/10.1016/j.pecs.2005.03.001

Khawaji, A. D., Kutubkhanah, I. K., & Wie, J.-M. (2008). Advances in seawater desalination technologies. *Desalination, 221*(1-3), 47-69. https://doi.org/10.1016/j.desal.2007.01.067

Kong, Y., Dan, H., Kong, W., Gao, Y., Shang, Y., Ji, K., Yue, Q., & Gao, B. (2020). Self-floating maize straw/graphene aerogel synthesis based on microbubble and ice crystal templates for efficient solar-driven interfacial water evaporation. *Journal of Materials Chemistry A, 8*(46), 24734-24742. https://doi.org/10.1039/d0ta07576k

Koosha, M., Mirzadeh, H., Shokrgozar, M. A., & Farokhi, M. (2015). Nanoclay-reinforced electrospun chitosan/PVA nanocomposite nanofibers for biomedical applications. *Rsc Advances, 5*(14), 10479-10487. https://doi.org/10.1039/C4RA13972K

Lapotko, D. (2009). Optical excitation and detection of vapor bubbles around plasmonic nanoparticles. *Optics express, 17*(4), 2538-2556. https://doi.org/10.1364/OE.17.002538

Lei, C., Guan, W., Guo, Y., Shi, W., Wang, Y., Johnston, K. P., & Yu, G. (2022). Polyzwitterionic Hydrogels for Highly Efficient High Salinity Solar Desalination. *Angewandte Chemie International Edition, 61*(36), e202208487. https://doi.org/10.1002/anie.202211267

Lei, W., Khan, S., Chen, L., Suzuki, N., Terashima, C., Liu, K., Fujishima, A., & Liu, M. (2021). Hierarchical structures hydrogel evaporator and superhydrophilic water collect device for efficient solar steam evaporation. *Nano Research, 14*(4), 1135-1140. https://doi.org/10.1007/s12274-020-3162-5

Lei, Z., Hu, B., Zhu, P., Wang, X., & Xu, B. (2024). A multilayer mesh porous 3D-felt fabric evaporator with concave array structures for high-performance solar desalination and electricity generation. *Nano Energy, 122*, 109307. https://doi.org/10.1016/j.nanoen.2024.109307

Li, C., Fan, L., Zhu, R., Li, X., Wen, P., Zhao, X., Wang, G., Zou, J., & Kim, F. (2020). Adjusting Channel Size within PVA-Based Hydrogels via Ice Templating for Enhanced Solar Steam Generation. *ACS Applied Energy Materials, 3*(9), 9216-9225. https://doi.org/10.1021/acsaem.0c01584

Li, C., Jiang, D., Huo, B., Ding, M., Huang, C., Jia, D., Li, H., Liu, C.-Y., & Liu, J. (2019). Scalable and robust bilayer polymer foams for highly efficient and stable solar desalination. *Nano Energy, 60*, 841-849. https://doi.org/10.1016/j.nanoen.2019.03.087

Li, C., Zhu, B., Liu, Z., Zhao, J., Meng, R., Zhang, L., & Chen, Z. (2022). Polyelectrolyte-based photothermal hydrogel with low evaporation enthalpy for solar-driven salt-tolerant desalination. *Chemical*

Engineering Journal, 431, 134224. https://doi.org/10.1016/j.cej.2021.134224

Li, D., Zhang, X., Zhang, S., Wang, D., Wang, Z., Liu, Y., Yu, X., Zhao, Q., & Xing, B. (2021). A flexible and salt-rejecting electrospun film-based solar evaporator for economic, stable and efficient solar desalination and wastewater treatment. *Chemosphere, 267*, 128916. https://doi.org/10.1016/j.chemosphere.2020.128916

Li, N., Qiao, L., He, J., Wang, S., Yu, L., Murto, P., Li, X., & Xu, X. (2021). Solar-Driven Interfacial Evaporation and Self-Powered Water Wave Detection Based on an All-Cellulose Monolithic Design. *Advanced Functional Materials, 31*(7), 2008681. https://doi.org/10.1002/adfm.202008681

Li, N., Shao, K., He, J., Wang, S., Li, S., Wu, X., Li, J., Guo, C., Yu, L., & Murto, P. (2023). Solar-Powered Interfacial Evaporation and Deicing Based on a 3D-Printed Multiscale Hierarchical Design. *Small, 19*(33), 2301474. https://doi.org/10.1002/smll.202301474

Li, T., Fang, Q., Wang, J., Lin, H., Han, Q., Wang, P., & Liu, F. (2021). Exceptional interfacial solar evaporation via heteromorphic PTFE/CNT hollow fiber arrays. *Journal of Materials Chemistry A, 9*(1), 390-399. https://doi.org/10.1039/d0ta09368h

Li, W., Li, X., Chang, W., Wu, J., Liu, P., Wang, J., Yao, X., & Yu, Z.-Z.

(2020). Vertically aligned reduced graphene oxide/Ti3C2Tx MXene hybrid hydrogel for highly efficient solar steam generation. *Nano Research, 13*(11), 3048-3056. https://doi.org/10.1007/s12274-020-2970-y

Li, X., Huang, J., Guo, L., Jin, X., Wang, L., Deng, Y., Xie, H., & Ye, L. (2021). Efficient solar seawater desalination constructed by oxide composite hydrogel with chitin as the base. *Inorganic Chemistry Communications, 129*, 108651. https://doi.org/10.1016/j.inoche.2021.108651

Li, Y., Shi, X.-l., Sun, L.-j., Zhao, M., Jiang, T., Jiang, W., Deng, M., Yang, S., & Wang, Y. (2021). Composite hydrogel-based photothermal self-pumping system with salt and bacteria resistance for super-efficient solar-powered water evaporation. *Desalination, 515*, 115192. https://doi.org/10.1016/j.desal.2021.115192

Liang, X., Zhang, X., Huang, Q., Zhang, H., Liu, C., & Liu, Y. (2020). Simple preparation of external-shape and internal-channel size adjustable porous hydrogels by fermentation for efficient solar interfacial evaporation. *Solar Energy, 208*, 778-786. https://doi.org/10.1016/j.solener.2020.08.038

Liang, X., Zhang, X., Liu, Z., Huang, Q., Zhang, H., Liu, C., & Liu, Y. (2020). Direction-limited water transport and inhibited heat convection loss of

gradient-structured hydrogels for highly efficient interfacial evaporation. *Solar Energy, 201*, 581-588. https://doi.org/10.1016/j.solener.2020.03.042

Lim, H., Kim, M., Yoo, J., Lee, D., Lee, M., Na, B., & Kim, S. K. (2022). Environmentally safe and renewable solar vapor generation device based on Prussian blue nanoparticles immobilized on cellulose nanofibers. *Desalination, 524*, 115477. https://doi.org/10.1016/j.desal.2021.115477

Liu, C., Cai, C., Ma, F., Zhao, X., & Ahmad, H. (2020). Accelerated solar steam generation for efficient ions removal. *J Colloid Interface Sci, 560*, 103-110. https://doi.org/10.1016/j.jcis.2019.10.055

Liu, C., Peng, Y., Cai, C., Zhang, J., & Zhao, X. (2021). Enhancing solar desalination performance based on restricted salt ions transport. *Journal of Environmental Chemical Engineering, 9*(4), 105272. https://doi.org/10.1016/j.jece.2021.105272

Liu, C., Peng, Y., & Zhao, X. (2021). Continuous solar desalination based on restricted salt crystallization zone. *Desalination, 501*, 114911. https://doi.org/10.1016/j.desal.2020.114911

Liu, J., Chen, X., Yang, H., Tang, J., Miao, R., Liu, K., & Fang, Y. (2021). Gel-emulsion templated polymeric aerogels for solar-driven interfacial evaporation and electricity generation. *Materials*

Chemistry Frontiers, 5(4), 1953-1961. https://doi.org/10.1039/D0QM00793E

Liu, J., Gui, J., Zhou, W., Tian, X., Liu, Z., Wang, J., Yang, L., Zhang, P., Huang, W., & Tu, J. (2021). Self-regulating and asymmetric evaporator for efficient solar water-electricity generation. *Nano Energy, 86*, 106112. https://doi.org/10.1016/j.nanoen.2021.106112

Liu, P.-F., Miao, L., Deng, Z., Zhou, J., Su, H., Sun, L., Tanemura, S., Cao, W., Jiang, F., & Zhao, L.-D. (2018). A mimetic transpiration system for record high conversion efficiency in solar steam generator under one-sun. *Materials Today Energy, 8*, 166-173. https://doi.org/10.1016/j.mtener.2018.04.004

Liu, Y., Luo, B., Liu, H., He, M., Wang, R., Wang, L., Quan, Z., Yu, J., & Qin, X. (2023). 3D printed electrospun nanofiber-based pyramid-shaped solar vapor generator with hierarchical porous structure for efficient desalination. *Chemical Engineering Journal, 452*, 139402. https://doi.org/10.1016/j.cej.2022.139402

Liu, Y., Tian, J., Xu, L., Wang, Y., Fei, X., & Li, Y. (2020). Multilayer graphite nano-sheet composite hydrogel for solar desalination systems with floatability and recyclability. *New Journal of Chemistry, 44*(46), 20181-20191. https://doi.org/10.1039/d0nj04409a

Liu, Y., & Zheng, X. (2024). 3D printed thermo-responsive hydrogel

evaporator with enhanced water transport for efficient solar steam generation. *Solar Energy, 273*. https://doi.org/10.1016/j.solener.2024.112507

Liu, Z., Qing, R.-K., Xie, A.-Q., Liu, H., Zhu, L., & Chen, S. (2021). Self-contained Janus Aerogel with Antifouling and Salt-Rejecting Properties for Stable Solar Evaporation. *ACS Applied Materials and Interfaces, 13*(16), 18829-18837. https://doi.org/10.1021/acsami.1c02198

Long, Y., Huang, S., Yi, H., Chen, J., Wu, J., Liao, Q., Liang, H., Cui, H., Ruan, S., & Zeng, Y.-J. (2019). Carrot-inspired solar thermal evaporator. *Journal of Materials Chemistry A, 7*(47), 26911-26916. https://doi.org/10.1039/c9ta08754k

Loo, S.-L., Vásquez, L., Zahid, M., Costantino, F., Athanassiou, A., & Fragouli, D. (2021). 3D Photothermal Cryogels for Solar-Driven Desalination. *ACS Applied Materials and Interfaces, 13*(26), 30542–30555. https://doi.org/10.1021/acsami.1c05087

Lou, G., Wang, Y., Ma, Y., Kou, J., Wu, F., & Fan, J. (2021). Reduced graphene oxide-based calcium alginate hydrogel as highly efficient solar steam generation membrane for desalination. *Frontiers of Materials Science, 15*(1), 138-146. https://doi.org/10.1007/s11706-021-0536-x

Lozinsky, V. I. (2002). Cryogels on the basis of natural and synthetic polymers: preparation, properties and application. *Russian Chemical Reviews,* *71*(6), 489-511. https://doi.org/10.1070/RC2002v071n06ABEH000720

Lozinsky, V. I. (2014). A Brief History of Polymeric Cryogels. In O. Okay (Ed.), *Polymeric Cryogels* (Vol. 263, pp. 1-48). Springer, Cham. https://doi.org/10.1007/978-3-319-05846-7_1

Lozinsky, V. I., & Okay, O. (2014). Basic Principles of Cryotropic Gelation. In O. Okay (Ed.), *Polymeric Cryogels* (Vol. 263, pp. 49-101). Springer, Cham. https://doi.org/10.1007/978-3-319-05846-7_2

Lu, H., Li, M., Wang, X., Wang, Z., Pi, M., Cui, W., & Ran, R. (2022). Recyclable physical hydrogels as durable and efficient solar-driven evaporators. *Chemical Engineering Journal, 450*, 138257. https://doi.org/10.1016/j.cej.2022.138257

Lu, H., Shi, W., Zhao, F., Zhang, W., Zhang, P., Zhao, C., & Yu, G. (2021). High-Yield and Low-Cost Solar Water Purification via Hydrogel-Based Membrane Distillation. *Advanced Functional Materials, 31*(19), 2101036. https://doi.org/10.1002/adfm.202101036

Lu, Y., Fan, D., Wang, Y., Xu, H., Lu, C., & Yang, X. (2021). Surface Patterning of Two-Dimensional Nanostructure-Embedded Photothermal Hydrogels for High-Yield Solar Steam Generation. *ACS*

Nano, 15(6), 10366–10376. https://doi.org/10.1021/acsnano.1c02578

Lu, Y., Wang, X., Fan, D., Yang, H., Xu, H., Min, H., & Yang, X. (2020). Biomass derived Janus solar evaporator for synergic water evaporation and purification. *Sustainable Materials and Technologies, 25*, e00180. https://doi.org/10.1016/j.susmat.2020.e00180

Luo, X., Zhang, J., Tao, J., Wang, X., Zhao, S., Chen, Z., Liu, S., Li, J., & Li, S. (2021). Solar-powered "pump" for uranium recovery from seawater. *Chemical Engineering Journal, 416*, 129486. https://doi.org/10.1016/j.cej.2021.129486

Ma, S., Chiu, C. P., Zhu, Y., Tang, C. Y., Long, H., Qarony, W., Zhao, X., Zhang, X., Lo, W. H., & Tsang, Y. H. (2017). Recycled waste black polyurethane sponges for solar vapor generation and distillation. *Applied Energy, 206*, 63-69. https://doi.org/10.1016/j.apenergy.2017.08.169

Mao, S., Feng, A., Zhang, X. S., Onggowarsito, C., Chen, Q., Su, D., & Fu, Q. (2023). Investigation of structure-property-application relationships of the hydrogel-based solar vapor generator. *Journal of Materials Chemistry A, 11*(42), 23062-23070. https://doi.org/10.1039/D3TA05278H

Mao, S., Johir, M., Onggowarsito, C., Feng, A., Nghiem, L., & Fu, Q. (2022). Recent Developments of Hydrogel Based Solar Water Purification

Technology. *Materials Advances,* *3*(3), 1322-1340. https://doi.org/10.1039/d1ma00894c

Mao, S., Onggowarsito, C., Feng, A., Zhang, S., Fu, Q., & Nghiem, L. D. (2023). A cryogel solar vapor generator with rapid water replenishment and high intermediate water content for seawater desalination. *Journal of Materials Chemistry A,* *11*(2), 858-867. https://doi.org/10.1039/d2ta08317e

Meng, F. L., Gao, M., Ding, T., Yilmaz, G., Ong, W. L., & Ho, G. W. (2020). Modular Deformable Steam Electricity Cogeneration System with Photothermal, Water, and Electrochemical Tunable Multilayers. *Advanced Functional Materials,* *30*(32), 2002867. https://doi.org/10.1002/adfm.202002867

Meng, X., Yang, J., Ramakrishna, S., Sun, Y., & Dai, Y. (2020a). Gradient-aligned Au/graphene meshes with confined heat at multiple levels for solar evaporation and anti-gravity catalytic conversion. *Journal of Materials Chemistry A,* *8*(32), 16570-16581. https://doi.org/10.1039/d0ta04986g

Meng, X., Yang, J., Ramakrishna, S., Sun, Y., & Dai, Y. (2020b). Gradient Vertical Channels within Aerogels Based on N-Doped Graphene Meshes toward Efficient and Salt-Resistant Solar Evaporation. *ACS Sustainable Chemistry & Engineering,* *8*, 4955-4965.

https://doi.org/10.1021/acssuschemeng.0c00853

Morris, R. M. (1993). The development of the multi-stage flash distillation process: A designer's viewpoint. *Desalination, 93*(1-3), 57-68. https://doi.org/10.1016/0011-9164(93)80096-6

Nabeela, K., Thorat, M. N., Backer, S. N., Ramachandran, A. M., Thomas, R. T., Preethikumar, G., Mohamed, A. P., Asok, A., Dastager, S. G., & Pillai, S. (2021). Hydrophilic 3D Interconnected Network of Bacterial Nanocellulose/Black Titania Photothermal Foams as an Efficient Interfacial Solar Evaporator. *ACS Applied Bio Materials, 4*(5), 4373-4383. https://doi.org/10.1021/acsabm.1c00143

Neumann, O., Urban, A. S., Day, J., Lal, S., Nordlander, P., & Halas, N. (2013). Solar vapor generation enabled by nanoparticles. *ACS Nano, 7*(1), 42-49. https://doi.org/10.1021/nn304948h

Ni, F., Xiao, P., Zhang, C., Liang, Y., Gu, J., Zhang, L., & Chen, T. (2019). Micro-/Macroscopically Synergetic Control of Switchable 2D/3D Photothermal Water Purification Enabled by Robust, Portable, and Cost-Effective Cellulose Papers. *ACS Appl Mater Interfaces, 11*(17), 15498-15506. https://doi.org/10.1021/acsami.9b00380

Okay, O., & Lozinsky, V. I. (2014). Synthesis and Structure–Property Relationships of Cryogels. In O. Okay (Ed.), *Polymeric Cryogels* (Vol. 263, pp. 103-157). Springer, Cham. https://doi.org/10.1007/978-3-

319-05846-7_3

Onggowarsito, C., Feng, A., Mao, S., Zhang, S., Ibrahim, I., Tijing, L., Fu, Q., & Ngo, H. H. (2022). Development of an innovative MnO2 nanorod for efficient solar vapor generator. *Environmental Functional Materials, 1*(2), 196-203.

Onggowarsito, C., Mao, S., Zhang, X. S., Feng, A., Xu, H., & Fu, Q. (2024). Updated perspective on solar steam generation application. *Energy & Environmental Science, 17*(6), 2088-2099.

Organization, W. H. (2004). *Guidelines for drinking-water quality* (Vol. 1). World Health Organization.

Organization, W. H. (2009a). *Calcium and magnesium in drinking water: public health significance*. World Health Organization.

Organization, W. H. (2009b). *Potassium in drinking-water: background document for development of WHO guidelines for drinking-water quality*. World Health Organization.

Panagopoulos, A., Haralambous, K.-J., & Loizidou, M. (2019). Desalination brine disposal methods and treatment technologies-A review. *Science of the total environment, 693*, 133545. https://doi.org/10.1016/j.scitotenv.2019.07.351

Park, S. H., Park, J. H., Kim, J., & Lee, S. J. (2021). Simultaneous solar-driven seawater desalination and spontaneous power generation using

polyvalent crosslinked polypyrrole/alginate hydrogels. *Desalination, 500*, 114900. https://doi.org/10.1016/j.desal.2020.114900

Qasem, N. A. A., Zubair, S. M., Qureshi, B. A., & Generous, M. M. (2020). The impact of thermodynamic potentials on the design of electrodialysis desalination plants. *Energy Conversion and Management, 205*. https://doi.org/10.1016/j.enconman.2019.112448

Qasim, M., Badrelzaman, M., Darwish, N. N., Darwish, N. A., & Hilal, N. (2019). Reverse osmosis desalination: A state-of-the-art review. *Desalination, 459*, 59-104. https://doi.org/10.1016/j.desal.2019.02.008

Schlosser, C. A., Strzepek, K., Gao, X., Fant, C., Blanc, É., Paltsev, S., Jacoby, H., Reilly, J., & Gueneau, A. (2014). The future of global water stress: An integrated assessment. *Earth's Future, 2*(8), 341-361. https://doi.org/10.1002/2014EF000238

Seh, Z. W., Liu, S., Low, M., Zhang, S. Y., Liu, Z., Mlayah, A., & Han, M. Y. (2012). Janus Au-TiO2 photocatalysts with strong localization of plasmonic near-fields for efficient visible-light hydrogen generation. *Advanced materials, 24*(17), 2310-2314. https://doi.org/10.1002/adma.201104241

Semiat, R. (2008). Energy issues in desalination processes. *Environmental science & technology, 42*(22), 8193-8201.

https://doi.org/10.1021/es801330u

Shannon, M. A., Bohn, P. W., Elimelech, M., Georgiadis, J. G., Marinas, B. J., & Mayes, A. M. (2008). Science and technology for water purification in the coming decades. *Nature, 452*(7185), 301-310. https://doi.org/10.1038/nature06599

Sharshir, S., Peng, G., Wu, L., Essa, F., Kabeel, A., & Yang, N. (2017). The effects of flake graphite nanoparticles, phase change material, and film cooling on the solar still performance. *Applied Energy, 191*, 358-366. https://doi.org/10.1016/j.apenergy.2017.01.067

Shi, Y., Feng, A., Mao, S., Onggowarsito, C., Zhang, X. S., Guo, W., & Fu, Q. (2024). Hydrogels in solar-driven water and energy production: Recent advances and future perspectives. *Chemical Engineering Journal, 492*, 152303.

Shi, Y., Ilic, O., Atwater, H. A., & Greer, J. R. (2021). All-day fresh water harvesting by microstructured hydrogel membranes. *Nat Commun, 12*(1), 1-10. https://doi.org/10.1038/s41467-021-23174-0

Shi, Y., Zhang, C., Wang, Y., Cui, Y., Wang, Q., Liu, G., Gao, S., & Yuan, Y. (2021). Plasmonic silver nanoparticles embedded in flexible three-dimensional carbonized melamine foam with enhanced solar-driven water evaporation. *Desalination, 507*, 115038. https://doi.org/10.1016/j.desal.2021.115038

Shrivastava, A. (2018). Introduction to Plastics Engineering. In A. Shrivastava (Ed.), *Introduction to Plastics Engineering* (pp. 1-16). William Andrew Publishing. https://doi.org/10.1016/B978-0-323-39500-7.00001-0

Singh, S., Shauloff, N., & Jelinek, R. (2019). Solar-Enabled Water Remediation via Recyclable Carbon Dot/Hydrogel Composites. *ACS Sustainable Chemistry & Engineering, 7*(15), 13186-13194. https://doi.org/10.1021/acssuschemeng.9b02342

Southan, A., Hoch, E., Schönhaar, V., Borchers, K., Schuh, C., Müller, M., Bach, M., & Tovar, G. E. (2014). Side chain thiol-functionalized poly (ethylene glycol) by post-polymerization modification of hydroxyl groups: synthesis, crosslinking and inkjet printing. *Polymer Chemistry, 5*(18), 5350-5359. https://doi.org/10.1039/C4PY00099D

Standard, A. (2012). G173-03-Standard Tables for Reference Solar Spectral Irradiances: Direct Normal and Hemispherical on 37 Tilted Surface. *Ann. Book of ASTM Standards, 14*, 1-20.

Strathmann, H. (2010). Electrodialysis, a mature technology with a multitude of new applications. *Desalination, 264*(3), 268-288. https://doi.org/10.1016/j.desal.2010.04.069

Su, H., Zhou, J., Miao, L., Shi, J., Gu, Y., Wang, P., Tian, Y., Mu, X., Wei, A., Huang, L., Chen, S., & Deng, Z. (2019). A hybrid hydrogel with

protonated g-C3N4 and graphene oxide as an efficient absorber for solar steam evaporation. *Sustainable Materials and Technologies, 20*, e00095. https://doi.org/10.1016/j.susmat.2019.e00095

Sun, S., Wang, Y., Sun, B., Zhang, F., Xu, Q., Mi, H.-Y., Li, H., Tao, X., Guo, Z., & Liu, C. (2021). Versatile Janus Composite Nonwoven Solar Absorbers with Salt Resistance for Efficient Wastewater Purification and Desalination. *ACS Applied Materials and Interfaces, 13*(21), 24945–24956. https://doi.org/10.1021/acsami.1c05618

Sun, Y., Gao, J., Liu, Y., Kang, H., Xie, M., Wu, F., & Qiu, H. (2019). Copper sulfide-macroporous polyacrylamide hydrogel for solar steam generation. *Chemical Engineering Science, 207*, 516-526. https://doi.org/10.1016/j.ces.2019.06.044

Sun, Y., Zong, X., Qu, D., Chen, G., An, L., Wang, X., & Sun, Z. (2021). Water management by hierarchical structures for highly efficient solar water evaporation. *Journal of Materials Chemistry A, 9*(11), 7122-7128. https://doi.org/10.1039/d1ta00113b

Sun, Z., Li, Z., Li, W., & Bian, F. (2019). Mesoporous cellulose/TiO2/SiO2/TiN-based nanocomposite hydrogels for efficient solar steam evaporation: low thermal conductivity and high light-heat conversion. *Cellulose, 27*(1), 481-491. https://doi.org/10.1007/s10570-019-02823-0

Sun, Z., Wang, J., Wu, Q., Wang, Z., Wang, Z., Sun, J., & Liu, C. J. (2019). Plasmon Based Double-Layer Hydrogel Device for a Highly Efficient Solar Vapor Generation. *Advanced Functional Materials, 29*(29), 1901312. https://doi.org/10.1002/adfm.201901312

Sun, Z., Zhao, Q., Ma, S., & Wu, J. (2023). DLP 3D printed hydrogels with hierarchical structures post-programmed by lyophilization and ionic locking. *Mater Horiz, 10*(1), 179-186. https://doi.org/10.1039/d2mh00962e

Tan, M., Wang, J., Song, W., Fang, J., & Zhang, X. (2019). Self-floating hybrid hydrogels assembled with conducting polymer hollow spheres and silica aerogel microparticles for solar steam generation. *Journal of Materials Chemistry A, 7*(3), 1244-1251. https://doi.org/10.1039/c8ta10057h

Tang, C., Yang, Z., Guo, H., Wen, J. J., Nghiem, L. D., & Cornelissen, E. (2018). Potable Water Reuse through Advanced Membrane Technology. *Environ Sci Technol, 52*(18), 10215-10223. https://doi.org/10.1021/acs.est.8b00562

Tao, J., Luttrell, T., & Batzill, M. (2011). A two-dimensional phase of TiO2 with a reduced bandgap. *Nature chemistry, 3*(4), 296-300. https://doi.org/10.1038/nchem.1006

Tian, C., Li, C., Chen, D., Li, Y., Xing, L., Tian, X., Cao, Y., Huang, W., Liu,

Z., & Shen, Y. (2021). Sandwich hydrogel with confined plasmonic Cu/carbon cells for efficient solar water purification. *Journal of Materials Chemistry A,* *9*(27), 15462-15471. https://doi.org/10.1039/d1ta02927d

Tian, J., Huang, X., & Wu, W. (2020). Graphene-Based Stand-Alone Networks for Efficient Solar Steam Generation. *Industrial & Engineering Chemistry Research,* *59*(3), 1135-1141. https://doi.org/10.1021/acs.iecr.9b03523

Tian, Y., Liu, X., Xu, S., Li, J., Caratenuto, A., Mu, Y., Wang, Z., Chen, F., Yang, R., Liu, J., Minus, M. L., & Zheng, Y. (2022). Recyclable and efficient ocean biomass-derived hydrogel photothermal evaporator for thermally-localized solar desalination. *Desalination, 523*, 115449. https://doi.org/10.1016/j.desal.2021.115449

Tu, Y., Zhou, J., Lin, S., Alshrah, M., Zhao, X., & Chen, G. (2023). Plausible photomolecular effect leading to water evaporation exceeding the thermal limit. *Proc Natl Acad Sci U S A, 120*(45), e2312751120. https://doi.org/10.1073/pnas.2312751120

UNESCO, & UN-Water. (2024). *The United Nations World Water Development Report 2024: Water for Prosperity and Peace*. United Nations Educational, Scientific and Cultural Organization (UNESCO).

Vrandečić, N. S., Erceg, M., Jakić, M., & Klarić, I. (2010). Kinetic analysis

of thermal degradation of poly (ethylene glycol) and poly (ethylene oxide) s of different molecular weight. *Thermochimica Acta, 498*(1-2), 71-80. https://doi.org/10.1016/j.tca.2009.10.005

Wada, Y., Flörke, M., Hanasaki, N., Eisner, S., Fischer, G., Tramberend, S., Satoh, Y., Van Vliet, M., Yillia, P., & Ringler, C. (2016). Modeling global water use for the 21st century: Water Futures and Solutions (WFaS) initiative and its approaches. *Geoscientific Model Development, 9*, 175-222. https://doi.org/10.5194/gmd-9-175-2016

Wang, H., Zhang, R., Yuan, D., Xu, S., & Wang, L. (2020). Gas Foaming Guided Fabrication of 3D Porous Plasmonic Nanoplatform with Broadband Absorption, Tunable Shape, Excellent Stability, and High Photothermal Efficiency for Solar Water Purification. *Advanced Functional Materials, 30*(46), 2003995. https://doi.org/10.1002/adfm.202003995

Wang, J.-Y., Guo, X.-X., Chen, J., Hou, S.-C., Li, H.-J., Haleem, A., Chen, S.-Q., & He, W.-D. (2021). A versatile platform of poly(acrylic acid) cryogel for highly efficient photothermal water evaporation. *Materials Advances, 2*(9), 3088-3098. https://doi.org/10.1039/d1ma00119a

Wang, P., Gu, Y., Miao, L., Zhou, J., Su, H., Wei, A., Mu, X., Tian, Y., Shi, J., & Cai, H. (2019). Co3O4 nanoforest/Ni foam as the interface heating sheet for the efficient solar-driven water evaporation under

one sun. *Sustainable Materials and Technologies, 20*, e00106. https://doi.org/10.1016/j.susmat.2019.e00106

Wang, Q., Jia, F., Huang, A., Qin, Y., Song, S., Li, Y., & Arroyo, M. A. C. (2020). MoS2@sponge with double layer structure for high-efficiency solar desalination. *Desalination, 481*, 114359. https://doi.org/10.1016/j.desal.2020.114359

Wang, W., Niu, J., Guo, J., Yin, L., & Huang, H. (2019). In situ synthesis of PPy-FexOy-CTS nanostructured gel membrane for highly efficient solar steam generation. *Solar Energy Materials and Solar Cells, 201*, 110046. https://doi.org/10.1016/j.solmat.2019.110046

Wang, X.-Y., Xue, J., Ma, C., He, T., Qian, H., Wang, B., Liu, J., & Lu, Y. (2019). Anti-biofouling double-layered unidirectional scaffold for long-term solar-driven water evaporation. *Journal of Materials Chemistry A, 7*(28), 16696-16703. https://doi.org/10.1039/c9ta02210d

Wang, X., Li, Z., Wu, Y., Guo, H., Zhang, X., Yang, Y., Mu, H., & Duan, J. (2021). Construction of a Three-Dimensional Interpenetrating Network Sponge for High-Efficiency and Cavity-Enhanced Solar-Driven Wastewater Treatment. *ACS Appl Mater Interfaces, 13*(9), 10902-10915. https://doi.org/10.1021/acsami.0c21690

Wang, Y., Zhang, J., Liang, W., Yang, H., Guan, T., Zhao, B., Sun, Y., Chi, L., & Jiang, L. (2021). Rational Design of Plasmonic Metal

Nanostructures for Solar Energy Conversion. *CCS Chemistry, 4*(4), 1153-1168.

Wang, Z., Zhan, Z., Chen, L., Duan, G., Cheng, P., Kong, H., Chen, Y., & Duan, H. (2022). 3D-Printed Bionic Solar Evaporator. *Solar RRL, 6*(7), 2101063. https://doi.org/10.1002/solr.202101063

Wei, C., Zhang, X., Ma, S., Zhang, C., Li, Y., Chen, D., Jiang, H., Xu, Z., & Huang, X. (2021). Ultra-robust vertically aligned three-dimensional (3D) Janus hollow fiber membranes for interfacial solar-driven steam generation with salt-resistant and multi-media purification. *Chemical Engineering Journal, 425*, 130118. https://doi.org/10.1016/j.cej.2021.130118

Wei, Z., Cai, C., Huang, Y., Wang, Y., & Fu, Y. (2021). Biomimetic surface strategy of spectrum-tailored liquid metal via blackbody inspiration for highly efficient solar steam generation, desalination, and electricity generation. *Nano Energy, 86*, 106138. https://doi.org/10.1016/j.nanoen.2021.106138

Wen, B., Zhang, X., Yan, Y., Huang, Y., Lin, S., Zhu, Y., Wang, Z., Zhou, B., Yang, S., & Liu, J. (2021). Tailoring polypyrrole-based Janus aerogel for efficient and stable solar steam generation. *Desalination, 516*, 115228. https://doi.org/10.1016/j.desal.2021.115228

Wen, C., Guo, H., Yang, J., Li, Q., Zhang, X., Sui, X., Cao, M., & Zhang, L.

(2021). Zwitterionic hydrogel coated superhydrophilic hierarchical antifouling floater enables unimpeded interfacial steam generation and multi-contamination resistance in complex conditions. *Chemical Engineering Journal, 421*, 130344. https://doi.org/10.1016/j.cej.2021.130344

Werber, J. R., Deshmukh, A., & Elimelech, M. (2016). The critical need for increased selectivity, not increased water permeability, for desalination membranes. *Environmental Science & Technology Letters, 3*(4), 112-120. https://doi.org/10.1021/acs.estlett.6b00050

WHO, & Geneva. (2011). *Guidelines for drinking-water quality* (W. H. Organization, Ed. 4 ed., Vol. 216).

Wu, L., Dong, Z., Cai, Z., Ganapathy, T., Fang, N. X., Li, C., Yu, C., Zhang, Y., & Song, Y. (2020). Highly efficient three-dimensional solar evaporator for high salinity desalination by localized crystallization. *Nat Commun, 11*(1), 521. https://doi.org/10.1038/s41467-020-14366-1

Wu, X., Wang, Y., Wu, P., Zhao, J., Lu, Y., Yang, X., & Xu, H. (2021). Dual-Zone Photothermal Evaporator for Antisalt Accumulation and Highly Efficient Solar Steam Generation. *Advanced Functional Materials, 31*(34), 2102618. https://doi.org/10.1002/adfm.202102618

Wu, Y., Shen, L., Zhang, C., Gao, H., Chen, J., Jin, L., Lin, P., Zhang, H., &

Xia, Y. (2021). Polyacid doping-enabled efficient solar evaporation of polypyrrole hydrogel. *Desalination, 505*, 114766. https://doi.org/10.1016/j.desal.2020.114766

Xiao, C., Liang, W., Hasi, Q.-M., Chen, L., He, J., Liu, F., Wang, C., Sun, H., Zhu, Z., & Li, A. (2020). Ag/polypyrrole co-modified poly(ionic liquid)s hydrogels as efficient solar generators for desalination. *Materials Today Energy, 16*, 100417. https://doi.org/10.1016/j.mtener.2020.100417

Xiao, Y., Liu, B., Li, D., Zheng, X., Li, J., & Qin, G. (2024). Biomimetic hydrogel evaporator with excellent salt-rejection performance via edge-preferential crystallization and ion-transport effects. *Chemical Engineering Journal, 497*. https://doi.org/10.1016/j.cej.2024.155038

Xie, Z., Zhu, J., & Zhang, L. (2021). Three-Dimensionally Structured Polypyrrole-Coated Setaria viridis Spike Composites for Efficient Solar Steam Generation. *ACS Appl Mater Interfaces, 13*(7), 9027-9035. https://doi.org/10.1021/acsami.0c22917

Xu, L., Cheng, L., Wang, C., Peng, R., & Liu, Z. (2014). Conjugated polymers for photothermal therapy of cancer. *Polymer Chemistry, 5*(5), 1573-1580. https://doi.org/10.1039/C3PY01196H

Xu, T., Xu, Y., Wang, J., Lu, H., Liu, W., & Wang, J. (2021). Sustainable self-cleaning evaporator for long-term solar desalination using gradient

structure tailored hydrogel. *Chemical Engineering Journal, 415*, 128893. https://doi.org/10.1016/j.cej.2021.128893

Xu, W., Xing, Y., Liu, J., Wu, H., Cui, Y., Li, D., Guo, D., Li, C., Liu, A., & Bai, H. (2019). Efficient Water Transport and Solar Steam Generation via Radially, Hierarchically Structured Aerogels. *ACS Nano, 13*(7), 7930-7938. https://doi.org/10.1021/acsnano.9b02331

Xu, X., Ozden, S., Bizmark, N., Arnold, C. B., Datta, S. S., & Priestley, R. D. (2021). A Bioinspired Elastic Hydrogel for Solar-Driven Water Purification. *Adv Mater, 33*(18), 2007833. https://doi.org/10.1002/adma.202007833

Xu, Y., Guo, Z., Wang, J., Chen, Z., Yin, J., Zhang, Z., Huang, J., Qian, J., & Wang, X. (2021). Harvesting Solar Energy by Flowerlike Carbon Cloth Nanocomposites for Simultaneous Generation of Clean Water and Electricity. *ACS Applied Materials and Interfaces, 13*(23), 27129–27139. https://doi.org/10.1021/acsami.1c07091

Xu, Y., Xu, J., Zhang, J., Li, X., Fu, B., Song, C., Shang, W., Tao, P., & Deng, T. (2022). All-in-one polymer sponge composite 3D evaporators for simultaneous high-flux solar-thermal desalination and electricity generation. *Nano Energy, 93*. https://doi.org/10.1016/j.nanoen.2021.106882

Xu, Z., Li, Z., Jiang, Y., Xu, G., Zhu, M., Law, W.-C., Yong, K.-T., Wang, Y.,

Yang, C., Dong, B., & Xing, F. (2020). Recent advances in solar-driven evaporation systems. *Journal of Materials Chemistry A, 8*, 25571. https://doi.org/10.1039/D0TA08869B

Yang, B., Zhang, Z., Liu, P., Fu, X., Wang, J., Cao, Y., Tang, R., Du, X., Chen, W., Li, S., Yan, H., Li, Z., Zhao, X., Qin, G., Chen, X. Q., & Zuo, L. (2023). Flatband lambda-Ti(3)O(5) towards extraordinary solar steam generation. *Nature*. https://doi.org/10.1038/s41586-023-06509-3

Yang, F., Chen, J., Ye, Z., Ding, D., Myung, N. V., & Yin, Y. (2021). Ni-based Plasmonic/Magnetic Nanostructures as Efficient Light Absorbers for Steam Generation [Article]. *Advanced Functional Materials, 31*(7), 9, Article 2006294. https://doi.org/10.1002/adfm.202006294

Yang, L., Li, N., Guo, C., He, J., Wang, S., Qiao, L., Li, F., Yu, L., Wang, M., & Xu, X. (2021). Marine biomass-derived composite aerogels for efficient and durable solar-driven interfacial evaporation and desalination. *Chemical Engineering Journal, 417*, 128051. https://doi.org/10.1016/j.cej.2020.128051

Yang, M., Luo, H., Zou, W., Liu, Y., Xu, J., Guo, J., Xu, J., & Zhao, N. (2022). Ultrafast Solar-Vapor Harvesting Based on a Hierarchical Porous Hydrogel with Wettability Contrast and Tailored Water States. *ACS Appl Mater Interfaces, 14*(21), 24766-24774. https://doi.org/10.1021/acsami.2c03597

Yang, S., Zhang, H., Sun, X., Bai, J., & Zhang, J. (2024). 3D-Printed Liquid Metal-in-Hydrogel Solar Evaporator: Merging Spectrum-Manipulated Micro-Nano Architecture and Surface Engineering for Solar Desalination. *ACS Nano*. https://doi.org/10.1021/acsnano.3c12574

Yang, T., Lin, H., Lin, K.-T., & Jia, B. (2020). Carbon-based absorbers for solar evaporation: Steam generation and beyond. *Sustainable materials technologies, 25*, e00182. https://doi.org/10.1016/j.susmat.2020.e00182

Yang, Y., Que, W., Zhao, J., Han, Y., Ju, M., & Yin, X. (2019). Membrane assembled from anti-fouling copper-zinc-tin-selenide nanocarambolas for solar-driven interfacial water evaporation. *Chemical Engineering Journal, 373*, 955-962. https://doi.org/10.1016/j.cej.2019.05.099

Yin, J., You, X., Zhang, Z., Guo, Z., Wang, J., & Wang, X. (2021). Boron nanosheets loaded with MoS2 porous sponges for water purification. *Journal of Water Process Engineering, 41*, 102048. https://doi.org/10.1016/j.jwpe.2021.102048

Yin, X., Zhang, Y., Guo, Q., Cai, X., Xiao, J., Ding, Z., & Yang, J. (2018). Macroporous Double-Network Hydrogel for High-Efficiency Solar Steam Generation Under 1 sun Illumination. *ACS Applied Materials & Interfaces, 10*(13), 10998-11007. https://doi.org/10.1021/acsami.8b01629

Yu, F., Chen, Y., Liang, X., Xu, J., Lee, C., Liang, Q., Tao, P., & Deng, T. (2017). Dispersion stability of thermal nanofluids. *Progress in natural science: Materials International, 27*(5), 531-542. https://doi.org/10.1016/j.pnsc.2017.08.010

Yu, F., Chen, Z., Guo, Z., Irshad, M. S., Yu, L., Qian, J., Mei, T., & Wang, X. (2020). Molybdenum Carbide/Carbon-Based Chitosan Hydrogel as an Effective Solar Water Evaporation Accelerator. *ACS Sustainable Chemistry & Engineering, 8*(18), 7139-7149. https://doi.org/10.1021/acssuschemeng.0c01499

Yu, F., Ming, X., Xu, Y., Chen, Z., Meng, D., Cheng, H., Shi, Z., Shen, P., & Wang, X. (2019). Quasimetallic Molybdenum Carbide–Based Flexible Polyvinyl Alcohol Hydrogels for Enhancing Solar Water Evaporation. *Advanced Materials Interfaces, 6*(24), 1901168. https://doi.org/10.1002/admi.201901168

Yu, H., Jin, H., Qiu, M., Liang, Y., Sun, P., Cheng, C., Wu, P., Wang, Y., Wu, X., Chu, D., Zheng, M., Qiu, T., Lu, Y., Zhang, B., Mai, W., Yang, X., Owens, G., & Xu, H. (2024). Making Interfacial Solar Evaporation of Seawater Faster than Fresh Water. *Adv Mater*, e2414045. https://doi.org/10.1002/adma.202414045

Yu, K., Shao, P., Meng, P., Chen, T., Lei, J., Yu, X., He, R., Yang, F., Zhu, W., & Duan, T. (2020). Superhydrophilic and highly elastic monolithic

sponge for efficient solar-driven radioactive wastewater treatment under one sun. *J Hazard Mater, 392*, 122350. https://doi.org/10.1016/j.jhazmat.2020.122350

Yu, Z., & Wu, P. (2020). Biomimetic MXene-Polyvinyl Alcohol Composite Hydrogel with Vertically Aligned Channels for Highly Efficient Solar Steam Generation. *Advanced Materials Technologies, 5*(6), 2000065. https://doi.org/10.1002/admt.202000065

Yuan, J., Lei, X., Yi, C., Jiang, H., Liu, F., & Cheng, G. J. (2021). 3D-printed hierarchical porous cellulose/alginate/carbon black hydrogel for high-efficiency solar steam generation. *Chemical Engineering Journal*, 132765. https://doi.org/10.1016/j.cej.2021.132765

Zang, L., Sun, L., Zhang, S., Finnerty, C., Kim, A., Ma, J., & Mi, B. (2021). Nanofibrous Hydrogel-Reduced Graphene Oxide Membranes for Effective Solar-driven Interfacial Evaporation and Desalination. *Chemical Engineering Journal, 422*, 129998. https://doi.org/10.1016/j.cej.2021.129998

Zeng, J., Wang, Q., Shi, Y., Liu, P., & Chen, R. (2019). Osmotic Pumping and Salt Rejection by Polyelectrolyte Hydrogel for Continuous Solar Desalination. *Advanced Energy Materials, 9*(38), 1900552. https://doi.org/10.1002/aenm.201900552

Zhan, Z., Chen, L., Wang, C., Shuai, Y., Duan, H., & Wang, Z. (2023). Super

Water-Storage Self-Adhesive Gel for Solar Vapor Generation and Collection. *ACS Appl Mater Interfaces, 15*(6), 8181-8189. https://doi.org/10.1021/acsami.2c21555

Zhang, C.-R., Cui, W.-R., Niu, C.-P., Yi, S.-M., Liang, R.-P., Qi, J.-X., Chen, X.-J., Jiang, W., Zhang, L., & Qiu, J.-D. (2021). rGO-based covalent organic framework hydrogel for synergistically enhance uranium capture capacity through photothermal desalination. *Chemical Engineering Journal, 428*, 131178. https://doi.org/10.1016/j.cej.2021.131178

Zhang, D., Cai, Y., Liang, Q., Wu, Z., Sheng, N., Zhang, M., Wang, B., & Chen, S. (2020). Scalable, Flexible, Durable, and Salt-Tolerant CuS/Bacterial Cellulose Gel Membranes for Efficient Interfacial Solar Evaporation. *ACS Sustainable Chemistry & Engineering, 8*(24), 9017-9026. https://doi.org/10.1021/acssuschemeng.0c01707

Zhang, D., Zhang, M., Chen, S., Liang, Q., Sheng, N., Han, Z., Cai, Y., & Wang, H. (2021). Scalable, self-cleaning and self-floating bi-layered bacterial cellulose biofoam for efficient solar evaporator with photocatalytic purification [Article]. *Desalination, 500*, 10, Article 114899. https://doi.org/10.1016/j.desal.2020.114899

Zhang, H., Li, L., He, N., Wang, H., Wang, B., Dong, T., Jiang, B., & Tang, D. (2022). Bioinspired hierarchical evaporator via cell wall

engineering for highly efficient and sustainable solar desalination. *EcoMat, 4*(5). https://doi.org/10.1002/eom2.12216

Zhang, H., Wang, K., Wang, L., Xie, H., & Yu, W. (2020). Mesoporous CuO with full spectrum absorption for photothermal conversion in direct absorption solar collectors. *Solar Energy, 201*, 628-637. https://doi.org/10.1016/j.solener.2020.03.047

Zhang, H., Xie, H., Han, W., Yan, X., Liu, X., He, L., Lin, P., Xia, Y., Zhang, K., Zapien, J. A., & Yoon, K.-B. (2021). Graphene Oxide–Reduced Graphene Oxide Janus Membrane for Efficient Solar Generation of Water Vapor. *ACS Applied Nano Materials, 4*(2), 1916-1923. https://doi.org/10.1021/acsanm.0c02765

Zhang, L., Zhang, Y., Zou, M., Yu, C., Li, C., Gao, C., Dong, Z., Wu, L., & Song, Y. (2023). A Bionic-Gill 3D Hydrogel Evaporator with Multidirectional Crossflow Salt Mitigation and Aquaculture Applications. *Advanced Functional Materials, 33*(24). https://doi.org/10.1002/adfm.202300318

Zhang, P., Liao, Q., Yao, H., Cheng, H., Huang, Y., Yang, C., Jiang, L., & Qu, L. (2018). Three-dimensional water evaporation on a macroporous vertically aligned graphene pillar array under one sun. *Journal of Materials Chemistry A, 6*(31), 15303-15309. https://doi.org/10.1039/c8ta05412f

Zhang, S., Li, M., Jiang, C., Zhu, D., & Zhang, Z. (2024). Cost-Effective 3D-Printed Bionic Hydrogel Evaporator for Stable Solar Desalination. *Advanced Science, 11*(17), 2308665. https://doi.org/10.1002/advs.202308665

Zhang, W., Chang, Q., Xue, C., Yang, J., & Hu, S. (2021). A Gelation-Stabilized Strategy toward Photothermal Architecture Design for Highly Efficient Solar Water Evaporation. *Solar RRL, 5*(5), 2100133. https://doi.org/10.1002/solr.202100133

Zhang, W., Chen, Y., Ji, Q., Fan, Y., Zhang, G., Lu, X., Hu, C., Liu, H., & Qu, J. (2024). Assessing global drinking water potential from electricity-free solar water evaporation device. *Nat Commun, 15*(1), 6784. https://doi.org/10.1038/s41467-024-51115-0

Zhang, X., Peng, Y., Shi, L., & Ran, R. (2020). Highly Efficient Solar Evaporator Based On a Hydrophobic Association Hydrogel. *ACS Sustainable Chemistry & Engineering, 8*(49), 18114-18125. https://doi.org/10.1021/acssuschemeng.0c06462

Zhang, X., Wang, X., Wu, W. D., Chen, X. D., & Wu, Z. (2019). Self-floating monodisperse microparticles with a nano-engineered surface composition and structure for highly efficient solar-driven water evaporation. *Journal of Materials Chemistry A, 7*(12), 6963-6971. https://doi.org/10.1039/c8ta12290c

Zhang, X. S., Mao, S., Wang, J., Onggowarsito, C., Feng, A., Han, R., Liu, H., Zhang, G., Xu, Z., Yang, L., Fu, Q., & Huang, Z. (2024). Boron nanosheets boosting solar thermal water evaporation. *Nanoscale, 16*(9), 4628-4636.

Zhang, Y., Sivakumar, M., Yang, S., Enever, K., & Ramezanianpour, M. (2018). Application of solar energy in water treatment processes: A review. *Desalination, 428*, 116-145. https://doi.org/10.1016/j.desal.2017.11.020

Zhao, F., Guo, Y., Zhou, X., Shi, W., & Yu, G. (2020). Materials for solar-powered water evaporation. *Nature Reviews Materials, 5*, 388–401. https://doi.org/10.1038/s41578-020-0182-4

Zhao, F., Zhou, X., Shi, Y., Qian, X., Alexander, M., Zhao, X., Mendez, S., Yang, R., Qu, L., & Yu, G. (2018). Highly efficient solar vapour generation via hierarchically nanostructured gels. *Nat Nanotechnol, 13*(6), 489-495. https://doi.org/10.1038/s41565-018-0097-z

Zhao, L., Tian, J., Liu, Y., Xu, L., Wang, Y., Fei, X., & Li, Y. (2020). A novel floatable composite hydrogel for solar evaporation enhancement. *Environmental Science: Water Research & Technology, 6*(1), 221-230. https://doi.org/10.1039/c9ew00661c

Zhao, L., Wang, P., Tian, J., Wang, J., Li, L., Xu, L., Wang, Y., Fei, X., & Li, Y. (2019). A novel composite hydrogel for solar evaporation

enhancement at air-water interface. *Sci Total Environ, 668*, 153-160. https://doi.org/10.1016/j.scitotenv.2019.02.407

Zhao, Q., Fan, T., Ding, J., Zhang, D., Guo, Q., & Kamada, M. (2011). Super black and ultrathin amorphous carbon film inspired by anti-reflection architecture in butterfly wing. *Carbon, 49*(3), 877-883. https://doi.org/10.1016/j.carbon.2010.10.048

Zhao, Q., Huang, Z., Wan, Y., Tan, J., Cao, C., Li, S., & Lee, C.-S. (2021). Multifunctional oligomer sponge for efficient solar water purification and oil cleanup. *Journal of Materials Chemistry A, 9*(4), 2104-2110. https://doi.org/10.1039/d0ta10798k

Zhao, R., Porada, S., Biesheuvel, P., & Van der Wal, A. (2013). Energy consumption in membrane capacitive deionization for different water recoveries and flow rates, and comparison with reverse osmosis. *Desalination, 330*, 35-41. https://doi.org/10.1016/j.desal.2013.08.017

Zhao, X., & Liu, C. (2020). Overcoming salt crystallization with ionic hydrogel for accelerating solar evaporation. *Desalination, 482*, 114385. https://doi.org/10.1016/j.desal.2020.114385

Zhao, Y., & Burda, C. (2012). Development of plasmonic semiconductor nanomaterials with copper chalcogenides for a future with sustainable energy materials. *Energy Environmental Science, 5*(2), 5564-5576. https://doi.org/10.1039/C1EE02734D

Zheng, X., Bao, Y., Huang, A., Qin, G., & He, M. (2023). 3D printing double-layer hydrogel evaporator with surface structures for efficient solar steam generation. *Separation and purification technology, 306*, 122741. https://doi.org/10.1016/j.seppur.2022.122741

Zhou, H., Xue, C., Chang, Q., Yang, J., & Hu, S. (2021). Assembling carbon dots on vertically aligned acetate fibers as ideal salt-rejecting evaporators for solar water purification. *Chemical Engineering Journal, 421*, 129822. https://doi.org/10.1016/j.cej.2021.129822

Zhou, X., Guo, Y., Zhao, F., Shi, W., & Yu, G. (2020). Topology-Controlled Hydration of Polymer Network in Hydrogels for Solar-Driven Wastewater Treatment. *Adv Mater, 32*(52), 2007012. https://doi.org/10.1002/adma.202007012

Zhou, X., Guo, Y., Zhao, F., & Yu, G. (2019). Hydrogels as an Emerging Material Platform for Solar Water Purification. *Acc Chem Res, 52*(11), 3244-3253. https://doi.org/10.1021/acs.accounts.9b00455

Zhou, X., Zhao, F., Guo, Y., Rosenberger, B., & Yu, G. (2019a). Architecting highly hydratable polymer networks to tune the water state for solar water purification. *Science Advances, 5*(6), eaaw5484. https://doi.org/10.1126/sciadv.aaw5484

Zhou, X., Zhao, F., Guo, Y., Rosenberger, B., & Yu, G. (2019b). Architecting highly hydratable polymer networks to tune the water state for solar

water purification. *Science Advances, 5*, eaaw5484. https://doi.org/10.1126/sciadv.aaw5484

Zhou, X., Zhao, F., Guo, Y., Zhang, Y., & Yu, G. (2018). A hydrogel-based antifouling solar evaporator for highly efficient water desalination. *Energy & Environmental Science, 11*(8), 1985-1992. https://doi.org/10.1039/c8ee00567b

Zhou, Y., Ding, T., Gao, M., Chan, K. H., Cheng, Y., He, J., & Ho, G. W. (2020). Controlled heterogeneous water distribution and evaporation towards enhanced photothermal water-electricity-hydrogen production. *Nano Energy, 77*, 105102. https://doi.org/10.1016/j.nanoen.2020.105102

Zhu, F., Wang, L., Demir, B., An, M., Wu, Z. L., Yin, J., Xiao, R., Zheng, Q., & Qian, J. (2020). Accelerating solar desalination in brine through ion activated hierarchically porous polyion complex hydrogels. *Materials Horizons, 7*(12), 3187-3195. https://doi.org/10.1039/d0mh01259a

Zhu, L., Ding, T., Gao, M., Peh, C. K. N., & Ho, G. W. (2019). Shape Conformal and Thermal Insulative Organic Solar Absorber Sponge for Photothermal Water Evaporation and Thermoelectric Power Generation. *Advanced Energy Materials, 9*(22), 1900250. https://doi.org/10.1002/aenm.201900250

Zhu, L., Gao, M., Peh, C. K. N., & Ho, G. W. (2018). Solar-driven

photothermal nanostructured materials designs and prerequisites for evaporation and catalysis applications. *Materials Horizons, 5*(3), 323-343. https://doi.org/10.1039/C7MH01064H

Zhu, L., Gao, M., Peh, C. K. N., & Ho, G. W. (2019). Recent progress in solar-driven interfacial water evaporation: Advanceddesigns and applications. *Nano Energy, 57*, 507-518. https://doi.org/10.1016/j.nanoen.2018.12.046

Zhu, L., Sun, L., Zhang, H., Yu, D., Aslan, H., Zhao, J., Li, Z., Yu, M., Besenbacher, F., & Sun, Y. (2019). Dual-phase molybdenum nitride nanorambutans for solar steam generation under one sun illumination. *Nano Energy, 57*, 842-850. https://doi.org/10.1016/j.nanoen.2018.12.058

Zhu, Z., Xu, Y., Luo, Y., Wang, W., & Chen, X. (2021). Porous evaporators with special wettability for low-grade heat-driven water desalination. *Journal of Materials Chemistry A, 9*(2), 702-726.

Zhuang, P., Li, D., Xu, N., Yu, X., & Zhou, L. (2020). Stable Self-Floating Reduced Graphene Oxide Hydrogel Membrane for High Rate of Solar Vapor Evaporation under 1 sun. *Global Challenges, 5*(1), 2000053. https://doi.org/10.1002/gch2.202000053

Zou, M., Zhang, Y., Cai, Z., Li, C., Sun, Z., Yu, C., Dong, Z., Wu, L., & Song, Y. (2021). 3D Printing a Biomimetic Bridge-Arch Solar Evaporator

for Eliminating Salt Accumulation with Desalination and Agricultural Applications. *Adv Mater,* *33*(34), e2102443. https://doi.org/10.1002/adma.202102443

Zou, Y., Zhao, J., Zhu, J., Guo, X., Chen, P., Duan, G., Liu, X., & Li, Y. (2021). A Mussel-Inspired Polydopamine-Filled Cellulose Aerogel for Solar-Enabled Water Remediation. *ACS Applied Material and Interfaces, 13*(6), 7617-7624. https://doi.org/10.1021/acsami.0c22584